

**MATERIALS FOR ADAPTIVE STRUCTURAL  
ACOUSTIC CONTROL**

Period February 1, 1995 to January 31, 1996

Annual Report

**VOLUME II**

**OFFICE OF NAVAL RESEARCH**  
Contract No.: N00014-92-J-1510

**APPROVED FOR PUBLIC RELEASE — DISTRIBUTION UNLIMITED**

Reproduction in whole or in part is permitted  
for any purpose of the United States Government

L. Eric Cross

19960703 068

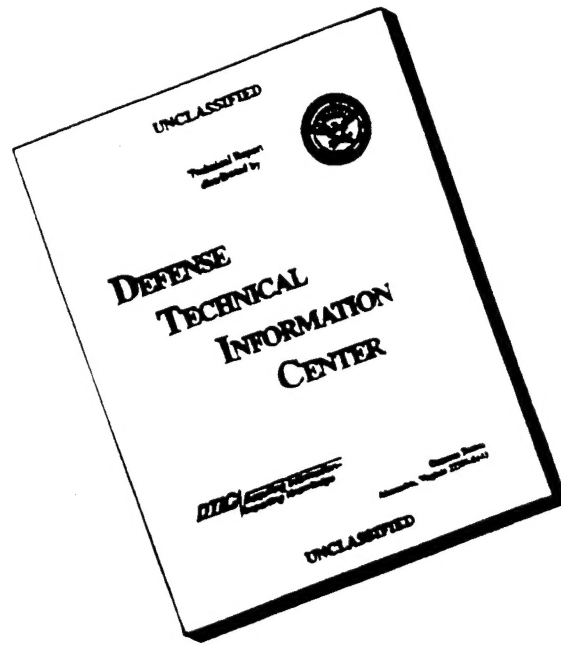
**PENNSSTATE**



**THE MATERIALS RESEARCH LABORATORY**  
UNIVERSITY PARK, PA

**DTIC QUALITY INSPECTED 1**

# DISCLAIMER NOTICE



**THIS DOCUMENT IS BEST  
QUALITY AVAILABLE. THE  
COPY FURNISHED TO DTIC  
CONTAINED A SIGNIFICANT  
NUMBER OF PAGES WHICH DO  
NOT REPRODUCE LEGIBLY.**

REPORT DOCUMENTATION PAGE			Form Approved OMB No 0704-0188	
Public reporting burden for this collection of information is estimated to average 1 hour per response, including the time for reviewing instructions, searching existing data sources, gathering and maintaining the data needed, and completing and reviewing the collection of information. Send comments regarding this burden estimate or any other aspect of this collection of information, including suggestions for reducing this burden, to Washington Headquarters Services, Directorate for Information Operations and Reports, 1215 Jefferson Davis Highway, Suite 1204, Arlington, VA 22202-4302, and to the Office of Management and Budget, Paperwork Reduction Project (0704-0188), Washington, DC 20503.				
1. AGENCY USE ONLY (Leave blank)		2. REPORT DATE 3/13/96		3. REPORT TYPE AND DATES COVERED ANNUAL REPORT 02/01/95 TO 01/31/96
4. TITLE AND SUBTITLE MATERIALS FOR ADAPTIVE STRUCTURAL ACOUSTIC CONTROL			5. FUNDING NUMBERS	
6. AUTHOR(S) L. ERIC CROSS				
7. PERFORMING ORGANIZATION NAME(S) AND ADDRESS(ES) MATERIALS RESEARCH LABORATORY THE PENNSYLVANIA STATE UNIVERSITY UNIVERSITY PARK, PA 16802			8. PERFORMING ORGANIZATION REPORT NUMBER	
9. SPONSORING/MONITORING AGENCY NAME(S) AND ADDRESS(ES) OFFICE OF NAVAL RESEARCH CODE 1513:NRJ 800 NORTH QUINCY STREET ARLINGTON, VA 22217-5660			10. SPONSORING/MONITORING AGENCY REPORT NUMBER GERALD T. SMITH OFFICE OF NAVAL RESEARCH RES. 536 SOUTH CLARK STREET, RM 286 CHICAGO, ILLINOIS 60606-1588 REP.	
11. SUPPLEMENTARY NOTES				
12a. DISTRIBUTION/AVAILABILITY STATEMENT  <div style="border: 1px solid black; padding: 5px; text-align: center;"> DEFINITION STATEMENT A  Approved for public release  Distribution Unlimited </div>			12b. DISTRIBUTION CODE	
13. ABSTRACT (Maximum 200 words)  SEE FOLLOWING THREE PAGES				
14. SUBJECT TERMS			15. NUMBER OF PAGES	
			16. PRICE CODE	
17. SECURITY CLASSIFICATION OF REPORT	18. SECURITY CLASSIFICATION OF THIS PAGE	19. SECURITY CLASSIFICATION OF ABSTRACT	20. LIMITATION OF ABSTRACT	

## GENERAL INSTRUCTIONS FOR COMPLETING SF 298

The Report Documentation Page (RDP) is used in announcing and cataloging reports. It is important that this information be consistent with the rest of the report, particularly the cover and title page. Instructions for filling in each block of the form follow. It is important to *stay within the lines* to meet optical scanning requirements.

**Block 1. Agency Use Only (Leave blank).**

**Block 2. Report Date.** Full publication date including day, month, and year, if available (e.g. 1 Jan 88). Must cite at least the year.

**Block 3. Type of Report and Dates Covered.** State whether report is interim, final, etc. If applicable, enter inclusive report dates (e.g. 10 Jun 87 - 30 Jun 88).

**Block 4. Title and Subtitle.** A title is taken from the part of the report that provides the most meaningful and complete information. When a report is prepared in more than one volume, repeat the primary title, add volume number, and include subtitle for the specific volume. On classified documents enter the title classification in parentheses.

**Block 5. Funding Numbers.** To include contract and grant numbers; may include program element number(s), project number(s), task number(s), and work unit number(s). Use the following labels:

C - Contract	PR - Project
G - Grant	TA - Task
PE - Program Element	WU - Work Unit Accession No.

**Block 6. Author(s).** Name(s) of person(s) responsible for writing the report, performing the research, or credited with the content of the report. If editor or compiler, this should follow the name(s).

**Block 7. Performing Organization Name(s) and Address(es).** Self-explanatory.

**Block 8. Performing Organization Report Number.** Enter the unique alphanumeric report number(s) assigned by the organization performing the report.

**Block 9. Sponsoring/Monitoring Agency Name(s) and Address(es).** Self-explanatory.

**Block 10. Sponsoring/Monitoring Agency Report Number.** (If known)

**Block 11. Supplementary Notes.** Enter information not included elsewhere such as: Prepared in cooperation with...; Trans. of...; To be published in... When a report is revised, include a statement whether the new report supersedes or supplements the older report.

**Block 12a. Distribution/Availability Statement.** Denotes public availability or limitations. Cite any availability to the public. Enter additional limitations or special markings in all capitals (e.g. NOFORN, REL, ITAR).

DOD - See DoDD 5230.24, "Distribution Statements on Technical Documents."

DOE - See authorities.

NASA - See Handbook NHB 2200.2.

NTIS - Leave blank.

**Block 12b. Distribution Code.**

DOD - Leave blank.

DOE - Enter DOE distribution categories from the Standard Distribution for Unclassified Scientific and Technical Reports.

NASA - Leave blank.

NTIS - Leave blank.

**Block 13. Abstract.** Include a brief (Maximum 200 words) factual summary of the most significant information contained in the report.

**Block 14. Subject Terms.** Keywords or phrases identifying major subjects in the report.

**Block 15. Number of Pages.** Enter the total number of pages.

**Block 16. Price Code.** Enter appropriate price code (NTIS only).

**Blocks 17. - 19. Security Classifications.** Self-explanatory. Enter U.S. Security Classification in accordance with U.S. Security Regulations (i.e., UNCLASSIFIED). If form contains classified information, stamp classification on the top and bottom of the page.

**Block 20. Limitation of Abstract.** This block must be completed to assign a limitation to the abstract. Enter either UL (unlimited) or SAR (same as report). An entry in this block is necessary if the abstract is to be limited. If blank, the abstract is assumed to be unlimited.



## ABSTRACT

This report documents work carried forward over the fourth year of a five year ONR sponsored University Research Initiative (URI) entitled "Materials for Adaptive Structural Acoustic Control." The program has continued to underpin the development of new electro-ceramic, single crystal and composite materials combinations for both the sensing and actuation functions in adaptive structures.

For the lead based perovskite structure relaxor ferroelectric electrostrictors, new experimental and theoretical studies have underscored the critical role of nano-scale heterogeneity on either A or B sites of the  $ABO_3$  in promoting dispersive dielectric response and the very strong opposing role of elastic stress and electrostrictive coupling in suppressing polarization fluctuations. Most important for practical application is the regimen where, under high electric field nano-polar regions begin to amalgamate into ferroelectric macro-domains with very mobile walls lead to unusually large extrinsic piezoelectric coefficients.

The program has explored a range of new relaxor:ferroelectric solid solutions which exhibit morphotropic phase boundaries between rhombohedral and tetragonal ferroelectric phases. Some of these compositions are much more tractable than PZT to grow in single crystal form. A major surprise is the very strong enhancement of the piezoelectric  $d_{33}$  and  $d_{31}$  in the crystal over that in the corresponding ceramic, and the massive anisotropy for different orientations and directions of poling. Optical studies suggest that the unusual effects reside largely in the extrinsic (domain controlled) response and we speculate about the mobility of walls in metastable phases, however further studies are required.

Antiferroelectric:ferroelectric phase switching studies in a wide range of compositions in the lead lanthanum zirconate stannate titanate system show that the first abrupt switchover to the rhombohedral ferroelectric phase only produces volume strain  $\sim 0.2\%$  as checked both by dilatometry and by X-ray. There is a large enhancement under higher field to  $\sim 0.6\%$  volume strain although the polarization does not change markedly. From thin film and single crystals studies there is mounting evidence of higher field ferroelectric:ferroelectric phase change, but again additional work is needed.

Size effect studies in perovskite ferroelectrics are continuing on this program and on the NSF/MRG in MRL. Scaling of the  $90^\circ$  stripe domains in thinned TEM samples of tetragonal composition begin to show departure from the accepted  $1/2$  power law at sub micron sizes. The structure of domains under the three dimensional constraints of grains inside the ceramic is still however almost completely unknown. Computer modeling appear to show promise and codes are being explored which permit the mutual interactions to be varied and the corresponding two dimensional structures visualized.

In composite sensors, the focus has continued upon the flextensional configurations with the new inexpensive cymbal shaped amplifier proving superior in every respect to the original "moonie." The flat section on the cymbal end cap permits very easy stacking of elements and work is now in progress to develop large area panels for low frequency testing at the Penn State ARL.

Work has continued on the thin sheet 2:2 piezoceramic polymer composites, where the transverse poling and low density lead to a desirable combination of low electrical and low acoustic impedance. An alternative fabrication procedure using extruded PZT honeycomb appears most attractive.

Two problems of major importance in actuation have been topics for study. First what are the "intrinsic" material limitations for high strain electrically driven actuation in polarization controlled systems, and secondly what are the practical limitations in multilayer actuators as they are currently fabricated and how may they be alleviated. Work on the first topic is now largely completed, showing that strains  $\sim 0.4\%$  could be switched more than  $10^9$  cycles in suitable PLZT compositions. Such reliability however requires near theoretical density, homogeneity, grain size control, critical attention to electrodes and electric field uniformity, none of which are adequately controlled in current actuator systems.

For practical actuators fabricated by inexpensive tape casting and co-firing techniques electrode termination is a major problem. In the simple MLC like designs, cracks initiate at field concentrations associated with the tip of the buried conductor layer. A new floating electrode design has been found to reduce this problem. For cracking near the end surfaces, poling of the termination layers reduces their stiffness and markedly improves performance. In the conventional structures it is also found that the floating electrode may be used directly as an acoustic emission pickup, giving early warning of cracking problems.

Under resonant driving conditions, the problems in actuators are markedly different. Heat build up and temperature run-away are significant problems traceable to dielectric loss, and new hard compositions and anti-resonant driving methods have been explored to reduce these problems.

In integration work on the high activity 0-3 composites is nearing completion. A new type of zig-zag actuator is being explored for the capability to combine both longitudinal and transverse actuation. Under a new ONR sponsored program with Virginia Polytechnic Institute and University new double amplifiers combining bimorph and flextensional concepts are being examined.

Processing studies permit the fabrication of the wide range of compositions and forms required in these material researches. Rate controlled sintering is proving to be highly advantageous, particularly for reducing delamination in integrated structures. Electrophoretic and

dielectrophoretic forming are showing promise in green assembly of thick film components where high green density is critical.

Thin film papers have been selected from the very broad range of work in MRL because of their relevance to transduction in piezoelectric and in phase switching systems.

# **MATERIALS FOR ADAPTIVE STRUCTURAL ACOUSTIC CONTROL**

Period February 1, 1995 to January 31, 1996

Annual Report

**VOLUME II**

**OFFICE OF NAVAL RESEARCH**

Contract No.: N00014-92-J-1510

**APPROVED FOR PUBLIC RELEASE — DISTRIBUTION UNLIMITED**

Reproduction in whole or in part is permitted  
for any purpose of the United States Government

L. Eric Cross

**PENNSTATE**

---



**THE MATERIALS RESEARCH LABORATORY**  
UNIVERSITY PARK, PA

## TABLE OF CONTENTS

ABSTRACT .....	8
INTRODUCTION .....	10
1.0    GENERAL SUMMARY PAPERS .....	11
2.0    MATERIALS STUDIES .....	12
3.0    COMPOSITE SENSORS .....	12
4.0    ACTUATORS STUDIES .....	13
5.0    INTEGRATION ISSUES .....	14
6.0    PROCESSING STUDIES .....	14
7.0    THIN FILM FERROELECTRICS .....	15
8.0    GRADUATE STUDENTS IN THE PROGRAM .....	16
9.0    HONORS AND AWARDS .....	16
10.0   APPRENTICE PROGRAM .....	16
11.0   PAPERS PUBLISHED IN REFEREED JOURNALS .....	17
12.0   INVITED PAPERS PRESENTATIONS AT NATIONAL AND INTERNATIONAL MEETINGS .....	21
13.0   INVITED PAPERS PRESENTED AT UNIVERSITY, INDUSTRY AND GOVERNMENT LABORATORIES .....	23
14.0   CONTRIBUTED PAPERS AT NATIONAL AND INTERNATIONAL MEETINGS .....	24
15.0   BOOKS (AND SECTIONS THEREOF) .....	27

## APPENDICES

### VOLUME I

#### *General Summary Papers*

1. Cross, L.E., "Ferroelectric Materials for Electromechanical Transducer Applications," *Jpn. J. Appl. Phys.* **34**, 2525-2532 (1995).
2. Fernandez, J.F., A. Dogan, Q.M. Zhang, J.F. Tressler, and R.E. Newnham, "Hollow Piezoelectric Composites," submitted to *Sensors and Actuators: A. Physical* (1995).
3. Uchino, K., "Recent Developments in Ceramic Actuators—Comparison among USA, Japan and Europe," Workshop on Microsystem Technologies in the USA and Canada, Dusseldorf (1995).
4. Trolier-McKinstry, S., J. Chen, K. Vedam, and R.E. Newnham, "In Situ Annealing Studies of Sol-Gel Ferroelectric Thin Films by Spectroscopic Ellipsometry," *J. Am. Ceram. Soc.* **78** [7], 1907-1913 (1995).
5. Nair, N., A. Bhalla, and R. Roy, "Inorganic Lead Compounds in Electroceramics and Glasses," *Am. Cer. Soc. Bull.* **75** [1], 77-82 (1996).
6. Gentile, A. and F.W. Ainger, "Single Crystals," Chapter 9, Materials Science and Technology, A Comprehensive Treatment, **17A** Processing of Ceramics, Part 1 (R.J. Brook, editor), VCH Verlagsgesellschaft mbH, Weinheim, Fed. Repl. of Germany (1996).

#### *Materials Studies*

7. Choi, S.W., J.M. Jung, and A.S. Bhalla, "Dielectric, Pyroelectric and Piezoelectric Properties of Calcium-Modified Lead Magnesium Tantalate-Lead Titanate Ceramics."
8. Kim, Y.J., S.W. Choi, and A.S. Bhalla, "Dielectric, Pyroelectric Properties, and Morphotropic Phase Boundary in La-Doped  $(1-x)\text{Pb}(\text{Mg}_{1/3}\text{Ta}_{2/3})-x\text{PbTiO}_3$  Solid Solution Ceramics", *Ferroelectrics* **173**, 87-96 (1995).
9. Alberta, E. and A.S. Bhalla, "A Processing and Electrical Property Investigation of the Solid Solution:  $(x)\text{Pb}(\text{In}_{1/2}\text{Nb}_{1/2})\text{O}_3-(1-x)\text{Pb}(\text{Sc}_{1/2}\text{Ta}_{1/2})\text{O}_3$ ," submitted to *Ferroelectrics* (1995).
10. Zhang, Q.M., H. You, M.L. Mulvihill, and S.J. Jang, "An X-ray Diffraction Study of Superlattice Ordering in Lead Magnesium Niobate," *Solid State Comm.* **97** [8], 693-698 (1996).
11. Zhang, Q.M., J. Zhao, and L.E. Cross, "Aging of the Dielectric and Piezoelectric Properties of Relaxor Ferroelectric Lead Magnesium Niobate-Lead Titanate in the Electric Field Biased State," *J. Appl. Phys.* **79** (6), 1-7 (1996).

## VOLUME II

### *Materials Studies (continued)*

12. Zhang, Q.M., J. Zhao, T.R. Shrout, and L.E. Cross, "The Effect of Ferroelastic Coupling in Controlling the Abnormal Aging Behavior in Lead Magnesium Niobate-Lead Titanate Relaxor Ferroelectrics," submitted *J. Mat. Res.*
13. Mulvihill, M.L., L.E. Cross, and K. Uchino, "Low-Temperature Observation of Relaxor Ferroelectric Domains in Lead Zinc Niobate," *J. Am. Ceram Soc.* **78** (12) 3345-3351 (1995).
14. Mulvihill, M.L., L.E. Cross, and K. Uchino, "Dynamic Motion of the Domain Configuration in Relaxor Ferroelectric Single Crystals as a Function of Temperature and Electric Field," 8th Euro. Mtg. Ferroelectricity, Nijmegen (1995).
15. Mulvihill, M.L., K. Uchino, Z. Li, and Wenwu Cao, "In-Situ Observation of the Domain Configurations During the Phase Transitions in Barium Titanate," accepted *Phil. Mag. B* (1995).
16. Oh, K.Y., K. Uchino, and L.E. Cross, "Electric Properties and Domain Structures in Ba(Ti,Sn)O<sub>3</sub> Ceramics."
17. Cao, W., "Elastic and Electric Constraints in the Formation of Ferroelectric Domains," *Ferroelectrics*, **172**, 31-37 (1995).
18. Cao, W. and C.A. Randall, "The Grain Size and Domain Size Relations in Bulk Ceramic Ferroelectric Materials," accepted *J. Phys. Chem. Solids* (1995).
19. Cao, W., "Defect Stabilized Periodic Amplitude Modulations in Ferroelectrics," accepted *Phase Transitions* (1995).
20. Sopko, J., A. Bhalla, and L.E. Cross, "An Improved Quantitative Method for Determining Dynamic Current Response of Ppyroelectric Materials," *Ferroelectrics*, **173**, 139-152 (1995)

## VOLUME III

### *Composite Sensors*

21. Tressler, J.F., A. Dogan, J.F. Fernandez, J.T. Fielding, Jr., K. Uchino, and R.E. Newnham, "Capped Ceramic Hydrophones," submitted to Proc. IEEE Int'l Ultrasonics Symp., Seattle (1995).
22. Koc, B., A. Dogan, J.F. Fernandez, R.E. Newnham, and K. Uchino, "Accelerometer Application of the Modified Moonie (Cymbal) Transducer," submitted *Jpn. J. Appl. Phys.* (1995).
23. Zhao, J., Q.M. Zhang, and W. Cao, "Effects of Face Plates and Edge Strips on Hydrostatic Piezoelectric Response of 1-3 Composites," *Ferroelectrics* **173**, 243-256 (1995).
24. Wu, S.J., W. Qi, and W. Cao, "Numerical Study of Ultrasonic Beam Pattern of a 1-3 Piezocomposite Transducer," accepted *Proc. IEEE Trans. Ultrasonics, Ferroelectrics and Frequency Control*. (1995).

### *Composite Sensors (continued)*—Volume III

25. Wang, H., Q.M. Zhang, and L.E. Cross, "Tailoring Material Properties by Structure Design--Radially Poled Piezoelectric Cylindrical Tube," *Ferroelectrics Lett.* (in press).
26. Zhang, Q.M. and X. Geng, "Electric Field Forced Vibration of a Periodic Piezocomposite Plate with Laminated Structure and Reflection and Transmission of a Plane Wave at the Fluid-Composite Interface," submitted to *IEEE Transactions on Ultrasonics, Ferroelectrics, and Frequency Control* (1995).
27. Geng, X., and Q.M. Zhang, "Dynamic Behavior of Periodic Piezoceramic-Polymer Composite Plates," *Appl. Phys. Lett.* **67** (21) (1995).
28. Zhang, Q.M., "Transverse Piezoelectric Mode Piezoceramic Polymer Composites with High Hydrostatic Piezoelectric Responses," *Proc. Int. Conf. on Electronic Components and Materials Sensors and Actuators*, Xi'an, China, 159-162 (1995)
29. Zhang, Q.M., H. Wang, J. Zhao, J.T. Fielding, Jr., R.E. Newnham, and L.E. Cross, "A High Sensitivity Hydrostatic Piezoelectric Transducer Based on Transverse Piezoelectric Mode Honeycomb Ceramic Composites," *IEEE Transactions on Ultrasonics, Ferroelectrics and Frequency Control* **43** (1), 26-42 (1996).
30. Zhang, Q.M., J. Chen, H. Wang, J. Zhao, L.E. Cross, and M.C. Trottier, "A New Transverse Piezoelectric Mode 2-2 Piezocomposite for Underwater Transducer Applications," *IEEE Transactions on Ultrasonics, Ferroelectrics, and Frequency Control* **42** (4), 774-780 (1995).
31. Cao, W., Q.M. Zhang, J.Z. Zhao, and L.E. Cross, "Effects of Face Plates on Surface Displacement Profile in 2-2 Piezoelectric Composites," *IEEE Transactions on Ultrasonics, Ferroelectrics, and Frequency Control* **42** (1), 37-41 (1995).
32. Cao, W. and W. Qi, "Plane Wave Propagation in Finite 2-2 Composites," *J. Appl. Phys.* **78** (7), 4627-4632 (1995).
33. Qi, W. and W. Cao, "Finite Element Analysis and Experimental Studies on the Thickness Resonance of Piezocomposite Transducers," accepted *Ultrasonic Imaging* (1995).
34. Cao, W. and W. Qi, "Multisource Excitations in a Stratified Biphase Structure," *J. Appl. Phys.* **78** (7), 4640-4646 (1995).

### VOLUME IV

#### *Actuator Studies*

35. Uchino, K., "Materials Update: Advances in ceramic actuator materials," *Materials Lett.* **22**, 1-4 (1995).
36. Uchino, K., "Novel Ceramic Actuator Materials."
37. Aburatani, H., K. Uchino, and A.F. Yoshiaki, "Destruction Mechanism and Destruction Detection Technique for Multilayer Ceramic Actuators," *Proc. of the 9th Annual International Symposium on the Applications of Ferroelectrics*, 750-752 (1995).



#### **Actuator Studies (continued)—Volume IV**

38. Uchino, K. "Manufacturing Technology of Multilayered Transducers," *Proc. Amer. Ceram. Soc.*, Manufacture of Ceramic Components, 81-93 (1995).
39. Uchino, K. "Piezoelectric Actuators/Ultrasonic Motors--Their Development and Markets," *Proc. 9th ISAF*, 319-324 (1995).
40. Dogan, A., J.F. Fernandez, K. Uchino, and R.E. Newnham, "New Piezoelectric Composite Actuator Designs for Displacement Amplification," in press *Proc. Euroceram 95* (1995).
41. Onitsuka, O., A. Dogan, J.F. Tressler, Q.Su, S. Yoshikawa, and R.E. Newnham, "Metal-Ceramic Composite Transducer, The 'Moonie' ," *J. Intelligent Materials Systems and Structures* **6**, 447-455 (1995).
42. Fernandez, J.F., A. Dogan, J.T. Fielding, K. Uchino, and R.E. Newnham, "Tailoring High Displacement Performance of Ceramic-Metal Piezocomposite Actuators 'Cymbals'," submitted to *IEEE Transactions on Ultrasonics, Ferroelectrics, and Frequency Control* (1995).
43. Hirose, S., S. Takahashi, K. Uchino, M. Aoyagi, and Y. Tomikawa, "Measuring Methods for High-Power Characteristics of Piezoelectric Materials," *Mat. Res. Soc. Symp. Proc.* **360**, 15-20 (1995).
44. Takahashi, S., S. Hirose, K. Uchino, and K.Y. Oh, "Electro-Mechanical Characteristics of Lead-Zirconate-Titanate Ceramics Under Vibration-Level Change," *Proc. 9th ISAF*, 377-382 (1995).
45. Takahashi, Sadayuki, Yasuhiro Sasaki, Seiji Hirose, and Kenji Uchino, "Electro-Mechanical Properties of  $\text{PbZrO}_3\text{-PbTiO}_3\text{-Pb}(\text{Mn}_{1/3}\text{Sb}_{2/3})\text{O}_3$  Ceramics Under Vibration-Level Change," *Mat. Res. Soc. Symp. Proc.* **360**, 305-310 (1995).

#### **VOLUME V**

46. Zheng, Jiehui, Sadayuki Takahashi, Shoko Yoshikawa, Kenji Uchino, and J.W.C. de Vries, "Heat Generation in Multilayer Piezoelectric Actuators," submitted to *J. Am. Ceram. Soc.* (1995).
47. Uchino, Kenji, "Review: Photostriction and its Applications," in press *J. Innovations in Mater. Res.* (1995).
48. Chu, Sheng-Yuan, and Kenji Uchino, "Photo-Acoustic Devices Using  $(\text{Pb},\text{La})(\text{Zr},\text{Ti})\text{O}_3$  Ceramics," *Proc. 9th ISAF*, 743-745 (1995).

#### **Integration Issues**

49. Matsko, M.G., Q.C. Xu, and R.E. Newnham, "Zig-Zag Piezoelectric Actuators: Geometrical Control of Displacement and Resonance," *J. Intell. Mat. Syst. and Struct.* **6** (6), 783-786 (1995).
50. Xu, Baomin, Qiming Zhang, V.D. Kugel, and L.E. Cross, "Piezoelectric Air Transducer for Active Noise Control," submitted *Proc. SPIE* (1996).

### **Integration Issues (continued)—Volume V**

51. Kumar, S., A.S. Bhalla, and L.E. Cross, "Underwater Acoustic Absorption by Collocated Smart Materials," accepted *Ferroelectric Letters* (1995).
52. Elissalde, Catherine and Leslie Eric Cross, "Dynamic Characteristics of Rainbow Ceramics," *J. Am. Ceram. Soc.* **78** [8], 2233-2236 (1995).

### **Processing Studies**

53. Bowen, Christopher P., Thomas R. Shrout, Robert E. Newnham, and Clive A. Randall, "Tunable Electric Field Processing of Composite Materials," *J. of Intelligent Material Systems and Structures* **6** (2), 159-168 (1995).
54. Zhang, Q.M., J. Zhao, T. Shrout, N. Kim, and L.E. Cross, "Characteristics of the Electromechanical Response and Polarization of Electric Field Biased Ferroelectrics," *J. Appl. Phys.* **77** (5), 2549-2555 (1995).
55. Zhao, J., Q.M. Zhang, N. Kim, and T. Shrout, "Electromechanical Properties of Relaxor Ferroelectric Lead Magnesium Niobate-Lead Titanate Ceramics," *Jpn. J. Appl. Phys.* **34**, 5658-5663 (1995).
56. Zipparo, M.J., K.K. Shung, and T.R. Shrout, "Piezoelectric Properties of Fine Grain PZT Materials," *Proc. IEEE Int'l Ultrasonics Symposium* (1995).
57. Yoshikawa, Shoko, Ulagaraj Selvaraj, Paul Moses, John Witham, Richard Meyer, and Thomas Shrout, "Pb(Zr,Ti)O<sub>3</sub>[PZT] Fibers—Fabrication and Measurement Methods," *J. Intell. Mat. Syst. and Struct.* **6** (2), 152-158 (1995).
58. Hackenberger, W.S., T.R. Shrout, A. Nakano, and R.F. Speyer, "Rate Controlled Sintering of Low Temperature Cofired Ceramic Multilayers Used for Electronic Packaging."
59. Randall, C.A., N. Kim, W. Cao, and T.R. Shrout, "Domain-Grain Size Relation in Morphotropic Phase Boundary, Pb(Zr<sub>0.52</sub>Ti<sub>0.48</sub>)O<sub>3</sub>," 7th US:Japan Mtg. on Dielectric and Piezoelectric Ceramics, Tsukuba, 145-149 (1995).
60. Cann, David P., Clive A. Randall, and Thomas R. Shrout, "Investigation of the Dielectric Properties of Bismuth Pyrochlores," accepted *Solid State Communication* (1995).

### **VOLUME VI**

61. Mulvihill, Maureen L., Seung Eek Park, George Risch, Zhuang Li, Kenji Uchino, and Thomas R. Shrout, "The Role of Processing Variables in the Flux Growth of PZN-PT Relaxor Ferroelectric Single Crystals."

### **Thin Films Ferroelectrics**

62. Chen, H.D., K.R. Udayakumar, L.E. Cross, J.J. Bernstein, and L.C. Niles, "Dielectric, Ferroelectric, and Piezoelectric Properties of Lead Zirconate Titanate Thick Films on Silicon Substrates," *J. Appl. Phys.* **77** (7), 3349-3353 (1995).

*Thin Films Ferroelectrics (continued)*—Volume VI

63. Udayakumar, K.R., P.J. Schuele, J. Chen, S.B. Krupanidhi, and L.E. Cross, "Thickness-Dependent Electrical Characteristics of Lead Zirconate Titanate Thin Films," *J. Appl. Phys.* **77** (8), 3981-3986 (1995).
64. Chen, H.D., K.R. Udayakumar, C.J. Gaskey, and L.E. Cross, "Electrical Properties' Maxima in Thin Films of the Lead Zirconate-Lead Titanate Solid Solution System," *Appl. Phys. Lett.* **67** (23), 3411-3413 (1995).
65. Gaskey, C.J., K.R. Udayakumar, H.D. Chen, and L.E. Cross, "'Square' Hysteresis Loops in Phase-Switching Nb-Doped Lead Zirconate Stannate Titanate Thin Films," *J. Mater. Res.* **10** (11), 2764-2769 (1995).
66. Yamakawa, K., S. Trolier-McKinstry, J.P. Dougherty, and S. Krupanidhi, "Reactive Magnetron Co-Sputtered Antiferroelectric Lead Zirconate Thin Films," *Appl. Phys. Lett.* **67** (14), 2014-2016 (1995).
67. Ravichandran, D., K. Yamakawa, A.S. Bhalla, and R. Roy, "Alkoxide Derived  $\text{SrBi}_2\text{Ta}_2\text{O}_9$  Phase Pure Powder and Thin Films."
68. Thakoor, Sarita, A.P. Thakoor, and L. Eric Cross, "Optical Non-Invasive Evaluation of Ferroelectric Films/Memory Capacitors," *Mat. Res. Soc. Symp. Proc.* **360**, 157-167 (1995).

# **MATERIALS STUDIES**

*(continued)*

# **APPENDIX 12**

The Effect of Ferroelastic Coupling in Controlling the Abnormal Aging Behavior  
in Lead Magnesium Niobate-Lead Titanate Relaxor Ferroelectrics

Q. M. Zhang, J. Zhao, T. R. Shrout, and L. E. Cross

Materials Research Laboratory, The Pennsylvania State University  
University Park, PA 16802

**Abstract:**

The abnormal aging behavior, i.e., severe aging in the electric field induced piezoelectric coefficient while very weak dielectric aging, observed in the relaxor ferroelectric lead magnesium niobate-lead titanate (PMN-PT) ceramics under a DC electric bias field can be significantly reduced by hot isostatic pressing (HIP) treatment on pre-sintered samples. The aging can also be reduced by doping suitable amounts of either La (donor) or Mn (acceptor). We suggest that the reduction in the aging is due to the introduction of additional random fields into the material which reduces the probability of the growth of micro-polar regions into metastable and/or stable polar domains. The abnormal aging behavior and the effectiveness of HIP in reducing it indicate the importance of the elastic energy in controlling the aging and relaxor behavior in PMN-PT relaxor ferroelectrics.

PACS No: 77.84.-s, 77.84. Dy, 81.40.-z

## I. Introduction.

Aging or the change of the material properties with time is of great concern in many areas of application for ferroelectric ceramics. In the past decade, there are many experimental investigations devoted to the aging phenomena in the relaxor ferroelectric materials, especially in PMN-PT ( $\text{Pb}(\text{Mg}_{1/3}\text{Nb}_{2/3})\text{O}_3\text{-PbTiO}_3$ ) and PLZT (lanthanum modified lead zirconate titanate) solid solution systems.<sup>1-4</sup> The objective of these investigations was to identify the basic mechanisms associated with aging phenomena so that they can be minimized and also to elucidate the polarization mechanism in this class of materials. From those investigations, it was found that aging in PMN-PT and PLZT exhibits quite different behaviors compared with those in normal ferroelectric ceramics such as barium titanate and lead zirconate titanate and is more complex.<sup>5</sup> For instance, as revealed by several recent experiments, aging of the dielectric behavior in PMN-PT depends strongly on the frequency and occurs even at temperatures where the material is in the pseudo-cubic phase (non-ferroelectric phase). In addition, aging was found to be not log linear with time but follows a time dependent curve of stretched exponential type:

$$d = d_{\infty} + d_1 \exp(- (t/\tau)^{\nu}) \quad (1)$$

where  $t$  is the aging time,  $d_1$  represents the part of the material constant varying with time and  $d_{\infty}$  is the time independent part, and  $\tau$  measures the aging rate. Hence, the ratio of  $d_1/d_{\infty}$  in eq. (1) is a measure of the degree (or amount) of aging in the corresponding property.<sup>6,7</sup> Eq. (1) describes a relaxation process with a broad distribution of relaxation times and a smaller  $\nu$  ( $\nu \leq 1$ ) corresponds to a broader distribution of relaxation times.<sup>8</sup> As has been reported in an earlier publication, in PMN-PT,  $\nu$  changes with temperature and decreases as the temperature approaches  $T_m$ , the temperature of dielectric constant maximum.<sup>6</sup>

In a more recent investigation, it was found that in relaxor PMN-PT ceramics, the amount of aging increases with PT content. For specimens aged under a DC bias field, it was also shown that the direction of the defect electric field developed during the aging is opposite to that of the

applied DC bias field. In addition, the piezoelectric coefficients in the field biased state exhibited more severe aging relative to the dielectric aging under the same condition. From these observations, it was suggested that the aging in the field biased state may be closely related to the growth of the micro-polar regions into metastable (and stable) polar domains. Furthermore, it was proposed that the interaction of the polarization with the stress field plays a very important role in the aging process.<sup>6</sup>

The aim of the present study is to explore possible ways to reduce or eliminate the aging observed and to search for the possible mechanisms of the aging phenomena in the relaxor PMN-PT in the electric field biased state. Undoubtedly, aging in the relaxor ferroelectric materials is a very complicated process which involves both a change in the defect structures and host lattice, as well as the interaction between them. Even for normal ferroelectric ceramics where the polarization mechanism is relatively well understood, many questions concerning the aging mechanisms remain, such as what are the relevant structural changes occurring in the material in the aging process and how the domain boundaries interact with and are stabilized by the defect fields developed during the aging process. Hence, the main focus of the work will be to present experiment results in a logical manner along with the rationale behind the study and the possible conclusions can be drawn from these experiments.

## II. Experimental

All the specimens used in this investigation were made by the mixed oxide method following the columbite B-site precursor method as described by Swartz and Shrout.<sup>9</sup> Most of the specimens were sintered at a temperature of 1250 °C for 2 -- 6 hours followed by annealing in oxygen rich atmosphere at 900 °C for 6 -- 24 hours. Other sintering and annealing conditions were also tried to examine their effect on the aging process. In spite of some variations in the aging rate and amount of aging as these conditions varied, no significant improvement and systematic trend in the aging processes were observed. Our earlier study showed that during the



aging process, there was a build-up of a defect field originated from space charges trapped at the porous regions. Hot isostatic pressing (HIP) was used to densify the specimens to minimize these regions. The density of HIP samples is at about 99.5% theoretical density compared with 95% for the conventionally sintered samples. In this study, HIP was carried out at 1100 °C under 20 MPa pressure in air. HIP samples were subsequently annealed in oxygen rich atmosphere at 900 °C for 6 hours.

The aging experiments were performed in the temperatures above  $T_m$ , i.e., the phase diagram region labeled "cubic" in figure 1, and at compositions with PT content below the morphotropic phase boundary (MPB) ( $PT < 33\%$ ) where the materials are in the relaxor region and exhibit typical electrostrictive behavior,<sup>10,11</sup> and for the specimens under a DC bias field. In this phase diagram region, the strain ( $S$ ) is related to the applied electric field ( $E$ ) through a quadratic relationship,  $S = M E^2$  where the proportional constant  $M$  is termed as the electric field related electrostrictive coefficient. For many device applications, a DC bias field  $E_{bias}$  is applied onto the specimen to break the centre of symmetry and under this condition, the strain vs electric field follows approximately a linear relationship which can be described by an effective piezoelectric coefficient  $d$  ( $d = S / E$ ).

Both pure PMN-PT and PMN-PT doped with La ( $y \leq 1$  in  $(Pb_{(1-3y/2)}La_y)(Mg_{1/3}Nb_{2/3})(1-x)Ti_xO_3$ ) and with Mn were investigated. In a previous publication, we showed that as the composition approaches the MPB, the aging in the field biased state becomes severe.<sup>6</sup> Hence, the current investigation was concentrated on the phase diagram region near the MPB.

The change of the dielectric constant, the effective piezoelectric coefficient, and the polarization level at the DC field biased state as a function of time were recorded simultaneously. This is quite different from most of the earlier aging experiments where only the dielectric aging was investigated, and hence the results provide more complete information about the aging process. The piezoelectric coefficient, either  $d_{33}$  or  $d_{31}$ , was measured by a double beam laser dilatometer.<sup>12</sup> The dielectric aging under a DC bias field was evaluated using a set-up shown in

figure 2 where the current passing through the small resistor  $R$  was measured and the polarization level was determined by a standard Sawyer-Tower circuit.<sup>13</sup> In all these experiments, the temperature was controlled within 0.1 °C fluctuation. In addition, the dielectric constant and the current released during the sample heating were acquired as a function of temperature for samples without DC bias fields. The capacitance measurement was made with a multi-function LCR meter (HP 4274A) and the current was measured with a pA meter (HP 4140B). For these experiments, the temperature change was provided by a Delta temperature chamber controlled by a HP computer. To probe the change in the structure due to HIP process, x-ray powder diffraction measurement was also carried out using a Scintag diffractometer (Cu  $K\alpha$  source).

Although the aging rate and the amount of aging vary with frequency and DC bias field level, which are interesting and deserve detailed investigation, they are not the theme of the paper and the general trends reported here will not change markedly with these variables as revealed by the experimental observations. The data on the aging behavior reported here are at a fixed frequency of 1 kHz with a DC bias field level of 5 kV/cm.

### III. Results and discussions

#### (a) Effect of HIP

Shown in figure 3 are the aging data for HIP samples of the composition 0.68PMN-0.32PT doped with 1 mole % La which has  $T_m$  at a temperature near 129 °C. Compared with the aging data for conventionally sintered samples of the same composition as shown in figure 4, it is obvious that HIP significantly reduces and nearly eliminates aging in both the dielectric constant and the effective piezoelectric coefficient. To make a quantitative comparison, eq. (1) is used to fit the data in figures 3 and 4 and the results are listed in Table I. Aging experiments were also carried out on other PMN-PT compositions and similar results were obtained.

The results demonstrate that the HIP treatment on pre-sintered ceramic specimens is a very effective means in reducing or eliminating the observed aging in relaxor PMN-PT. To shed some lights on the possible mechanisms behind this improvement on the aging properties in HIP specimens, it is instructive to consider first what might happen in the aging process of relaxor PMN-PT under a DC electric field.

From the current understanding on the relaxor ferroelectrics, the polarization mechanism in the material is from the micro-polar clusters and their dynamic nature and the induced ferroelectric transition in the non-polar micro-regions.<sup>14,15</sup> The response of these micro-polar and non-polar regions to external fields yields the observed large dielectric constant and electrostrictive strain. The inability of the micro-polar regions to grow in size as the temperature is lowered is due to the existence of local random fields that lower the local symmetry compared with the global symmetry and prevent the development of normal long-range order.<sup>16</sup> The existence of such randomness or random field is crucial for the material to exhibit relaxor behavior. When a DC bias field is applied to the material, it will tend to overcome the local random fields and induce a macroscopic polarization (coalescing of the micro-polar regions). Now the question is whether this process is fully reversible, that is, as one reduces this external ordering field, whether the original state will be fully recovered. Clearly, it will depend on the magnitude of the energy barriers in breaking up a large polarization region into micro-regions, which are functions of temperature and related to the microstructures, and also depend on the temperature where the aging experiment is performed. For a material with strong local random fields, this process will be nearly fully recovered and no-aging or very small aging in the material properties will be expected. This could be the situation for the PMN-PT at low PT content where the material shows very little aging. As the composition approaches the MPB, earlier experimental results from dielectric constant measurements and TEM studies already showed that the material becomes more normal-ferroelectric like, i.e., a reduction in the dielectric dispersion, a sharpening in the dielectric constant peak, and the disappearing of "random" structural

inhomogeneity on the nanometer scale.<sup>10,17</sup> Therefore, it is expected that under a DC bias field there is an increased probability to form large size polar domains which may not be switchable thermally and will not follow the change of external fields. The slow increase of the population of large metastable (and/or stable) polar domains with time should be one of the causes for the observed aging here.

In aged samples, by reversing the direction of DC bias field, the induced piezoelectric constant can be recovered in a large part (more than 90%). This is consistent with the fact that the large polar regions formed during the aging are broken up by a reverse electric field which causes the polarization switching in the material.

As we have shown in an earlier publication and the data in figure 4, in the DC field biased state, the aging in the piezoelectric coefficient is more severe compared with the dielectric aging under the same DC bias. In some cases, the dielectric constant shows very little aging while a severe aging is observed in the piezoelectric coefficient as shown in figure 5 which was taken from 0.72PMN-0.28PT at 140 °C ( $T_m = 138$  °C). We do not have the explanation on why in some specimens, although the dielectric aging is relatively weak compared with the aging in the piezoelectric coefficient, it is still substantial (the data in figure 4), while for other specimens, the dielectric aging is very little (the data in figure 5).

From the thermodynamics consideration, for an electrostrictive material biased under an external field, the effective piezoelectric coefficient  $d_{ij}$  has the relationship:

$$d_{33} = 2 Q_{11} K \epsilon_0 P \quad (\text{or } d_{31} = 2 Q_{12} K \epsilon_0 P) \quad (2)$$

where  $Q_{ij}$  is the charge related electrostrictive coefficient,  $P$  is the polarization level at the DC biased state,  $K$  is the dielectric constant,  $\epsilon_0$  is the vacuum dielectric permittivity.<sup>18</sup> Eq. (2) suggests that there should be reduction in either  $P$  or  $Q_{ij}$ , or both in the aged sample if  $K$  does not change very much during the aging. Our experimental results indicate that  $P$  is indeed reduced in the aging process. However, for all the specimens measured, the reduction in  $P$  is too small to account for the reduction in  $d_{ij}$ . Hence, it is  $Q_{ij}$  which bears the main responsibility for

the aging in  $d_{33}$  and  $d_{31}$ . In other words, the polarization slowly loses its ferroelastic component in the aging process. In terms of the polar region reorientation processes which are responsible for the large polarization and strain in PMN-PT, the results imply that the energy barriers for the polarization switching processes which generate strain response in the material are much higher than those for the pure ferroelectric polarization switching processes, which generate only the dielectric response. It should be pointed out that while the former processes must be originated from the non-180 degree polarization reorientation or switching processes and the change of polarization level in the non-polar regions, the latter can involve both the pure 180 degree polarization change and some collective non-180 degree polarization reorientation processes which do not generate net strain response in the material such as the processes proposed by Arlt and the process involving two simultaneous 90 degree polarization switchings which is equivalent to a net 180 degree polarization switch in the material.<sup>19</sup> As the specimen ages, the total polarization regions participating in non-180° polar reorientations and the reversible polarization changes which contribute to the strain response diminish while the total polarization regions participating in 180° polar reorientations (including the collective non-180 degree reorientations which do not generate strain response in the material) may not change or even increase as reflected by the small dielectric aging observed. Hence, in this abnormal aging process most of the polarization regions in the material is not pinned, but instead, is converted from the non-180° motions to the 180° motions.

From a previous study, it was found that during aging, there is a build-up of an internal defect field whose direction is against that of the applied DC field. We believe that this field is the result of drifting space charge deposited at the pore regions as schematically shown in figure 6. For a ceramic specimen sintered using conventional method which has about 95% theoretical density, there are porous regions inside grains and in the grain boundaries which serve as the sites to trap the space charges as they drift under an external DC field. HIP which densifies the specimen to 99.5% theoretical density reduces these regions and the defect field associated with them

significantly as observed experimentally. The defect field schematically shown in figure 6 can also provide some explanation to the large decrease in the piezoelectric coefficient and small change in the dielectric constant in the aging process if we assume that this defect field does not pin the polarization except reversing the field direction locally. However, the data from the Mn doped specimens presented below seem to indicate that this effect cannot be the major source for the observed abnormal aging behavior.

Therefore, the results indicate that the interaction of the polar regions with the stress field, i.e., the ferroelastic coupling, plays a major role here in producing the abnormal aging and in determining the response behavior in relaxor PMN-PT. Hence, this effect may be effective in breaking the local symmetry and generating the relaxor response.

Based on the discussion above, the possibility of random stresses introduced in the HIP and subsequent O<sub>2</sub> annealing process in the specimens was examined. A series of x-ray diffraction measurements were carried out on HIP and conventionally sintered samples. Shown in figure 7 are the x-ray powder diffraction data taken from 0.7PMN-0.3PT with 1% La HIP sample (annealed in O<sub>2</sub> atmosphere). Listed in Table II are the peak width measured in full width at half maximum (FWHM) for HIP and regularly sintered samples of this composition. Apparently, the peak width of the samples treated with HIP and O<sub>2</sub> annealing is approximately 10% wider than that of the conventionally sintered samples. Similar results were also observed for other composition samples. The broadening of the x-ray diffraction peak width in the HIP samples is interpreted as the evidence for a nonuniform micro-strain distribution.<sup>20</sup> From the data in Table II, it can be estimated that the non-uniform strain distribution introduced by HIP is at about 0.05% strain level in the sample (measured in FWHM). The significant reduction of the aging in HIP samples may be in part due to this inhomogeneous strain pattern and stress field which prevent the formation of large size metastable (and/or stable) polar clusters.

#### (b) Effect of doping

From the analysis and data presented thus far, it seems that to reduce the aging in the field biased state, a material should be moved into a state which is more relaxor-like. In relaxor PMN-PT system, it has been shown that La doping will move the material into a more relaxor state as indicated by a broadening of the dielectric constant peak and a lowering of  $T_m$ .<sup>21</sup> Hence, by doping with a suitable amount of La, one would expect to achieve a reduction of the aging in the material. The experimental results performed here confirm this and are consistent with those from the earlier investigations.<sup>4</sup> However, the reduction is not as significant as the HIP treatment.

On the other hand, the experimental results here show that a small amount of Mn doping also results in a reduction in the aging. Shown in figure 8 are the aging data taken from the specimens of La modified 0.71PMN-0.29PT with and without Mn doping (0.05 weight %). The two samples show very different aging characteristics and the piezoelectric coefficient of the Mn doped samples exhibit smaller aging. For comparison, the dielectric constant as a function of temperature of the two samples was also measured and presented in figure 9. A reduction in the maximum dielectric constant and broadening of the peak width are observed for the Mn doped sample, suggesting that the Mn-doped sample is more relaxor-like compared with the non-Mn doped sample. In addition, the low frequency dielectric loss at high temperature region, which is likely associated with the space charge conduction, is reduced significantly.

There are additional changes observed in Mn doped samples:

(1) The direction of the defect field established during aging becomes parallel to the external DC bias field. After these aged specimens were cooled down to room temperature under no external DC bias field, the remanent  $d_{33}$  value was measured using a Berlincourt  $d_{33}$  meter. For Mn doped specimens, the  $d_{33}$  was found to be positive while for non-doped specimens, the  $d_{33}$  was negative.

(2) Shown in figure 10 are the experimental results of charge release during the sample heating for aged samples. In these experiments, the aged samples were cooled down to room

temperature without a DC bias field and the current released as the samples were heated up in a constant temperature rate was measured. For non-Mn doped samples, the charge released from trapped space charges was observed at a temperature near and above their  $T_m$ . These charges were compensated by the local polar regions at low temperatures ( $< T_m$ ). The release of these charges as a result of the vanishing of local polarization at temperatures above  $T_m$  gives rise to the irregular current curve observed. On the other hand, for Mn doped samples, as a result of the stabilization of polar regions by the defect field associated with Mn which has the same direction as that of the applied DC bias field, a well defined pyroelectric peak was observed.<sup>3</sup>

These results indicate that Mn doping significantly reduces the mobile space charges in the host lattice. In addition, it is also likely that Mn defects in the host lattice traps oxygen vacancies, which are believed to be quite mobile in perovskite structure, to form  $Mn^{2+} - V_O^{\bullet\bullet}$  (and/or  $Mn^{3+} - V_O^{\bullet\bullet}$ ) complex, producing defect dipoles.<sup>22,23</sup> As a result, the defect field due to the accumulation of the drifting space charge in the porous regions observed in the non-Mn doped samples is eliminated. It may be the combined effects of the reduced space charges and the irregularities introduced by the random distribution of  $Mn^{2+} - V_O^{\bullet\bullet}$  (and/or  $Mn^{3+} - V_O^{\bullet\bullet}$ ) complex in the lattice which reduce the aging in the material.

For both La doped and Mn doped samples, HIP followed by  $O_2$  annealing significantly reduces or nearly eliminates the aging in both the piezoelectric coefficient and dielectric constant in the field biased state.

#### IV. Summary

This paper shows that the abnormal aging behavior, i.e., severe aging in the piezoelectric coefficient and weak dielectric aging, observed in relaxor PMN-PT in the electric field biased state can be nearly eliminated by HIP treatment on pre-sintered ceramic samples. The aging can also be reduced by doping suitable amounts of either La (donor) or Mn (acceptor).



The results suggest that the aging observed in relaxor PMN-PT is due to the growth of the metastable and/or stable polar regions under the bias field (or defect field). Hence, by moving the material deeper into the relaxor state (by introducing extra-randomness in the material by doping and HIP), the aging can be reduced or nearly eliminated. The abnormal aging behavior reveals that the growth of the micro-polar regions does not have a significant effect on the 180 degree polarization reorientation process, which is pure ferroelectric in nature. In other words, for PMN-PT the energy barriers for the pure non-180 degree polarization reorientation processes which generate both the polarization and strain responses in the material are much higher than those of the 180 degree polarization reorientation process and the collective non-180 processes which do not change the macroscopic strain state in the material. Therefore, by HIP treatment, which introduces random stress fields into the sample, one can effectively reduce or nearly eliminate the aging in PMN-PT in the field biased state. These results also indicate the importance of the elastic energy in controlling the relaxor behavior in PMN-PT in comparison with the electric energy.

## V. Acknowledgment

The authors wish to thank Prof. S. J. Jang for many stimulating discussions. This work was supported in part by a contract from Tektronix, Inc. and in part by the Office of Naval Research.

Table I. Comparison of the amount of aging in  $d_{31}$  and  $K_{33}$  (figures 3 and 4) for 0.68PMN-0.32PT doped with 1% La for HIP and non-HIP samples.<sup>a</sup>

Temp.	$d_{31}$ $d_1 / d_\infty$		$K_{33}$ $K_1 / K_\infty$	
	HIP	Non-HIP	HIP	Non-HIP
130 °C	0.049		0.12	
140 °C	0.046	2.5	0.08	0.8
150 °C	0.06		0.04	

<sup>a</sup> For dielectric constant, eq. (1) is written as  $K = K_\infty + K_1 \exp(-(\frac{t}{\tau})^\nu)$ .

For the piezoelectric coefficients, eq. (1) is in the form of  $d = d_\infty + d_1 \exp(-(\frac{t}{\tau})^\nu)$ .

Table II. The x-ray peak width (measured in full width at half maximum in degrees for  $\theta$ ) for HIP and conventionally sintered samples

Diffraction peak	100	110	111	200	210	211
HIP sample	0.1087	0.1136	0.110	0.176	0.183	0.180
Regular sample	0.0963	0.1055	0.105	0.162	0.166	0.163

## References:

1. W. A. Schulze, J. V. Biggers, and L. E. Cross, J. Amer. Ceram. Soc., 61, 46 (1978).
2. G. Borchhardt, J. von Cierninski, and G. Schmidt, Phys. Stat. Sol. (a), 59, 749 (1980).
3. W. Pan, E. Furman, G. O. Dayton, and L. E. Cross, J. Mater. Sci. Lett. 5, 647 (1986).
4. T. R. Shrout, W. Huebner, C. A. Randall, and A. D. Hilton, Ferro. 93, 361 (1989).
5. W. A. schulze and K. Ogino, Ferro. 87, 361 (1988).
6. Q. M. Zhang, J. Zhao, and L. E. Cross, to be published in J. Appl. Phys. 79 (1996).
7. T. Nomura, N. Kawano, J. Yamamatsu, T. Arashi, Y. Nakano, and A. Sato, Jpn. J. Appl. Phys. 34, 5389 (1995).
8. K. L. Ngai, A. K. Rajagopal, and C. Y. Huang, J. Appl. Phys. 55, 1714 (1984).
9. S.L.Swartz and T.R.Shrout. Mat. Res. Bull. 17, 1245 (1982).
10. S.W.Choi, T.R. Shrout, S.J. Jang and A.S. Bhalla. Ferro. 100, 29 (1989).
11. S. J. Jang. Ph. D. Thesis, The Pennsylvania State University (1979).
12. Q. M. Zhang, S. J. Jang, and L. E. Cross. J. Appl. Phys. 65, 2807 (1989).
13. J. K. Sinha, J. Sci. Instrum., 42, 696 (1965).
14. L. E. Cross. Ferro. 76, 241 (1987).
15. G. A. Smolenskii. J. Phys. Soc. Jpn., 28, 26 (1970).
16. D. Viehland, S. Jang, L. E. Cross, and M. Wuttig. Phil. Mag. B64, 335 (1991).
17. A. D. Hilton, C. R. Randall, D. J. Barber, and T. R. Shrout, Ferro. 93, 379 (1989).
18. A. F. Devonshire, Phil. Mag. 3, 85 (1954).
19. G. Arlt, private communications.
20. B. D. Cullity, Elements of x-ray diffraction (Addison-Wesley Publishing Company, Inc., Reading, MA, 1977).
21. N. Kim, MS thesis, the Pennsylvania State University (1990).
22. P. V. Lambeck and G. H. Jonker, Ferro., 22, 729 (1978).
23. D. M. Smyth, Prog. Solid State Chem., 15, 145 (1984).

Figure captions:

Figure 1. Phase diagram of PMN-PT solid solution system (from Choi et al.).

Figure 2. Schematic drawing of the experimental set-up used to measure the dielectric constant of PMN-PT under a DC bias field.

Figure 3. The aging data for HIP samples of composition 0.68PMN-0.32PT doped with 1 mole % La. The solid lines are the fitting using eq. (1) and solid circles and open circles are the experimental data points. The experimental temperatures are indicated in the figure and the bias field is 5 kV/cm.

Figure 4. The aging data for regularly sintered samples of composition 0.68PMN-0.32PT doped with 1 mole % La. The solid lines are the fitting using eq. (1) and solid circles and open circles are the experimental data points. The bias field is 5 kV/cm and the temperature is 140 °C. The data here are for the comparison with those in figure 3 and clearly, HIP nearly eliminates the aging in the samples.

Figure 5. The abnormal aging behavior where the piezoelectric coefficient exhibits severe aging while the dielectric aging is very weak. The data are taken from regularly sintered samples of composition 0.72PMN-0.28PT. The experimental temperature is 140 °C and the bias field is 5 kV/cm. The solid lines are drawn to guide eyes and open and solid circles are the data points.

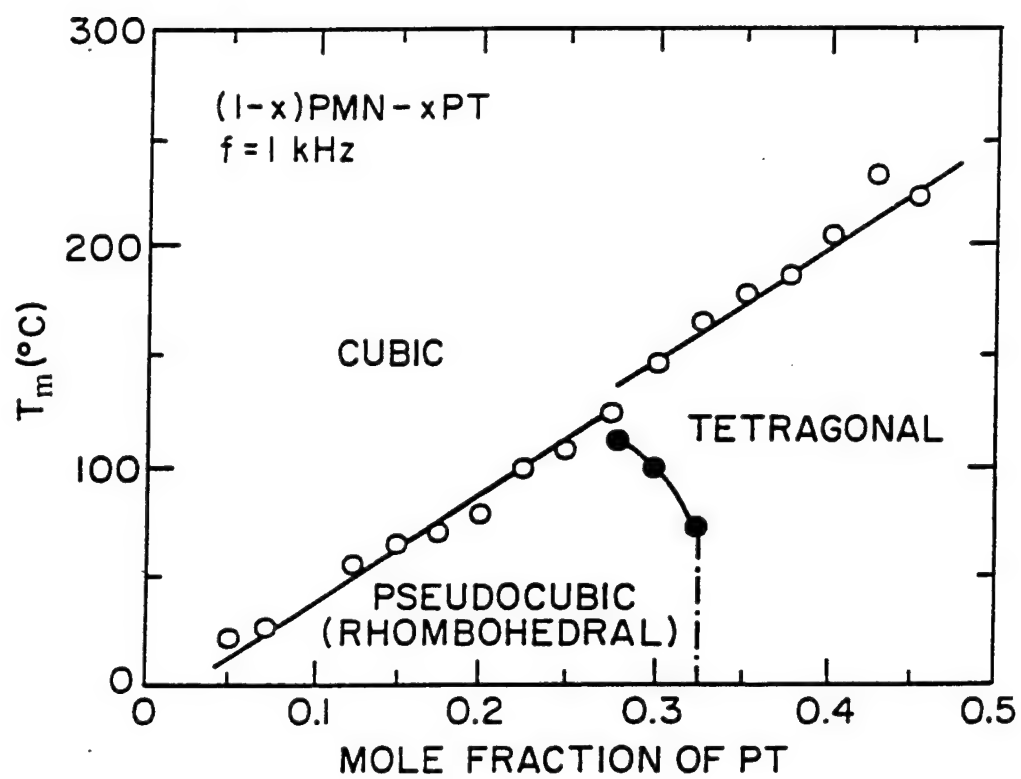
Figure-6. Schematic drawing of the space charge distribution and the resulting defect electric field at near the gap or grain boundary region for PMN-PT under DC bias field. (a) shows the space charge distribution, (b) shows the directions of the defect field in the gap region and inside the grains, and (c) shows the spatial distribution of the total electric field inside the sample.

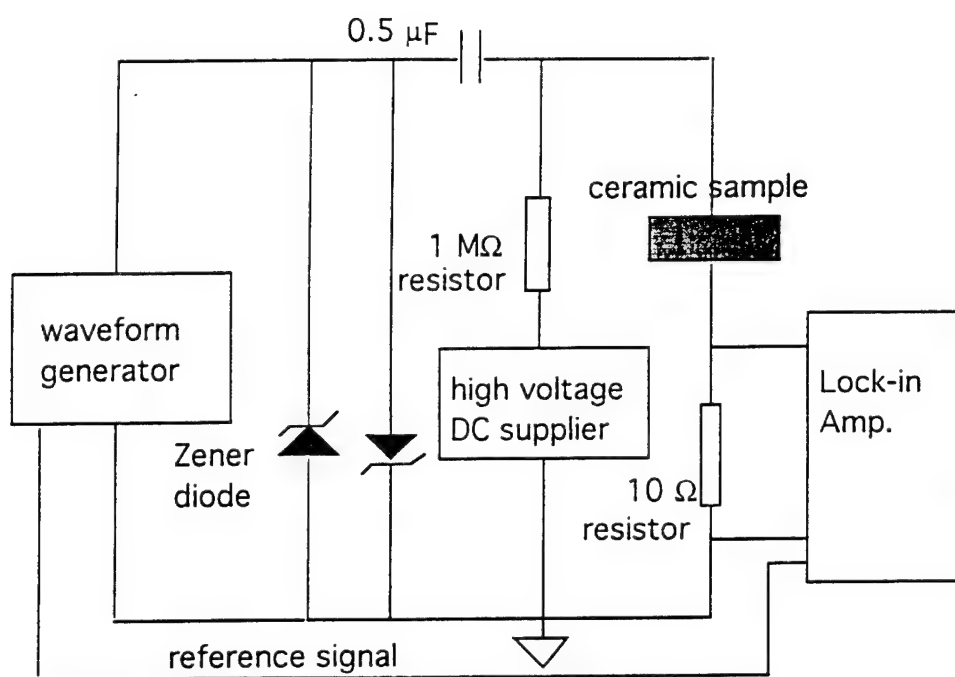
Figure 7. x-ray powder diffraction data of HIP samples of composition 0.7PMN-0.3PT doped with 1 mole % La (top figure) and the fitting of the (110) diffraction peak with a Gaussian line shape (bottom figure). In the bottom figure, the solid curve is the fitting of a Gaussian line shape from which FWHM is calculated and solid circles are the data points.

Figure 8. Aging data illustrating the reduction of the aging in the piezoelectric coefficient in the DC electric field biased state. The curve A is from Mn doped sample (0.05 weight %) and the curve B is from the sample without Mn doping (0.71PMN-0.29PT with 0.5% La). Open and solid circles are the data points and solid lines are drawn to guide eyes.

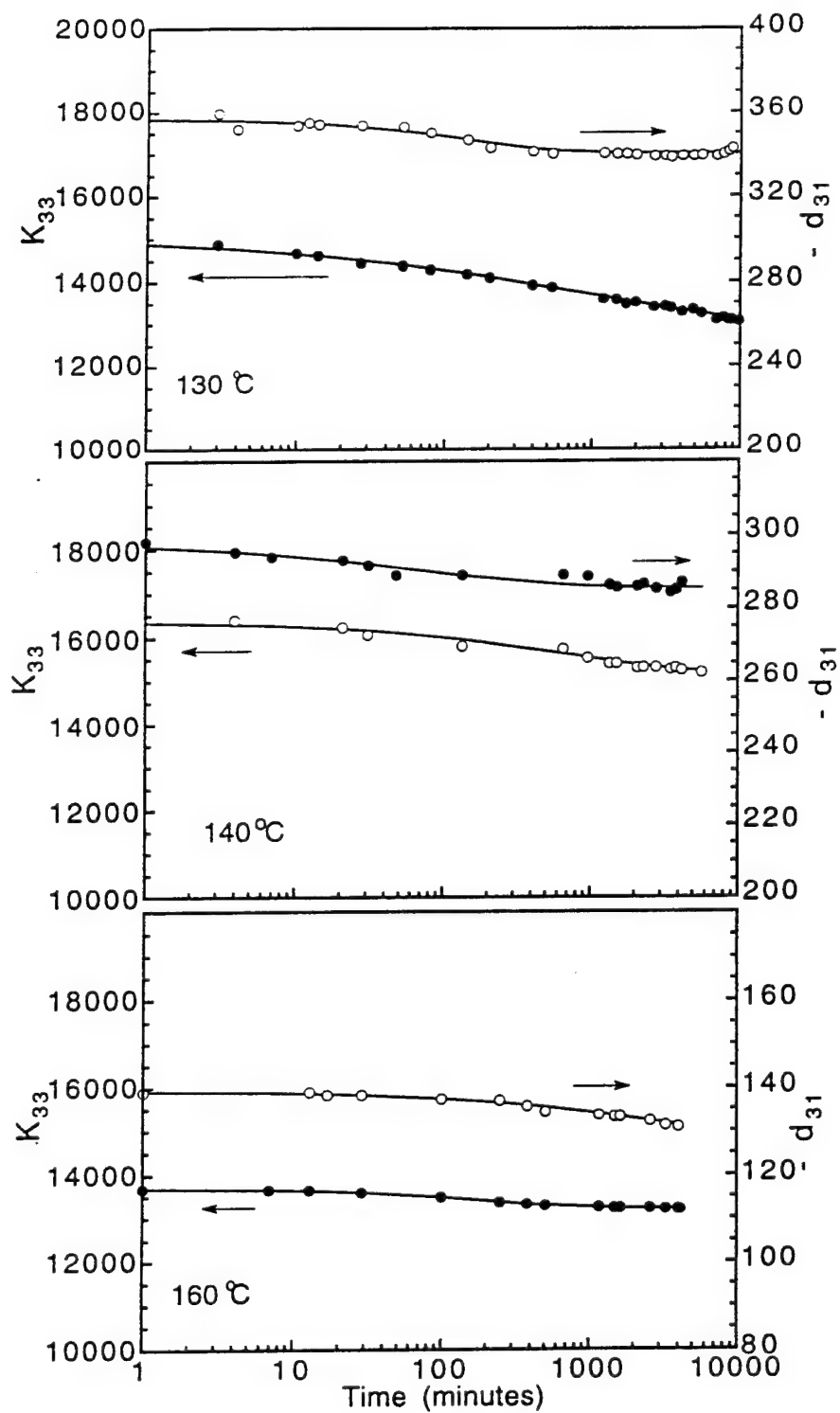
Figure 9. Dielectric constant and dielectric loss as a function of temperature for conventionally sintered samples: figure a is for 0.71PMN-0.29PT with 0.5% La and figure b is 0.05 weight % Mn doped 0.71PMN-0.29PT with 0.5% La.

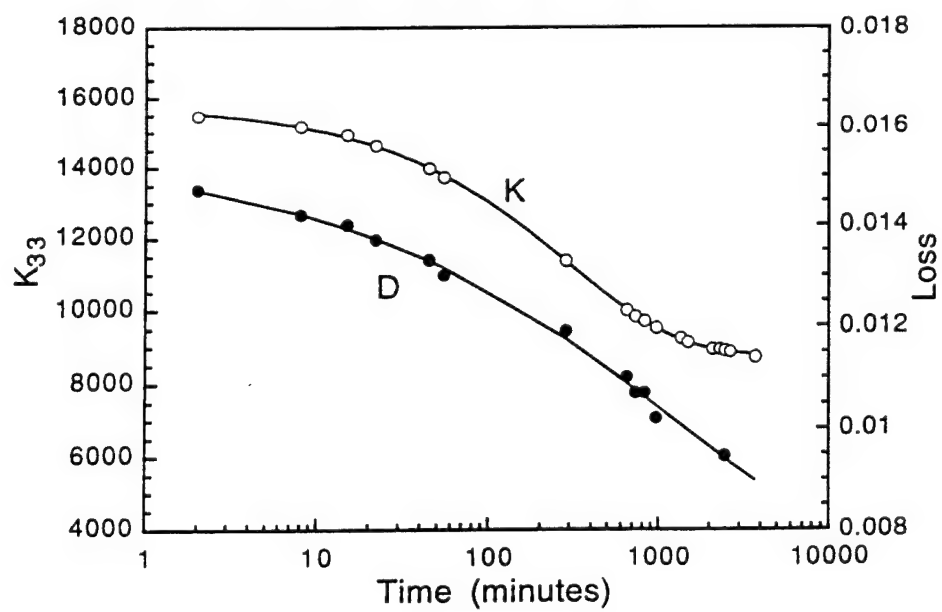
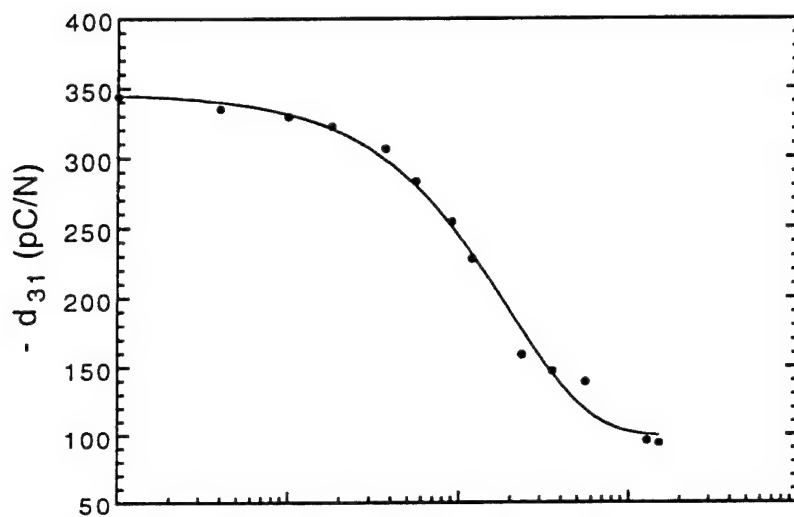
Figure 10. Comparison of the charge release data for Mn doped and undoped samples. All the samples were aged at 140 °C for more than one day under a 5 kV/cm DC bias field. The data were taken during heating (heating rate is 2 °C/min) after the DC bias field was removed and the samples were subsequently cooled down to room temperature.

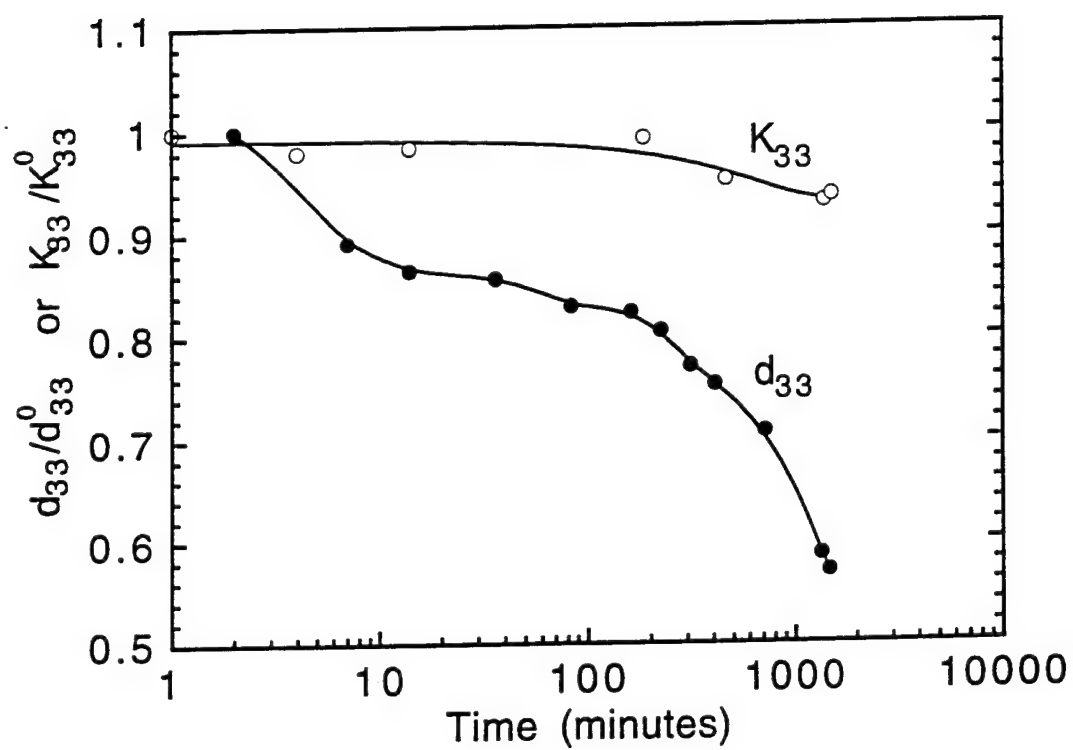


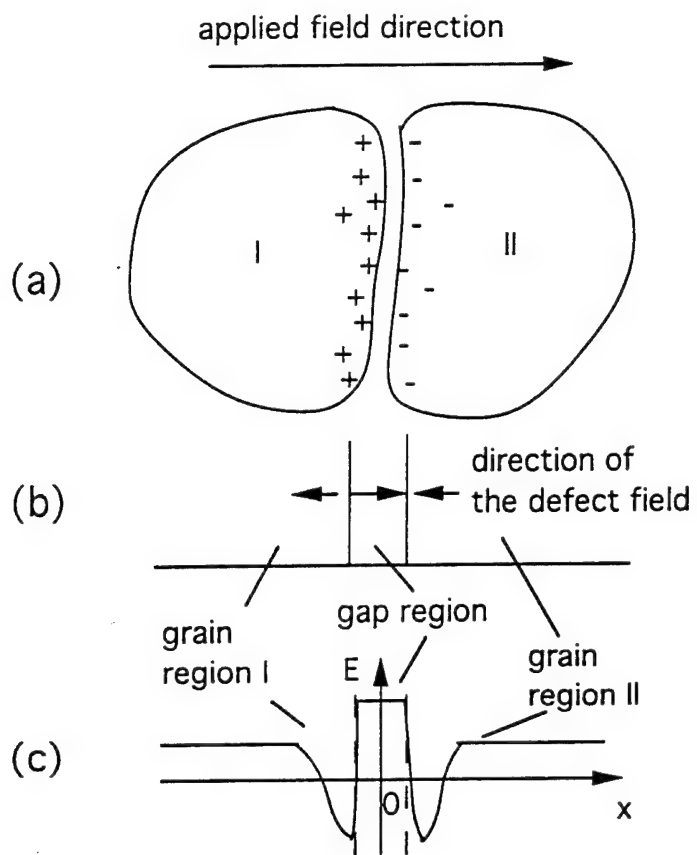


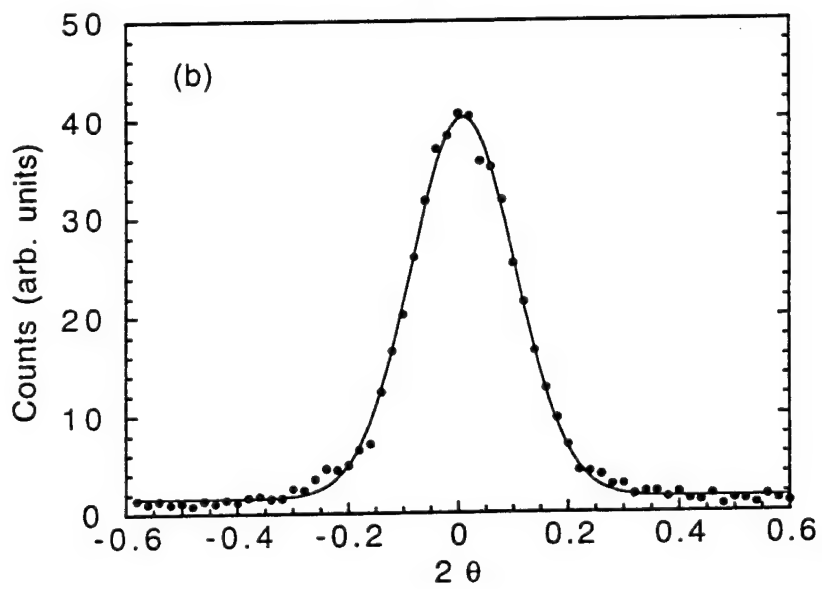
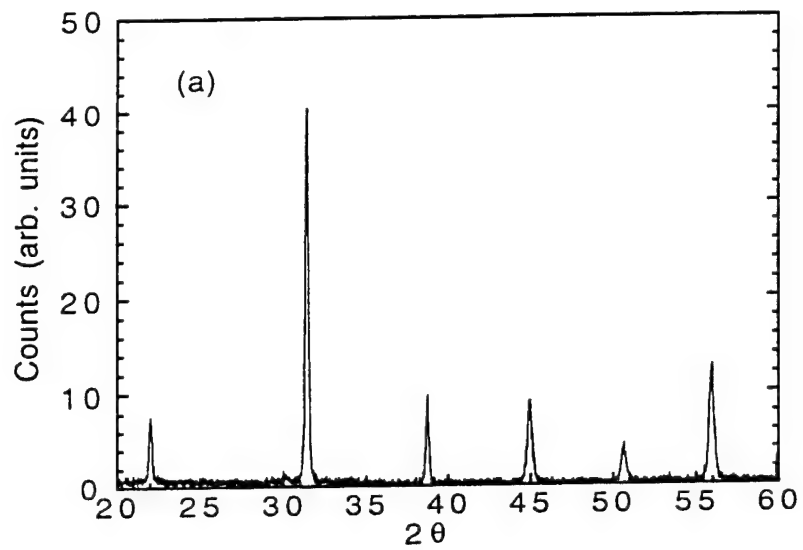


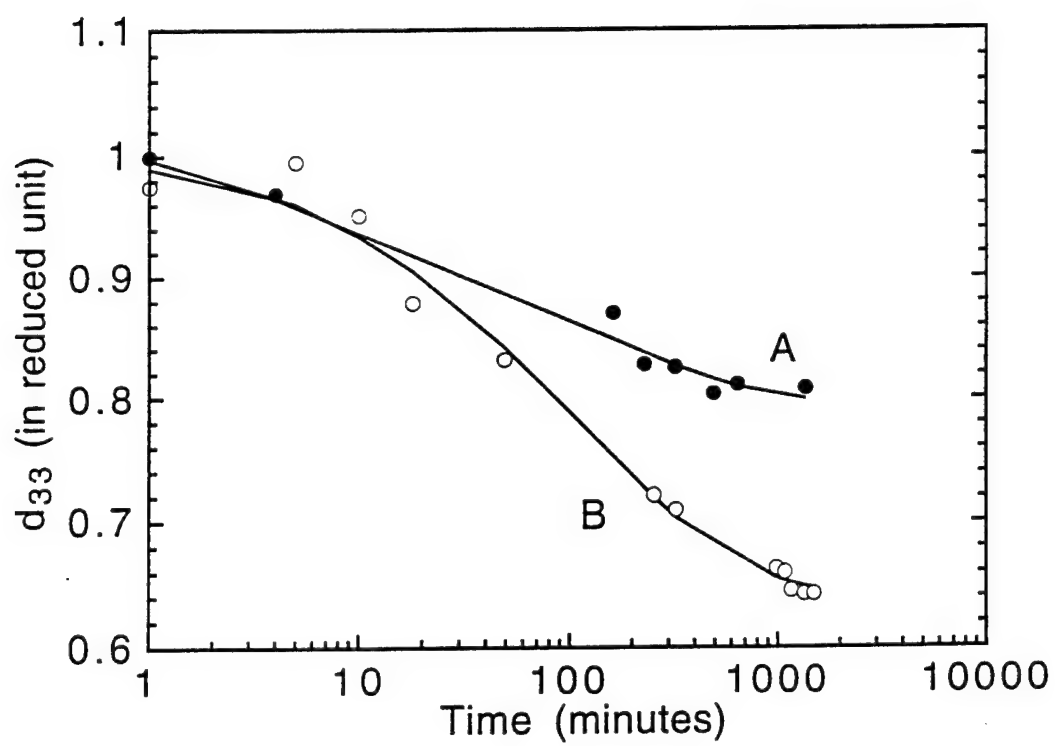


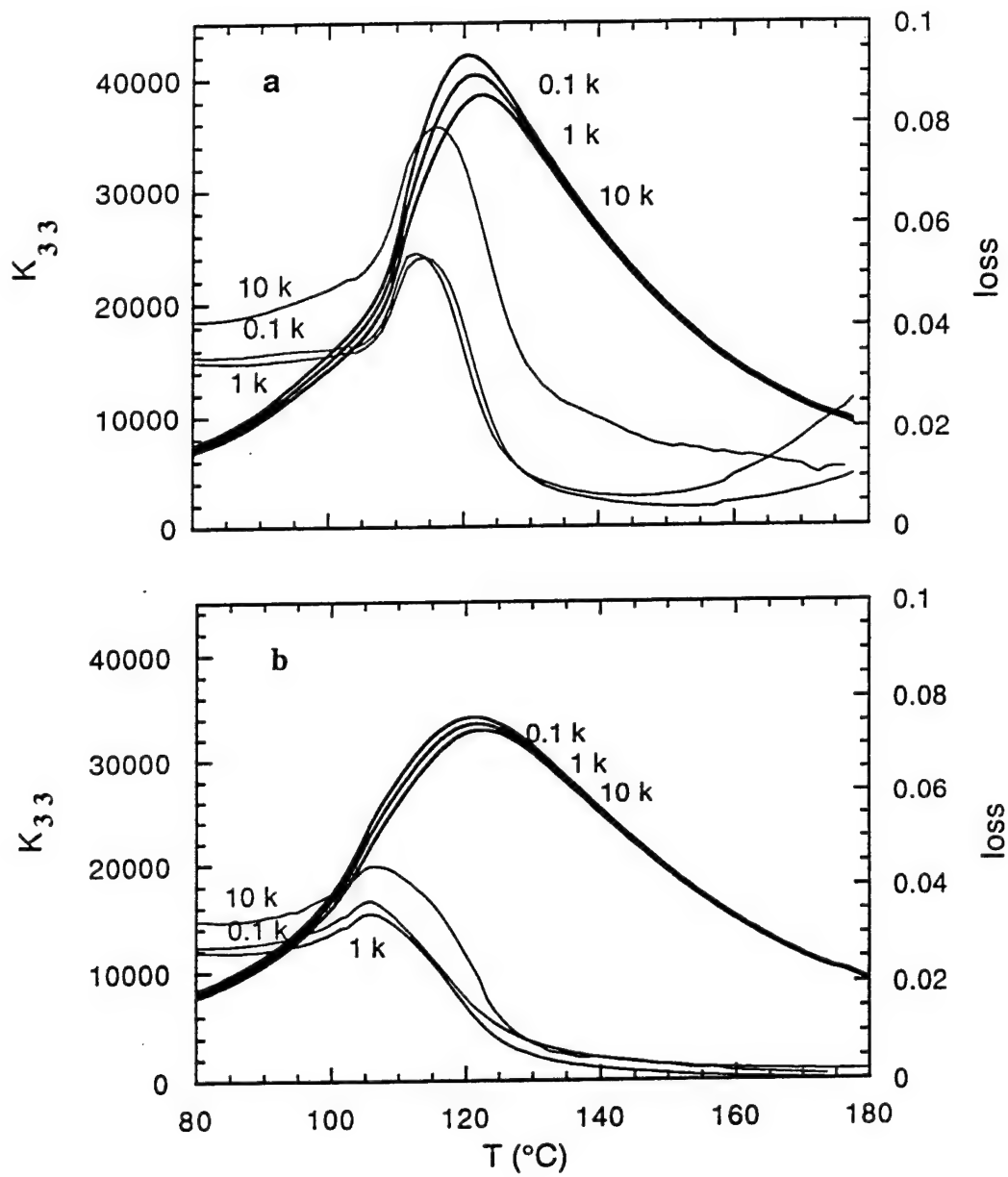


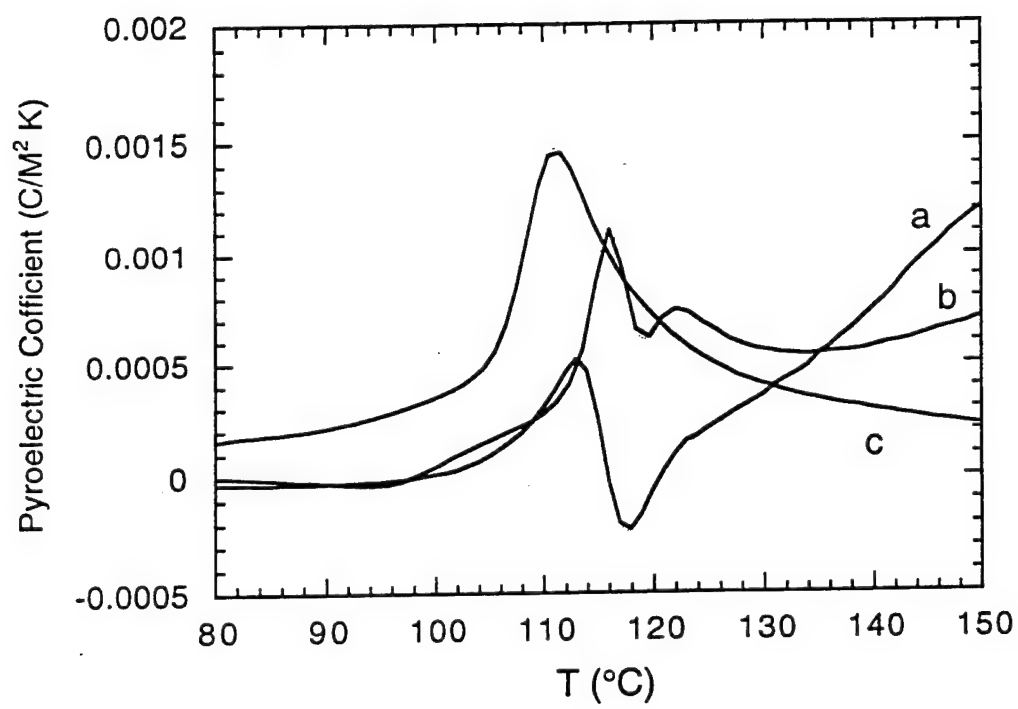














# **APPENDIX 13**

# Low-Temperature Observation of Relaxor Ferroelectric Domains in Lead Zinc Niobate

Maureen L. Mulvihill,<sup>1,\*</sup> L. Eric Cross,<sup>1</sup> and Kenji Uchino<sup>2</sup>

International Center for Actuators and Transducers (ICAT), Materials Research Laboratory, The Pennsylvania State University, University Park, Pennsylvania 16802

Domain reorientation in single crystals of lead zinc niobate-lead titanate solid solutions was examined, because the reorientation contributes to the electrically controlled change of shape and change of response in piezoelectric transducers and actuators. An optical microscope technique was used to explore the buildup of macropolar domains from micropolar regions in relaxor compositions. Poorly defined "ambiguous" spindlelike domains changed to distinct lamellar domains as  $\text{PbTiO}_3$  content was increased. The domain walls in  $\text{Pb}(\text{Zn}_{1-x}\text{Nb}_{2x})\text{O}_3$ -rich samples moved with a wavelike motion. The motion ceased or "froze-in" below  $-130^\circ$  and  $-30^\circ\text{C}$  for field-biased and nonbiased samples, respectively. The domains were observed at various temperatures from  $300^\circ$  to  $-185^\circ\text{C}$  and electric fields up to  $\pm 10\text{ kV/cm}$ .

## I. Introduction

RELAXOR ferroelectrics have large dielectric constant maximum and broad phase transition regions due to the complex perovskite crystal structure.  $\text{Pb}(\text{Zn}_{1-x}\text{Nb}_{2x})\text{O}_3$  (PZN) has a complex perovskite structure in which the  $\text{Zn}^{2+}$  and  $\text{Nb}^{5+}$  are disordered on the B-site, which results in composition variations and corresponding fluctuations in the phase transition temperature from region to region. As a result, the phase transition is broad and occurs over a range of temperatures called the Curie region. The Curie region for PZN occurs near  $140^\circ\text{C}$ .<sup>1,2</sup> The symmetry of PZN above the transition is cubic,  $Pm\bar{3}m$ , and below the transition is rhombohedral,  $3m$ .<sup>3</sup>  $\text{PbTiO}_3$  (PT) has a first-order phase transition at  $490^\circ\text{C}$  and a tetragonal,  $4mm$ ,<sup>4</sup> perovskite structure below its phase transition. In PT, a Curie point rather than a Curie region occurs, because there is no variation in local composition on the B-site. The system  $(1-x)\text{Pb}(\text{Zn}_{1-x}\text{Nb}_{2x})\text{O}_3$ - $x\text{PbTiO}_3$  (PZN-PT) forms a complete solid solution up to  $x = 0.2$ . PZN-PT has a morphotropic phase boundary (MPB) at  $x = 0.1$  between the rhombohedral and tetragonal phases at  $25^\circ\text{C}$ , as illustrated in Fig. 1.<sup>5</sup>

Static ferroelectric domains have been observed by methods such as etching the sample with acid and observing the exposed domains with an optical microscope<sup>6</sup> or thinning the sample and observing domains using transmission electron microscopy (TEM).<sup>7</sup> However, observing switching domains under an applied electric field or with changing temperature is difficult; this limits research on domain motion.

Lead zinc niobate-based single crystals were studied, because of their potential applications in actuators and transducers. Since the domain reorientation mechanisms contribute

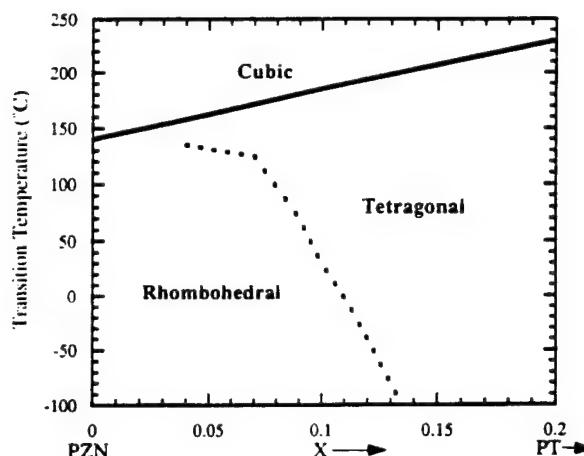


Fig. 1. Phase diagram of the  $\text{Pb}(\text{Zn}_{1/3}\text{Nb}_{2/3})\text{O}_3$ - $\text{PbTiO}_3$  solid-solution system taken from Kuwata *et al.*<sup>5</sup>

to the dielectric and piezoelectric properties, it is important to understand the domain reorientation so that the actuators and transducer properties can be tailored. In this study, an optical microscope technique was used to explore the growth of macrodomains from micropolar regions in relaxor compositions,  $\text{Pb}(\text{Zn}_{1/3}\text{Nb}_{2/3})\text{O}_3$ - $\text{PbTiO}_3$ , as functions of temperature and applied electric field.

## II. Experimental Procedure

Single crystals of PZN-PT were grown using a flux method with excess  $\text{PbO}$ .<sup>8</sup> The Laue X-ray technique was used to precisely determine the  $\langle 011 \rangle$  and  $\langle 111 \rangle$  directions in the crystals. The crystals were then sliced parallel to the  $\langle 011 \rangle$  plane, ground to a thickness of  $100\text{ }\mu\text{m}$ , and polished with diamond paste until a near-mirror finish was obtained on both surfaces. The samples were gold-sputtered, leaving a  $400\text{ }\mu\text{m}$  gap on the surface. Silver leads were attached to the sample with air dry silver paste. Figure 2 represents a schematic of an electroded sample. The samples were annealed above  $300^\circ\text{C}$  to remove the ferroelastic macrodomains in the material which were produced during the polishing operation. The removal of these ferroelastic macrodomains permitted the formation of the ferroelectric microdomains,<sup>9</sup> making the growth of macrodomains from microdomains observable.

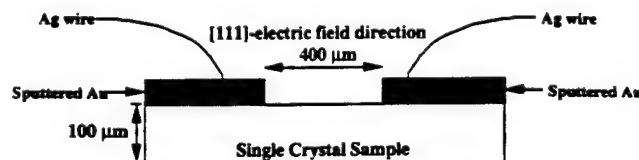


Fig. 2. Schematic of an electroded sample used in this study.

T. E. Mitchell—contributing editor

Manuscript No. 194076. Received November 5, 1993; approved June 28, 1995. Presented at the 95th Annual Meeting of the American Ceramic Society, Cincinnati, OH, April 20, 1993 (Paper No. 19-SXVIIIP).

Supported by the Office of Naval Research under Grant No. N00014-91-J-4145.

\*Member, American Ceramic Society.

Received Third Place Award in Graduate Student Poster Competition at the 95th Annual Meeting of the American Ceramic Society.

Samples with 100 and 90.5 mol% PZN (rhombohedral symmetry) were observed in this study as a function of temperature under a cyclic applied electric field parallel to the (111) axis. The (111) direction is the polarization axis for crystals with rhombohedral symmetry.

A high-resolution CCD (charged coupled device) camera was attached to a Nikon transmission petrographic microscope which was connected to a monitor and VCR (illustrated in Fig. 3). The birefringence between the domains permitted the observation of the domains with the polarizing light microscope. The microscope system also allows magnifications up to 1300X on the monitor. The temperature-controlled sample stage (Linkam) in conjunction with the deep focal point of the objective lenses allowed an electric field to be safely applied across the sample between 600° and -185°C. The stationary and switching domains were instantaneously recorded by the VCR and observed on the monitor.

### III. Experimental Results and Discussion

The variation of domain shape can be observed between rhombohedral domains (100% PZN) and a combination of rhombohedral and tetragonal domains (0.905PZN-0.095PT). The electrode configuration in this study allowed only observation of the two-dimensional shape of the domains. Rhombohedral domains can be described as having an ambiguous spindlelike morphology. "Spindlelike" refers to the domains being very wide in the middle and drawing to a point on each end. "Ambiguous" refers to the variation of domain widths and lengths which appear as an interpenetrating structure. The degree of the interpenetrating structure makes it very difficult to observe individual domains. The switching rhombohedral domains move across the sample with a wavelike motion. Tetragonal domains, in contrast, appear to have a well-defined lamellar morphology and are either at right angles or antiparallel. Therefore, even though the width and lengths of the tetragonal domains vary, the divisions between the domains are well defined, and no interpenetrating structure is observable.

The domain switching observations shown in Figs. 4 through 7 are in good agreement with the previous work done on PZN-PT.<sup>10,11</sup> The (011) plane is parallel to the plane of the

paper, and the [111] and [011] directions are labeled on each photograph. Each photograph is a single frame copied from the VCR tape. Therefore, on each photograph, three white boxes were printed, which were recorded during the experiment. The upper-left-hand box lists the time in hours, minutes, and seconds. The upper-right-hand box lists the date as the day, month, and year. The lower-left-hand box lists rate per minute, actual temperature, and the set temperature.

#### (1) Domain Change with Temperature

Figures 4(a) through (e) show a series of photographs of a moving domain wall taken from a 0.905PZN-0.095PT single crystal. The temperature was decreased from -8°C to -25°C without applying an electric field. With this sample, it was optically observed that domain wall motion could be driven by a thermal gradient without being electrically biased at low temperatures. A domain wall moved from the upper-right corner (Fig. 4(a) at -8°C) diagonally to the lower-left corner (Fig. 4(e) at -25°C). More spindlelike domains developed at -20°C (Fig. 4(c)), then combined to form a larger domain at lower temperatures, as shown in Fig. 4(e) at -25°C. The domain motion froze-in near -30°C.

#### (2) Domain Change with Electric Field

Figures 5(a) through (e) are photographs of the switching domains for a 100% PZN single crystal at a constant temperature of 25°C with an ac electric field. Total domain reversal occurred after one cycle of an ac field at  $\pm 5$  kV/cm at 0.05 Hz. The high density of macrodomains in these figures were caused by the application of the ac field for many cycles. The domain orientation returned to near the same position when the observed domains were compared between Figs. 5(a) and (e). These figures show five still photographs over a 15-s period (one cycle = 20 s). The domain wall switching observed in Figs. 5(a) through (e) is similar to the  $\text{Pb}(\text{Mg}_{1/3}\text{Nb}_{2/3})\text{O}_3$  single-crystal domains seen by Bokov and Myl'nikova.<sup>1</sup> It is very interesting that, even at an ac electric field as high as 10 kV/cm, the domains did not revert a single domain state, but maintained a spindlelike, interpenetrating structure with nearly constant width. Normal ferroelectrics, such as  $\text{BaTiO}_3$ , do not exhibit this phenomenon, but can be switched to a monodomain state by a high applied electric field.

#### (3) Domain Change with Applied Electric Field While Changing Temperature

The sample in Figs. 6(a) through (e) is a 100% PZN single crystal in which the temperature was raised from -114°C to -36°C with an ac field of  $\pm 7.5$  kV/cm. The domain motion was frozen-in below -130°C, but began slowly as temperature was increased. The domain motion appeared to nucleate in island regions on the crystal surface, which is marked by arrows on Figs. 6(a) through (c). The domains switched across the entire crystal by -53°C, as shown in Fig. 6(d). The switching speed increased as the temperature increased. As temperature increased, the size of the island regions increased, and eventually the domains on the entire surface began switching orientations with the field, which can be optically observed in Figs. 6(a) through (e). A slight temperature hysteresis also occurred between heating and cooling. The domain motion on cooling froze-in at -130°C, but on heating unfroze at -125°C.

Figure 7 shows the domain switching as a function of decreasing temperature with an electric field of  $\pm 10$  kV/cm at 0.05 Hz for the morphotropic phase boundary (MPB) composition 0.905PZN-0.095PT. The temperature was decreased from 191°C (paraelectric state) to -66°C (ferroelectric state). For this sample, domain motion froze-in near -130°C. Microdomain fluctuations caused birefringence changes which were optically observed above the Curie temperature of 182°C, as shown in Fig. 7(a). The large polar fluctuations in the paraelectric phase above the Curie temperature permitted the alternating field to force a phase change from a paraelectric state with large mobile micropolar regions to a ferroelectric state in which

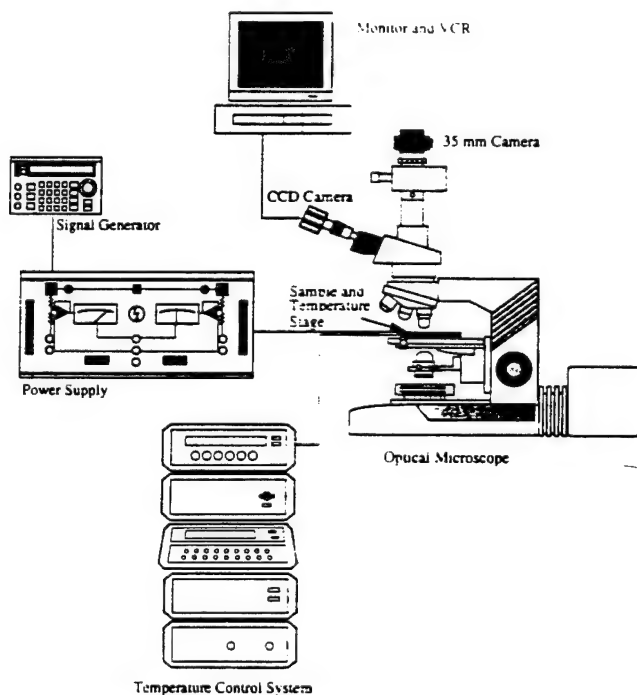
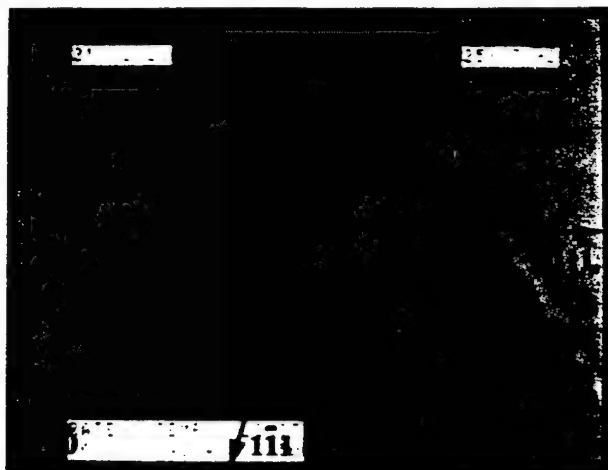
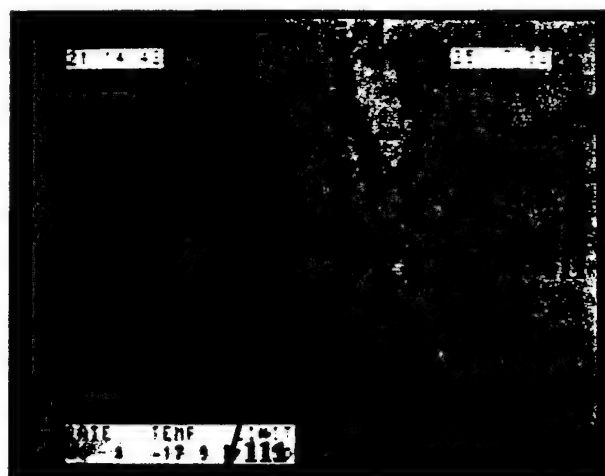


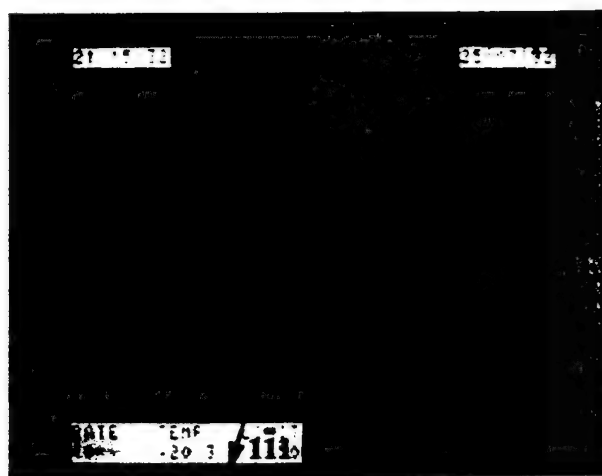
Fig. 3. CCD microscope system used at the Materials Research Laboratory.



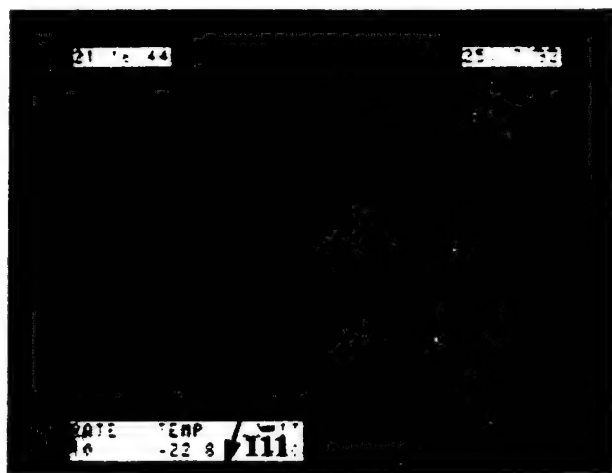
(a)



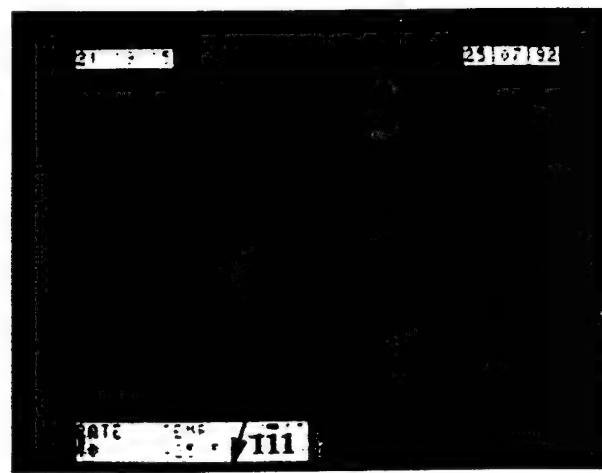
(b)



(c)



(d)

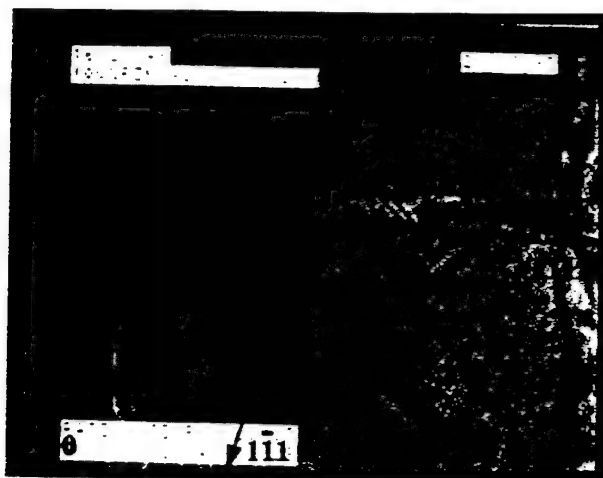


(e)

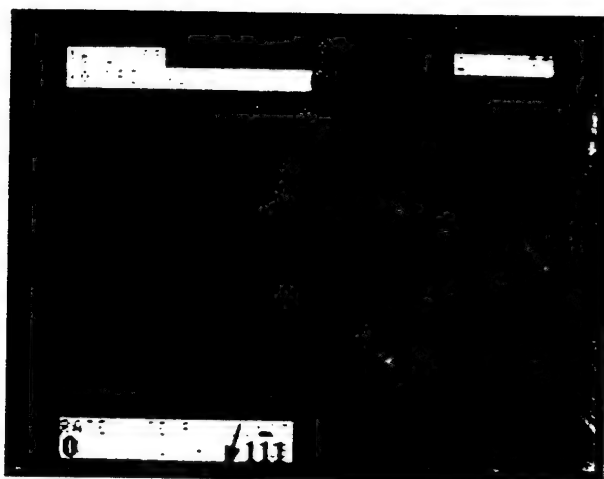
Fig. 4. Domain change with temperature for a 0.905/0.095 PZN-PT composition: (a)  $-8^{\circ}\text{C}$ , (b)  $-17^{\circ}\text{C}$ , (c)  $-20^{\circ}\text{C}$ , (d)  $-22^{\circ}\text{C}$ , (e)  $-25^{\circ}\text{C}$ . The plane of the photograph is parallel to the (011), and the crystallographic directions and scale bar are marked on each figure.

a domain structure became apparent.<sup>9</sup> As the temperature decreased, the domain morphology changed from a lamellar to a spindlelike pattern because of the phase transition from tetragonal to rhombohedral, as shown in Figs. 7(b) through (e). Both spindlelike and lamellar domains were observed at

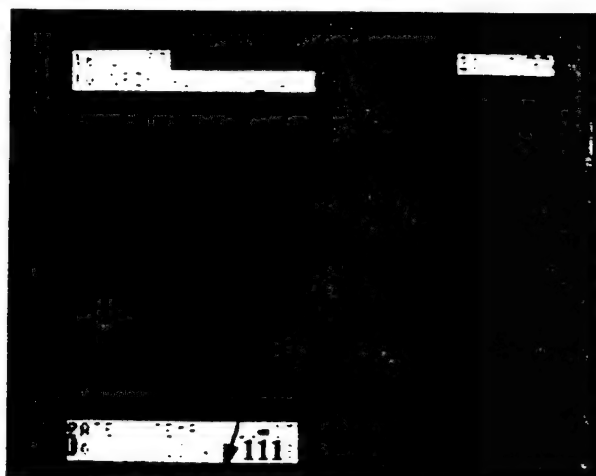
$+53^{\circ}\text{C}$ , as shown in Fig. 7(b). In this temperature range, the domain motion was more complicated because both the rhombohedral and tetragonal phases were present. At  $-4^{\circ}\text{C}$ , the density of spindlelike domains increased and the density of lamellar domains decreased, shown in Fig. 7(c). By  $-66^{\circ}$  and



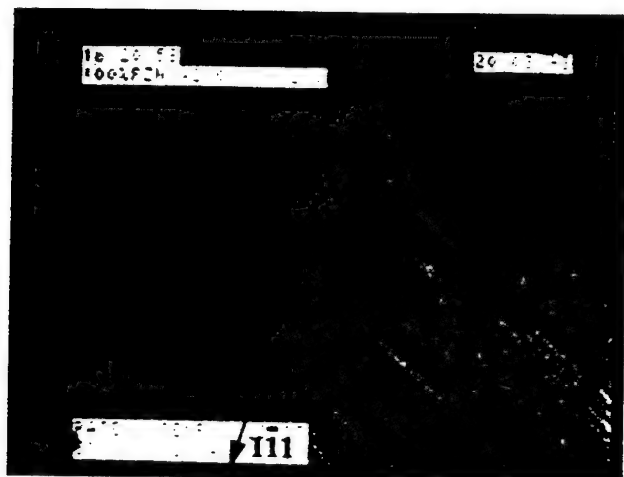
(a)



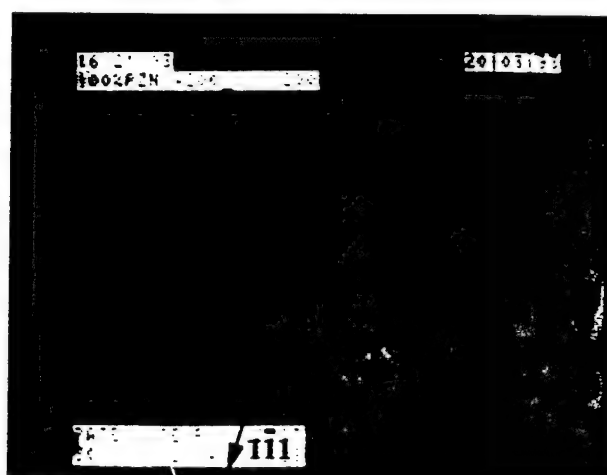
(b)



(c)

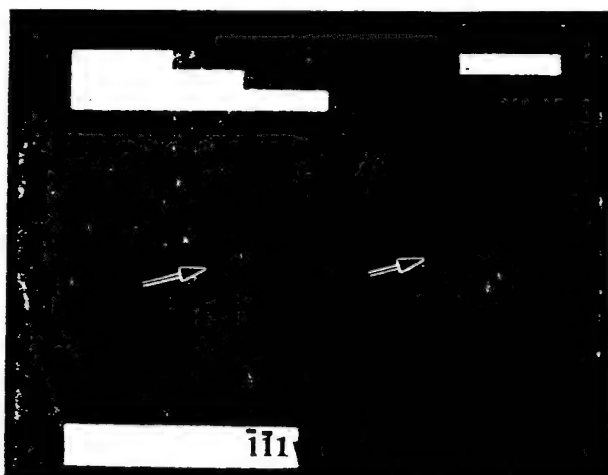


(d)

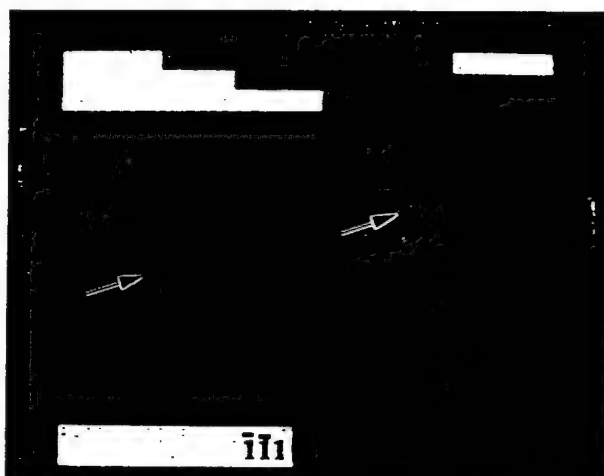


(e)

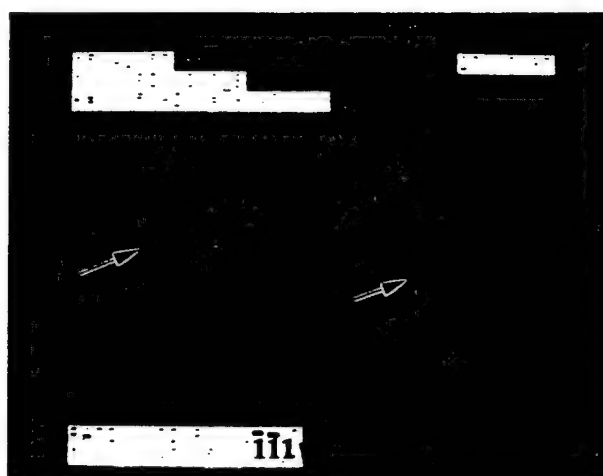
Fig. 5. Domain change with an electric field of  $\pm 5$  kV/cm at 28°C for a 100% PZN single crystal: (a) 5 kV/cm, (b) -2.5 kV/cm, (c) -4 kV/cm, (d) -5 kV/cm, (e) 0 kV/cm. The plane of the photograph is parallel to the (011), and the crystallographic directions and scale bar are marked on each figure.



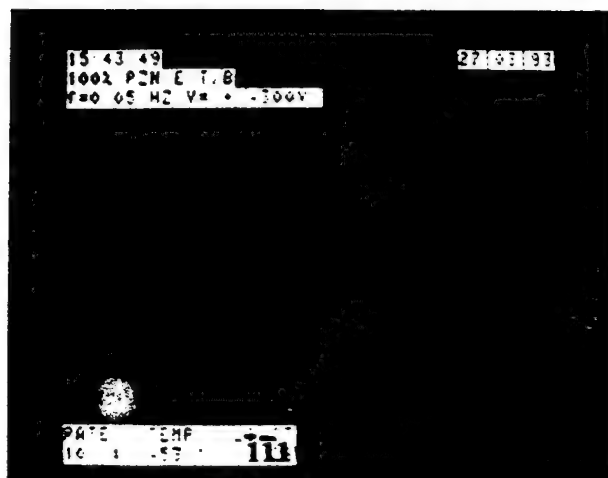
(a)



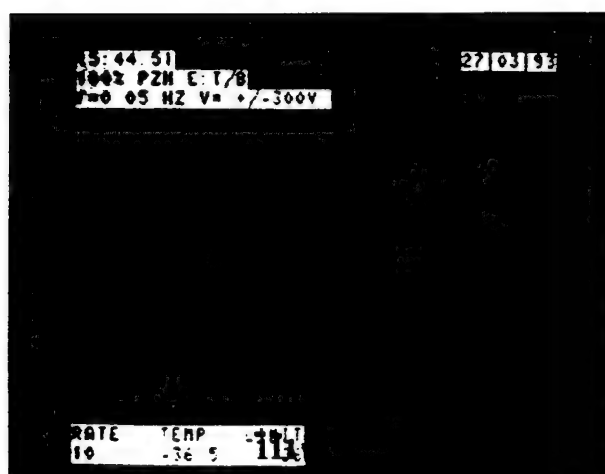
(b)



(c)

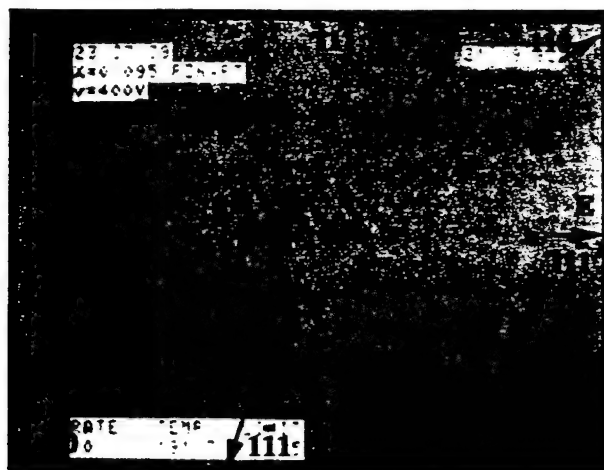


(d)

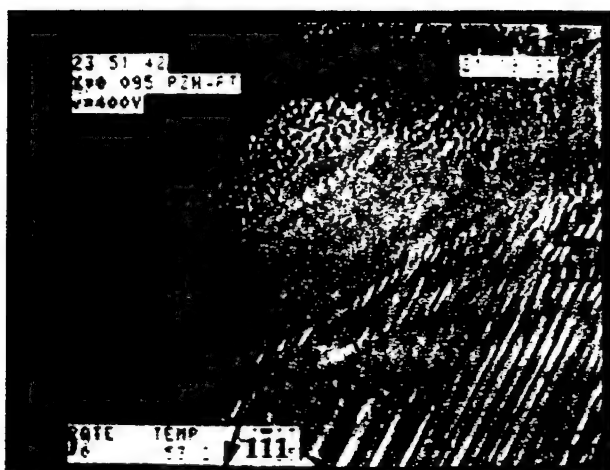


(e)

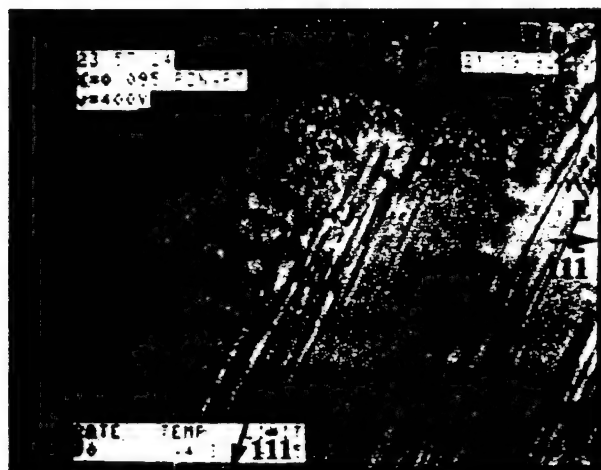
Fig. 6. Domain change under an applied electric field of  $\pm 7.5$  kV/cm with changing temperature for a 100% PZN single crystal: (a)  $-114^\circ\text{C}$ , (b)  $-85^\circ\text{C}$ , (c)  $-70^\circ\text{C}$ , (d)  $-53^\circ\text{C}$ , (e)  $-36^\circ\text{C}$ . The plane of the photograph is parallel to the (011), and the crystallographic directions and scale bar are marked on each figure.



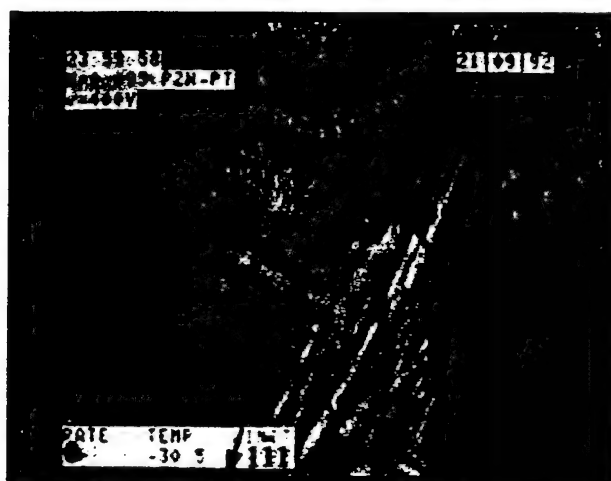
(a)



(b)



(c)



(d)



(e)

Fig. 7. Domain change under an applied electric field of  $\pm 10.0$  kV/cm with changing temperature for a 0.905/0.095 PZN-PT single crystal: (a) 191°C, (b) 53°C, (c) -4°C, (d) -30°C, (e) -66°C. The plane of the photograph is parallel to the (011), and the crystallographic directions and scale bar are marked on each figure.

-119°C, only spindlelike domains were observed. These observations can be supported by the phase evolution in the PZN-PT phase diagram shown in Fig. 1 for the composition 0.905PZN-0.095PT. At temperatures above 182°C, this composition has a cubic structure, while at temperatures between 182° and 25°C, it has tetragonal structure. However, at 25°C, rhombohedral and tetragonal structures coexist, which convert completely to rhombohedral below 25°C. The macrodomain morphologies which are representative of these different regions on the phase diagram were observed optically in Figs. 7(a) through 7(e).

#### IV. Summary

Domains in PZN-PT changed from ambiguous spindlelike to distinct lamellar domains as PbTiO<sub>3</sub> content was increased. This difference may be partially due to the crystallographic structure change from rhombohedral to the tetragonal phase. The domain walls moved with a wavelike motion in the 100% PZN compositions. The MPB composition of 0.905PZN-0.095PT had a more complicated domain wall motion than the other compositions, because the MPB composition has coexisting tetragonal and rhombohedral domains. The successive phase transitions from rhombohedral to tetragonal and tetragonal to cubic were also observed as the temperature increased. The freeze-in temperature for domain motion was successfully observed by optical microscopy. The observed freeze-in temperatures for pure PZN were -130 and -30°C for field-biased

and nonbiased samples, respectively. Quantitative analyses on the domain switching speed and the frozen island size will be reported in following papers.

**Acknowledgments:** The authors would like to thank Dr. Russell P. Brodeur, Mr. Roger B. Bagwell, and Ms. Heather T. Hawkins for the insightful discussions and editing.

#### References

- V. A. Bokov and I. E. Myl'nikova, "Ferroelectric Properties of Monocrystals of New Perovskite Compounds," *Sov. Phys.-Solid State*, **2** [11] 2428 (1961).
- N. P. Khuchua, V. A. Bokov, and I. E. Myl'nikova, "Dielectric Properties of  $\text{Pb}(\text{Zn}_{1-x}\text{Nb}_x)\text{O}_3$ , a Ferroelectric with an Indistinct Phase Transition," *Sov. Phys.-Solid State*, **10** [1] 194 (1968).
- Powder Diffraction File, Card No. 22-663, International Centre for Diffraction Data, Newtowne Square, PA, 1991.
- Powder Diffraction File, Card No. 42-4, International Centre for Diffraction Data, Newtowne Square, PA, 1991.
- J. Kuwata, K. Uchino, and S. Nomura, "Phase Transitions in  $\text{Pb}(\text{Zn}_{1-x}\text{Nb}_x)\text{O}_3$ - $\text{PbTiO}_3$  System," *Ferroelectrics*, **37**, 579 (1981).
- G. Arlt and P. Sasko, "Domain Configuration and Equilibrium Size of Domains in  $\text{BaTiO}_3$  Ceramics," *J. Appl. Phys.*, **51** [9] 4956 (1980).
- C. A. Randall, D. J. Barber, and R. W. Whatmore, "Ferroelectric Domain Configuration in a Modified PZT Ceramic," *J. Mater. Sci.*, **22**, 925 (1987).
- Y. Yokomizu, T. Takahashi, and S. Nomura, "Ferroelectric Properties of  $\text{Pb}(\text{Zn}_{1-x}\text{Nb}_x)\text{O}_3$ ," *J. Phys. Soc. Jpn.*, **28** [5] 1278 (1970).
- J. Kuwata, K. Uchino, and S. Nomura, "Diffuse Phase Transition in Lead Zinc Niobate," *Ferroelectrics*, **22**, 863 (1979).
- K. Kato, K. Suzuki, and K. Uchino, "Observation of the Domain Motion in Ferroelectric Single Crystals with a Diffuse Phase Transition," *J. Ceram. Soc. Jpn.*, **98**, 820 (1990).
- R. Ujue and K. Uchino, "Dynamical Domain Observation in Relaxor Ferroelectrics," *Ultrason. Symp. Proc.*, **2**, 725 (1990).





# **APPENDIX 14**

# DYNAMIC MOTION OF THE DOMAIN CONFIGURATION IN RELAXOR FERROELECTRIC SINGLE CRYSTALS AS A FUNCTION OF TEMPERATURE AND ELECTRIC FIELD.

MAUREEN L. MULVIHILL, L. ERIC CROSS, and KENJI UCHINO

International Center for Actuators and Transducers (ICAT), Materials Research Laboratory, The Pennsylvania State University, University Park, PA. 16802, USA, (814) 865-9931. Funding provided by the US Office of Naval Research.

**Abstract** Relaxor ferroelectrics exhibit unique characteristics such as a broad phase transition and frequency dispersion which may originate from the configuration of ferroelectric microdomains. In this study, the dynamic behavior of the macrodomains in  $\text{Pb}(\text{Zn}_{1/3}\text{Nb}_{2/3})\text{O}_3$  single crystals was observed using an optical microscope in combination with a CCD camera system. Many domain characteristics such as changes in birefringence, transition between microdomains and macrodomains, and "freeze-in" temperature of the macrodomains were optically observed. These observations were then compared to measured dielectric properties in an attempt to clarify the relationship between the dielectric properties and the behavior of macrodomains.

## INTRODUCTION

The observation of switching domains under an applied electric field and changing temperature has been difficult and limited research has been documented.<sup>1-3</sup> In this study, an optical technique was used to explore the growth of macrodomains from micropolar regions in the relaxor composition  $\text{Pb}(\text{Zn}_{1/3}\text{Nb}_{2/3})\text{O}_3$  (PZN) as a function of temperature and applied electric field. Lead zinc niobate based single crystals were studied because of their large dielectric ( $K \approx 56,000$  along  $\langle 111 \rangle$ ) and piezoelectric ( $k_{33}^* \approx 92\%$  along  $\langle 001 \rangle$ ) properties which make PZN a potential material for actuator and transducer devices.<sup>4</sup> The measured dielectric constant and dielectric loss as a function of temperature for a poled and unpoled sample were compared to the optically observed domain behaviors to develop a fundamental understanding of the relaxor ferroelectric behavior in PZN.

## EXPERIMENTAL PROCEDURE

Single crystals of PZN were grown using a flux method with excess PbO. The Laué x-ray technique was used to precisely determine the  $[111]$  directions in the crystals. The crystals were then sliced, ground to a thickness of 100  $\mu\text{m}$ , and polished with diamond paste until a near-mirror finish was obtained on both surfaces. The PZN domain

configurations were observed through the single crystal along the  $\langle 111 \rangle$  which is the spontaneous polarization direction of PZN. The electric field was applied as a triangular wave at 0.05 Hz up to  $\pm 10$  kV/cm and the temperature was cycled between  $-185^\circ\text{C}$  and  $200^\circ\text{C}$ . A high resolution CCD (Charged Coupled Device) camera was attached to a Nikon Transmission Petrographic Microscope which was connected to a monitor and VCR.<sup>2,3</sup> The temperature-controlled sample stage in conjunction with the deep focal point of the objective lenses allowed an electric field to be safely applied across the sample.

## RESULTS AND DISCUSSION

### Optical Observation

The CCD camera microscope system was used to observe macrodomain behaviors of PZN such as birefringence change, microdomain to macrodomain phase transition and "freeze-in" temperature. The color change due to the birefringence appeared under the applied electric field around the Curie temperature range ( $T_c \approx 140^\circ\text{C}$ ). The birefringence appeared at higher temperatures as the magnitude of the electric field increased, and was possibly caused by the microdomain alignment. The electric field caused the fluctuating microdomains to orient with the field leading to macroscopic birefringence in the crystal.

Still photographs of a 100% PZN single crystal at  $100^\circ\text{C}$  as the electric field increased are represented in Figures 1a through 1d. Macrodomains were not observed for the annealed state without the application of an electric field, but were first detected when the AC field was raised to 0.7 kV/cm. With an AC bias during field-cooling and field-heating, the phase transition from a ferroelectric (FE) microdomain to a macrodomain state occurred near  $130^\circ\text{C}$ .

As the temperature decreased, the domain motion ceased or "froze-in" at a temperature which was electric field dependent. Small frozen islands appeared randomly in the crystal which expanded with decreasing temperature.<sup>3</sup> This freezing phenomenon is not directly related to the coercive field and is not observed in normal ferroelectrics such as  $\text{BaTiO}_3$ . It was optically observed that the freezing temperature decreased as the electric field increased. On field heating, the thawing or "unfreezing" temperature took place at temperatures slightly higher than the freeze-in temperature, indicating a slight temperature hysteresis.

### Dielectric Data

The dielectric constant and dielectric loss versus temperature at four frequencies for an unpoled and poled 100% PZN single crystal are shown in Figures 2 and 3, respectively. The dielectric constant and dielectric loss behavior exhibited above the transition temperature of  $\approx 140^\circ\text{C}$  were identical. The frequency dependent transition temperature

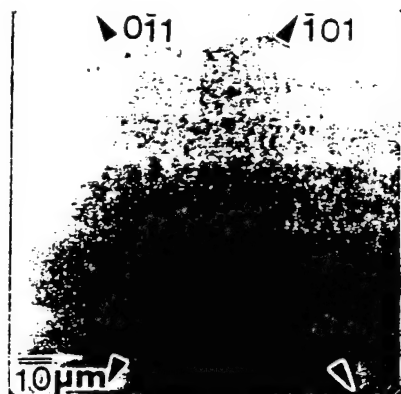


FIGURE 1a 100% PZN at 0 kV/cm.

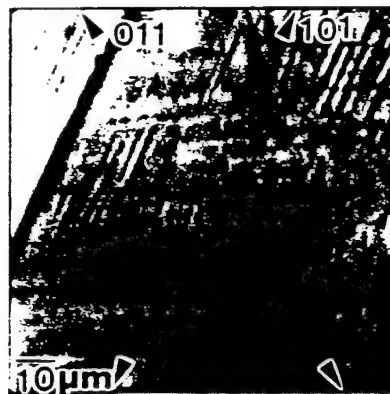


FIGURE 1b 100% PZN at 1 kV/cm.

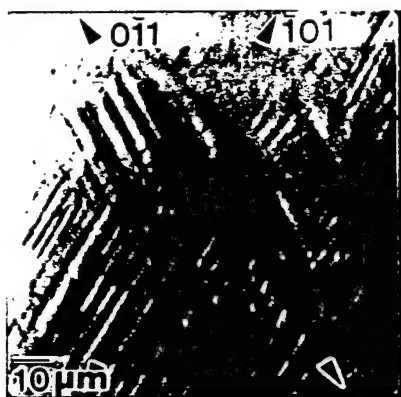


FIGURE 1c 100% PZN at 3.8 kV/cm.

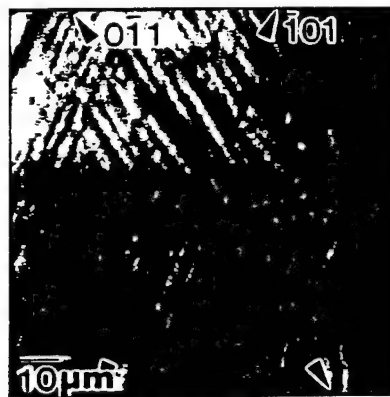


FIGURE 1d 100% PZN at 6.3 kV/cm.

corresponds to the border between paraelectric and FE microdomain phases. As temperature decreased, the dielectric behavior of the poled and unpoled sample near 100°C diverged. The frequency dispersion exhibited in the unpoled sample did not occur in the poled sample. The temperature region where the dielectric constant had a nondispersive frequency behavior appeared as a "shoulder" in the poled sample, as shown in Figure 3. Also, the  $\tan\delta$  decreased drastically in this temperature region. The decrease in  $\tan\delta$  and the shoulder in the poled sample were caused by the alignment of the

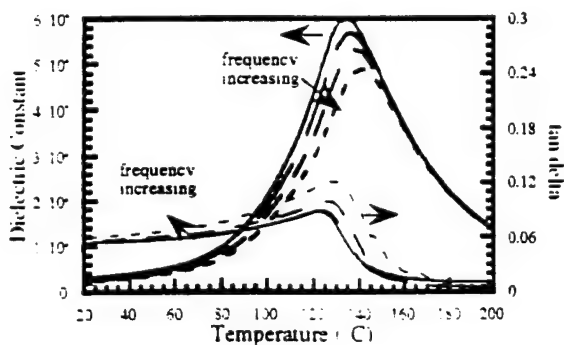


FIGURE 2 Unpoled PZN single crystal.

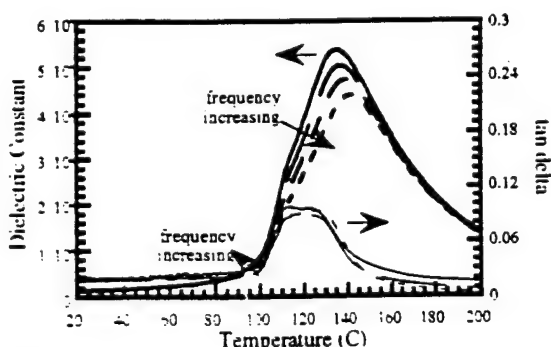


FIGURE 3 Poled PZN single crystal.

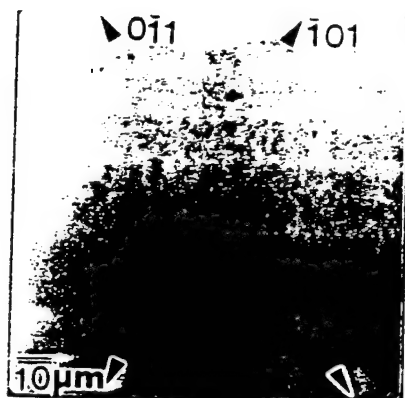


FIGURE 1a 100% PZN at 0 kV/cm.

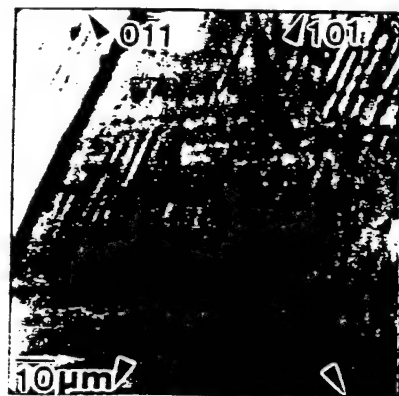


FIGURE 1b 100% PZN at 1 kV/cm.

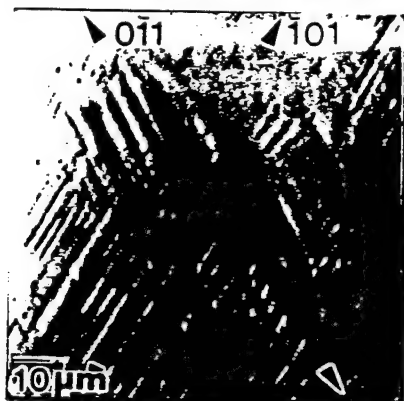


FIGURE 1c 100% PZN at 3.8 kV/cm.

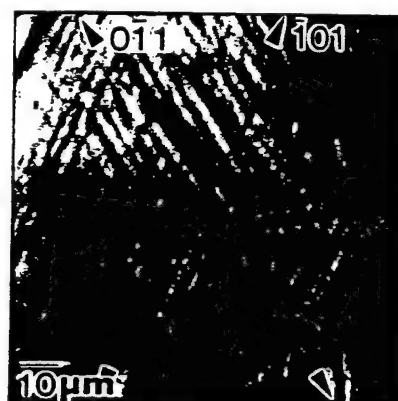


FIGURE 1d 100% PZN at 6.3 kV/cm.

corresponds to the border between paraelectric and FE microdomain phases. As temperature decreased, the dielectric behavior of the poled and unpoled sample near 100°C diverged. The frequency dispersion exhibited in the unpoled sample did not occur in the poled sample. The temperature region where the dielectric constant had a nondispersive frequency behavior appeared as a "shoulder" in the poled sample, as shown in Figure 3. Also, the  $\tan\delta$  decreased drastically in this temperature region. The decrease in  $\tan\delta$  and the shoulder in the poled sample were caused by the alignment of the

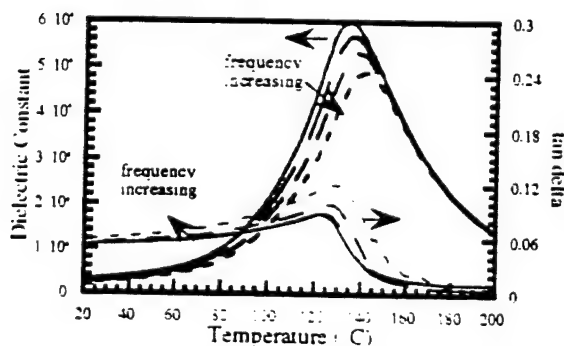


FIGURE 2 Unpoled PZN single crystal.

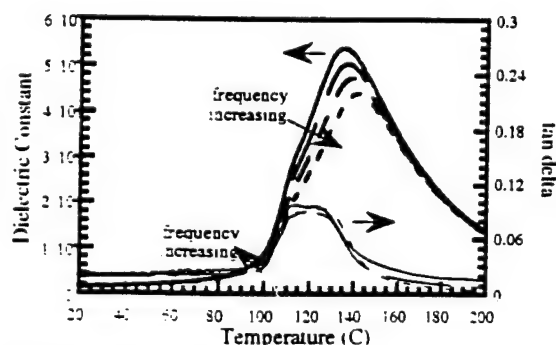


FIGURE 3 Poled PZN single crystal.

microdomains by the +15kV/cm DC poling bias. However, in the unpoled sample the microdomains were not aligned and variation in the orientation of the microdomains caused the frequency dispersion in the dielectric data. This temperature range corresponds to the ferroelectric microdomain phase region. The shoulder corresponds to a critical temperature ( $T_{crit}$ ) which is the phase border between FE microdomain and FE macrodomain.

#### Comparison of Optically Observed Domains and Dielectric Properties

The magnitude of the electric field as a function of temperature was plotted using the data from the optically observed characteristics and the measured dielectric properties, as shown in Figure 4. In conclusion, various trends in the data divided the figure into four phase regions as a function of temperature. Since the birefringence changes were caused by the induced micropolar alignment, it was assumed that the birefringence marked the first phase transition on decreasing temperature between paraelectric and FE microdomain phase regions. The second phase transition occurred at the temperature where the macrodomains appeared with field-cooling and disappeared with field-heating. This phase transition separated the FE microdomain phase from the FE macrodomain phase. The third phase transition occurred at the domain freeze-in temperature. This transition between the FE macrodomain phase and the FE frozen domain phase decreased to lower temperatures as the magnitude of the electric field increased.

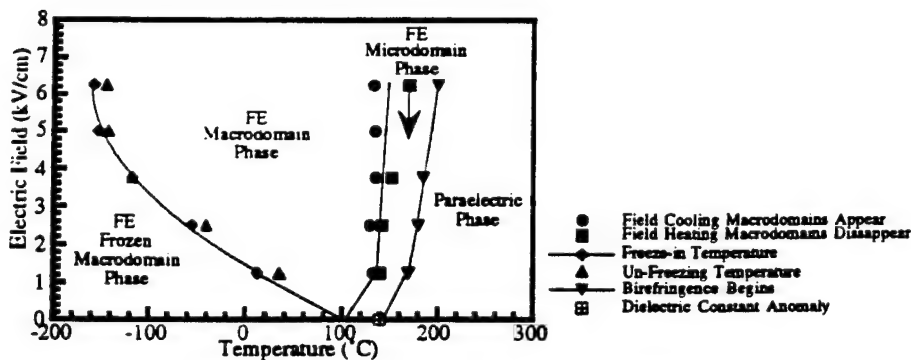


FIGURE 4 Optically observed behavior of the PZN macrodomains.

#### REFERENCES

1. K. Kato, K. Suzuki and K. Uchino, *J. Ceram. Soc. Jpn.*, **98** 840 (1990).
2. K.Y. Oh, K. Uchino, and L.E. Cross, *J. Am. Ceram. Soc.*, **77** [11] 2809 (1994).
3. M. L. Mulvihill, L. E. Cross, and K. Uchino, *J. Am. Ceram. Soc.*, accepted for publication.
4. J. Kuwata, K. Uchino and S. Nomura, *Ferroelectrics*, **37** 579 (1981).





# **APPENDIX 15**

# IN-SITU OBSERVATION OF THE DOMAIN CONFIGURATIONS DURING THE PHASE TRANSITIONS IN BARIUM TITANATE

Maureen L. Mulvihill<sup>†</sup>, Kenji Uchino<sup>†</sup>, Zhuang Li<sup>‡</sup> and Wenwu Cao<sup>†</sup>

<sup>†</sup>International Center for Actuators and Transducers (ICAT)  
Materials Research Laboratory, The Pennsylvania State University, University Park, PA 16802,  
USA.

<sup>‡</sup>Materials Science Division, Argonne National Laboratory, Argonne, IL. 60439, USA.

## § ABSTRACT

Using a polarizing optical microscope in conjunction with a CCD (charged coupled device) camera system, the domain microstructural evolution with respect to temperature in all three phases of BaTiO<sub>3</sub> was studied. Along a (001) oriented section the domains in the tetragonal phase form 90° domain patterns in an "a-a" configuration. The transition on heating and cooling between the cubic and tetragonal phases occurred near the same temperature, 125°C. On cooling, the domain structures in the orthorhombic phase appeared as long continuous lamellar structure, while on heating the domains formed a "patchwork" structure. This transition temperature showed a large thermal hysteresis. The final transition temperature from orthorhombic to rhombohedral was difficult to determine using this technique. The transition on cooling occurred at -134°C based on a color change and the disappearance of all the domains. During heating, the domains reappeared at -110°C and remained in a patchwork structure throughout the orthorhombic phase.

**KEYWORDS:** domains, ferroelectric, BaTiO<sub>3</sub>, phase transitions, polarizing optical microscope

## § 1.0 INTRODUCTION

### 1.1. Background of $\text{BaTiO}_3$

Since the discovery of the barium titanate ( $\text{BaTiO}_3$ ) crystal in 1943, many researchers have studied it due to its large dielectric, piezoelectric and elastic constants.  $\text{BaTiO}_3$  is used in many applications such as capacitors (Buessem, Cross and Goswami, 1966), electrooptic devices (Nakao, Tomomatsu, Ajimura, Kurosaka and Tominaga, 1994) and memory devices (Merz 1954; Cudney, Fousek, Zgonik, Günter, Garrett and Rytz, 1993). Domains, which are caused by multivariants in the spontaneous polarization and strain (Arlt and Sasko, 1980), contribute greatly to the physical properties of  $\text{BaTiO}_3$  (Arlt, 1990).

A domain is a uniform volume of spontaneous electrical polarization ( $P_s$ ) which can be formed on cooling from the paraelectric to ferroelectric (FE) phase or a transition between FE phases. Domains can be altered by temperature, pressure, electric field and past history of the material (Forsbergh, 1949). Domains develop in various configurations to balance the stress in the material so that the overall elastic energy is minimized (Arlt, 1987; Arlt, 1990; Kim, Chung and Kim, 1993). In some situations, certain kinds of domain patterns can be stabilized by defects (Cao, 1995). The domain configurations depend on the crystallographic symmetry of the material. Domain structures are of basic importance in FE polycrystals since the structures determine the mechanisms of the polarization reversal process. The presence of domain walls also affects the dielectric, elastic and piezoelectric properties since the walls are mobile under an external field (Fousek and Janovec, 1969).

$\text{BaTiO}_3$  (BT) has four phase stability regions as a function of temperature. The high temperature phase (greater than  $\sim 120^\circ\text{C}$ ) is a cubic perovskite. In 1949, Merz (1949) reported the dielectric constant as a function of temperature for BT. BT transformed from (c)ubic (paraelectric) to (t)etragonal (ferroelectric) at  $120^\circ\text{C}$ , to (o)rthorhombic (ferroelectric) at  $-7^\circ\text{C}$ , and to (r)hombohedral (ferroelectric) at  $-90^\circ\text{C}$ . On heating, the phase transitions of  $r \rightarrow o$ ,  $o \rightarrow t$ , and  $t \rightarrow c$  occurred at slightly higher temperatures than on cooling which signified the presence of latent heat and a first order transition (Kanata, Yoshikawa and Kubota, 1987). The polarization axes in the

ferroelectric phases are along the [001], [110] and [111] directions for the tetragonal, orthorhombic and rhombohedral phases, respectively (Merz, 1949; Cook, 1956). Since the polarization axis in each phase changes, the domain configuration also varies as the structure changes with temperature.

As BT transforms from the cubic to the tetragonal structure, the c-axis elongates and the lattice constant c/a ratio increases to 1.01 (DeVries and Burke, 1957). Strains develop and are relieved by the formation of domains with polarization along one of the three principal crystallographic axes. Due to the degeneracy of  $\pm P_s$ , there are six possible orientations in the tetragonal phase. In the tetragonal phase 90° and 180° domains occur. The 90° domain walls orient along one of the {101} planes (DeVries et al., 1957; Cao and Cross, 1991). The domains with polarization vectors antiparallel to each other are 180° domains. Optical microscopy cannot distinguish the 180° domains since the change of optical indices is only related to the strain and not direction.

As the temperature decreases below 0°C, BT transforms into the orthorhombic structure. The polarization axis changes to one of the twelve  $\langle 101 \rangle$  directions and the domains can meet with polarization vectors forming 60°, 90° and 180° angles (Smolenskii, 1982). As the temperature decreases even further to -80°C, BT transforms into the rhombohedral phase where the polarization axis goes to one of the eight  $\langle 111 \rangle$  directions, and there are 71°, 109° and 180° domain structures. Experimentally, it was observed that in contrast to the tetragonal phase, birefringence occurred in both the orthorhombic and rhombohedral phases (Smolenskii, 1982). Also, the actual changes in polarization were larger than expected in the orthorhombic and rhombohedral phases. It was suggested that the increase in polarization was possibly due to both the change in crystal axes and the change in the magnitude of polarization (Merz, 1949).

## 1.2. Microscopy Techniques used to Observe Domain Configurations

A significant amount of research has been conducted on BT since 1943 using various techniques such as optical (OM), scanning electron (SEM) and transmission electron (TEM) microscopes in an attempt to understand the relationship between the domain structures and the

properties of BT. Most of the research dealt with the effects of electric fields and compressive stresses on the tetragonal domain configurations. Due to the low temperature necessary to observe the orthorhombic and rhombohedral domain configurations, their configurations have not been studied as frequently as the tetragonal phase configurations.

Regions in which all polarization directions are parallel to the surface of the section are called "a" domains whereas regions perpendicular to the surface of the section are called "c" domains (Hooton and Merz, 1955). Using polarizing optical microscopy the "c" domains appear dark since the optic axis for a tetragonal phase is along the c-axis, whereas the "a" domains are bright (Merz, 1954). Hooton and Merz (1955), using optical microscopy were able to observe both 90° and 180° domains by etching BT samples with hydrochloric acid. They found that the positive end of the domain etched faster than the negative end of the polarization vector. Even though this technique proved successful for the observation of 90° and 180° domains, the method is destructive to the sample and not useful for dynamic studies.

Electron microscopic techniques have been used to obtain high resolution information concerning the domains and domain boundaries (Merz, 1949). Domain patterns must be etched to be observed using SEM. Due to the preferential etching, the "a", "+c" and "-c" domains appeared gray, dark and bright, respectively (Hu, Chan, Wen and Harmer, 1986). Park and Chung (1994) using SEM observed that the 90° and 180° domains formed a herringbone pattern when all three domains ("a", "+c" and "-c") were present. They also found that the spatial forms of the 90° and 180° domain boundaries formed irregular cross sections which appeared cylindrical.

When optical microscopy was compared to TEM, it was reported that the domain widths were much larger for bulk than thin film materials. The measured domain widths for bulk samples were tens of micrometers whereas for thin film techniques the widths were between hundredths or even thousandths of micrometers (Merz, 1949). It is believed that the bulk domains contain many smaller domains which were unobservable using optical microscopy.

In this study, domain creation and orientation changes for the three phase transitions in BT were observed as a function of temperature. The technique differs from previous studies since it is

in-situ, allowing domain configurations at each phase transition as well as in each ferroelectric phase to be observed in real time. Bulk domain behaviors can be determined without etching.

## § 2.0. EXPERIMENTAL PROCEDURE

The high quality barium titanate (BT) single crystal used in this study was obtained from the Institute of Physics, Chinese Academy of Science, Beijing China. The crystal was grown by the top seed solution method. As received, it was optically clear, free of imperfections, and untwined when examined under cross polarizers.

The Laué X-ray technique was used to precisely determine the  $\langle 001 \rangle$  family of directions in the crystal. The crystal was then sliced parallel to the (001) plane, ground to a thickness of 100  $\mu\text{m}$ , and polished with 0.5  $\mu\text{m}$  gamma-alumina in kerosene. The samples were gold sputtered on one side leaving a 400  $\mu\text{m}$  gap on the surface. Silver leads were attached to the electrodes with air dry silver paste. The samples were annealed above 200°C to remove any internal stresses in the material which were produced during the cutting and polishing operation.

A high resolution CCD (Charged Coupled Device) camera attached to a Nikon transmission optical microscope (TOM) was connected to a monitor and VCR as illustrated in Figure 1. The birefringence between the domains permitted the observation of the domains with the polarizing light microscope. Magnifications up to 1300X can be observed on the monitor. The temperature-controlled sample stage (Linkam Inc.) in conjunction with the deep focal point of the objective lenses allows the observation of domain behavior as a function of temperature between +200°C and -185°C at a rate of 10°C/min. The stationary and changing domains were instantaneously recorded by the VCR and observed on the monitor.

For the dielectric constant versus temperature measurements, the crystals were cut and polished to 100  $\mu\text{m}$  thick sections. Circular gold electrodes were sputtered on parallel surfaces with diameters of 1 ~ 2 mm. The capacitance and loss of an unpoled crystal section were measured as functions of temperature and frequency using a Hewlett Packard Programmable 4275A Multi-frequency LCR meter in a computer controlled furnace system. The samples were measured on cooling from 200°C down to -160°C at 1°C/min, then heated back to 200°C at 1°C/min.

### § 3.0. RESULTS AND DISCUSSION

A high quality BT single crystal section with (001) orientation was measured under transmission optical microscopy (TOM) as a function of temperature during several temperature cycles to determine domain configuration changes through the three ferroelectric phase transitions. These phase transitions were observed by the changes in the domain configurations and then compared with the measured dielectric constant. The (001) section contains several directions, as illustrated in Figure 2.

#### 3.1 Measured Dielectric Constant as a Function of Temperature

The dielectric constant as a function of temperature during heating and cooling for an unpoled BT single crystal measured along the [001] direction is shown in Figure 3. The phase transitions temperatures of this crystal occurred at slightly higher temperatures than those measured by Merz (1949). In this experiment, the  $c \leftrightarrow t$  phase transitions occurred at 125°C on cooling and at a slightly higher temperature, 127°C on heating whereas the  $c \leftrightarrow t$  phase transition reported by Merz was 120°C. The other two phase transitions, i.e.,  $t \leftrightarrow o$  and  $o \leftrightarrow r$  showed larger thermal hystereses. The  $t \leftrightarrow o$  phase transitions occurred near 2.5°C on cooling and 10°C on heating, and the  $o \leftrightarrow r$  phase transitions occurred at -100°C on cooling and -90°C on heating.

#### 3.2. Optical Observation of the Cubic $\leftrightarrow$ Tetragonal Phase Transitions

For each of the three thermal cycles, the cubic to tetragonal phases transition occurred at the same temperature of 125°C on cooling which was in agreement with the  $c \leftrightarrow t$  phase transition temperature of the measured dielectric constant shown in Figure 3. A small thermal hysteresis was observed as the sample was heated back through the tetragonal to cubic transition which occurred near 127°C.

In the cubic phase above 125°C, the sample appeared to be a uniform color. On cooling, wedge shaped domains appeared at 125°C as shown in Figure 4(a). These wedge shaped domains elongated and widened with further cooling as shown in Figure 4(b) at 124.4°C. The isolated wedge domains grew into a more uniform twin band with domain walls oriented in  $[1\bar{1} 0]$ . Another set of twin bands is formed with the domain walls oriented along the  $[110]$  direction. At

122.3°C the entire sample contains tetragonal 90° domains as shown in Figure 4(c). One set of twin bands disappeared leaving only the twin band with domain walls oriented along  $[1\bar{1}0]$ . The lamellar domains had a wedge shape which traveled across the sample slowly as the temperature decreased until the entire sample was covered. Most of the domain growth occurred by 120°C. Afterwards, the domain width (1 ~ 5  $\mu\text{m}$ ) appeared to be saturated and did not change down to 2.4°C. The 90° domains formed an "a-a" configuration on the plane. The sample contained a high density of the long and sharp 90° domains. The colors of domains alternated yellow and green.

On heating, the tetragonal to cubic phase transition began at 124°C, signified by the disappearance of some domains. At 125°C the domains became very difficult to distinguish. At 126°C a swift shift to cubic phase occurred and all domains disappeared in a sweeping motion. However, even at 127°C, the sample still shows some birefringence. Uniform color appeared only at 128°C.

### 3.3. Optical Observation of the Tetragonal $\leftrightarrow$ Orthorhombic Phase Transitions

With further cooling down to 2.4°C the second phase transition started, which is from the tetragonal phase to the orthorhombic phase as shown in Figure 4(d). This phase transition took place within 0.4°C. It was also in agreement with the  $t \leftrightarrow o$  phase transition temperature in Figure 3. The orthorhombic phase domains grew across the sample in a sweeping motion with a narrow but finite temperature interval as illustrated in Figures 4(d), 4(e), and 4(f). The orthorhombic domains were long and well defined domains. A single set of twin bands with domain walls oriented in the  $[010]$  evolved from the original tetragonal domains with domain wall oriented in  $[1\bar{1}0]$ . The domain walls effectively rotated by 45°. The sample color changed to warmer colors (reds and oranges). Taking into account of the fact that the stripe period is similar in both the tetragonal and orthorhombic phases, this domain configuration change was caused to compensate the stress and charge distribution.

On heating, the orthorhombic to tetragonal phase transition occurred at a much higher temperature, 14.4°C. The phase transition took place within 0.5°C as shown in Figures 4(h) to 4(j). A moving interface perpendicular to the tetragonal domain walls swept across the sample,



changing the domain wall orientation back to nearly the same configuration as before the  $t \rightarrow o$  transition [Figure 4(c)]. The interface front which swept across the sample was not straight but slightly zigzagged. The period of this zigzag pattern corresponded roughly to that of a patchwork pattern. The recovered tetragonal phase consisted of long straight  $90^\circ$  domains similar to the  $90^\circ$  domains which appeared on cooling but with varying widths.

### 3.4. Optical Observation of the Orthorhombic $\leftrightarrow$ Rhombohedral Phase Transitions

The orthorhombic to rhombohedral phase transition temperature could not be clearly defined from the optical observation of the domain configurations. The observed phase transition temperatures varied from those shown in Figure 5. At  $-110^\circ\text{C}$  the sample still contained long orthorhombic domains as in Figure 4(j). At  $-123^\circ\text{C}$  the sample darkened and the color became less orange and red, but the pattern was the same as that in Figure 4(g) in which the domain walls were oriented along the  $\langle \bar{1} 00 \rangle$ . The domains disappeared instantaneously at  $-134^\circ\text{C}$  probably reflecting the orthorhombic to rhombohedral phase transition, as shown in Figure 4(f). However, in the area near a crack, domains were still present. These domains are possibly caused by the residual strain of the crack (Cao and Krumhansl, 1990). The sample stayed in a uniform color down to  $-185^\circ\text{C}$ .

On heating to  $-110.4^\circ\text{C}$  no domains were observed as shown in Figure 4(k). At  $-110.3^\circ\text{C}$ , a cross hatching of the twin bands or a "patchwork" domain structure of purple color was observed as shown in Figure 4(l). The domain wall oriented along both the  $[\bar{1} 00]$  and  $[010]$  directions. The width of the patchwork squares was approximately  $10 \sim 50 \mu\text{m}$  in size. This pattern may have originated from the rhombohedral domain period which has not been clarified in this work. At  $-5.3^\circ\text{C}$  the brightness of the sample increased dramatically but the domain patterns remain the same as shown in Figure 4(h). The patchwork domain patterns existed up to  $14.6^\circ\text{C}$  where the sample went through the orthorhombic-tetragonal phase transition, shown in Figure 4(i).

## § 4.0. SUMMARY

A polarizing microscope in combination with a CCD camera system allowed the in-situ observation of the phase transition in barium titanate and the associated domain structures for

temperatures cycled between 200°C and -185°C. The domain configuration in each of the three phases had its own orientation and morphology. The transitions all appeared to be first order due to the existence of thermal hysteresis.

In the tetragonal phase, several twin bands were nucleated and later merged into a single set of twin bands with the domain wall oriented along the  $\langle 110 \rangle$  directions. The width of the domains was in the range of 1 ~ 5  $\mu\text{m}$  and did not seem to change significantly with temperature. The orthorhombic domains were different when the system was transformed from the high temperature phase or from the low temperature phase. On cooling, the system transformed into a single set of twin bands from the twin bands of the tetragonal phase via a propagating habit plane perpendicular to the tetragonal domain walls. In contrast, a patchwork pattern formed on heating. The patchwork domain structure transformed to the tetragonal twin band via a zigzagged interface of an orientation near the  $[010]$ . No clear domain patterns were visible under the TOM in the rhombohedral phase.

#### ACKNOWLEDGMENTS

This work was supported by the Office of Naval Research under grant numbers N00014-91-J-4145 and N00014-92-J-1501.

#### § 5.0. REFERENCES

- ARLT, G., 1987, *Ferroelectrics*, **76**, 451.
- ARLT, G., 1990, *Ferroelectrics*, **104**, 217.
- ARLT, G. and SASKO, P., 1980, *J. Appl. Phys.*, **51**, 4956.
- BUESSEM, W.R., CROSS, L.E., and GOSWAMI, A.K., 1966, *J. Am. Ceram. Soc.*, **49**, 33.
- CAO, W. and KRUMHANS, J.A., 1990, *Phys. Rev. B*, **42** [7] 4334 (1990).
- CAO, W. AND CROSS, L.E., 1991, *Phys. Rev. B.*, **44**, 5.
- CAO, W., 1995, *Phase Transitions*, in press.

- CUDNEY, R.S., FOUSEK, J., ZGONIK, M., GÜNTER, P., GARRETT M.H., and RYTZ, D., 1993, Appl. Phys Lett. **63**, 3399.
- DEVRIES, R.C. and BURKE, J.E., 1957, J. Am. Ceram. Soc., **40**, 200.
- FORSBERGH, P.W., 1949, Phys. Review, **76**, 1187.
- FOUSEK, J. and JANOVEC, V., 1969, J. Appl. Phys., **40**, 135.
- HOOTON, J.A. and MERZ, W.J., 1955, Phys. Rev., **98**, 409.
- HU, Y.H., CHAN, H.M., WEN, Z.X., and HARMER, M.P., 1986, J. Am. Ceram. Soc., **69**, 594.
- KANATA, T., YOSHIKAWA, T., and KUBOTA, K., 1987, Solid State Comm., **62**, 765.
- KIM, S.-B., CHUNG, T.-J. and KIM, D.-Y., 1993, J. Euro. Ceram. Soc., **12**, 147.
- MERZ, W., 1949, Phys. Rev., **76**, 1221.
- MERZ, W., 1954, Phys. Rev., **95**, 690.
- NAKAO, O., TOMOMATSU, K., AJIMURA, S., KUROSAKA, A., and TOMINAGA, H., 1994, Ferroelectrics, **156**, 135.
- PARK, B.-M. and CHUNG, S.-J., 1994, Ferroelectrics, **157**, 27.
- SMOLENSKII, G.A., 1982, Ferroelectrics and Related Materials. Volume 3, Gordon and Breach Science Publishers, Chapter 7.

## LIST OF FIGURES

- Figure 1: Experimental set-up of CCD microscope system used in this study.
- Figure 2: An illustration of the directions contained in the (001) section.
- Figure 3: The measured dielectric constant versus temperature for an unpoled BT single crystal.
- Figure 4: High quality 100% BT single crystal as a function of temperature. (a) 125°C, (b) 124.4°C, (c) 122.3°C, (d) 2.4°C, (e) 2.2°C, (f) 2.0°C, (g) -135°C, (h) 14.4°C, (i) 14.6°C, (j) 14.9°C, (k) -110.4°C and (l) -110.3°C.

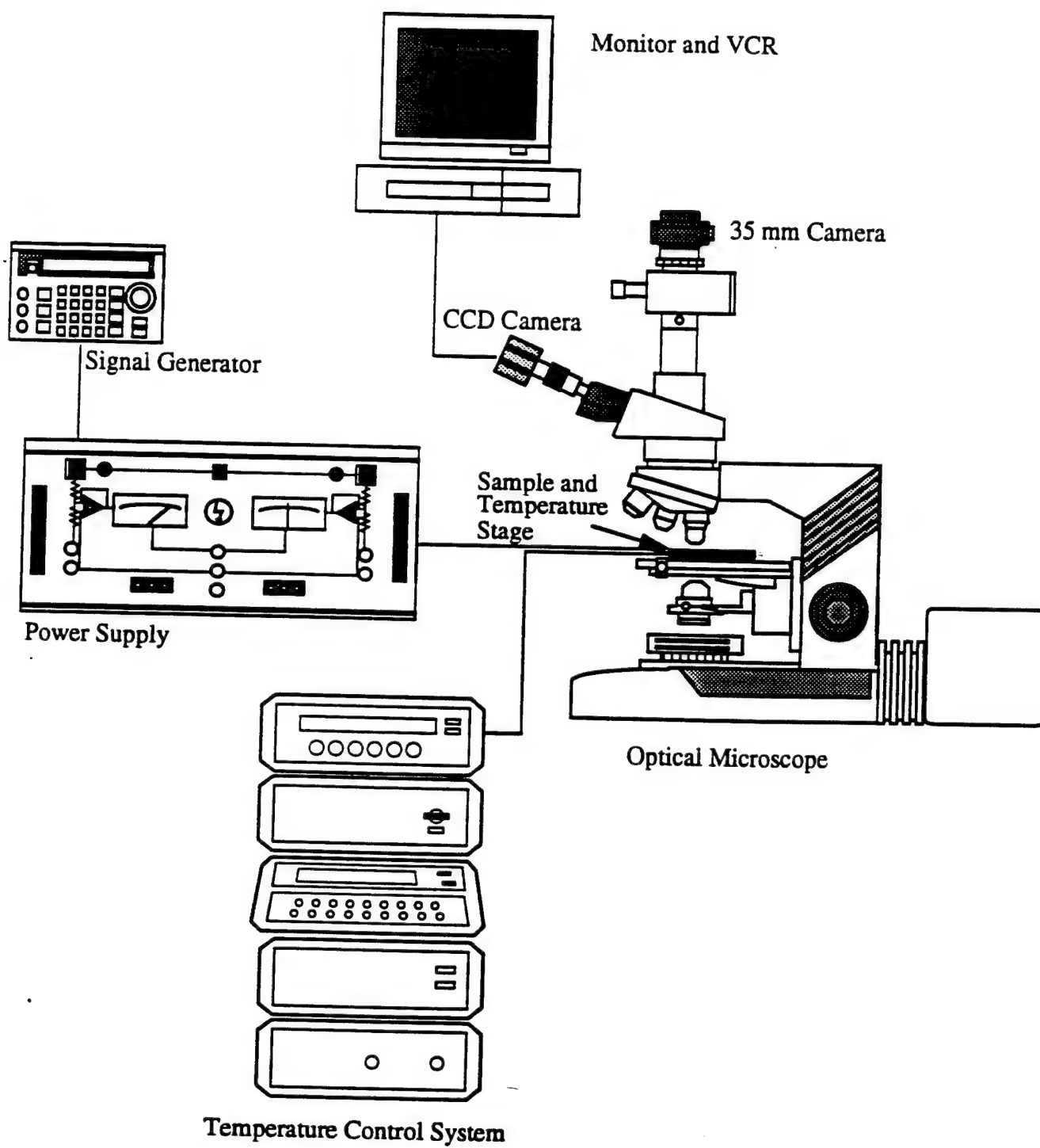
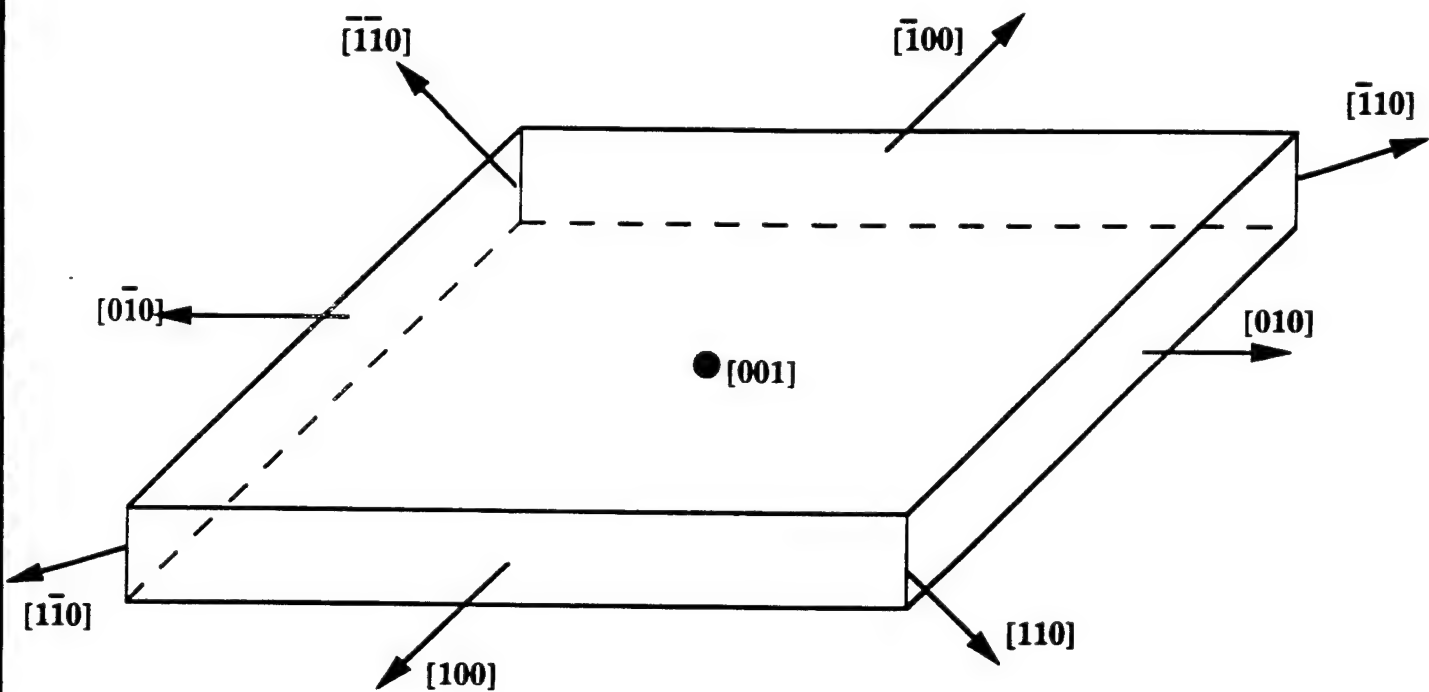


fig 1



292

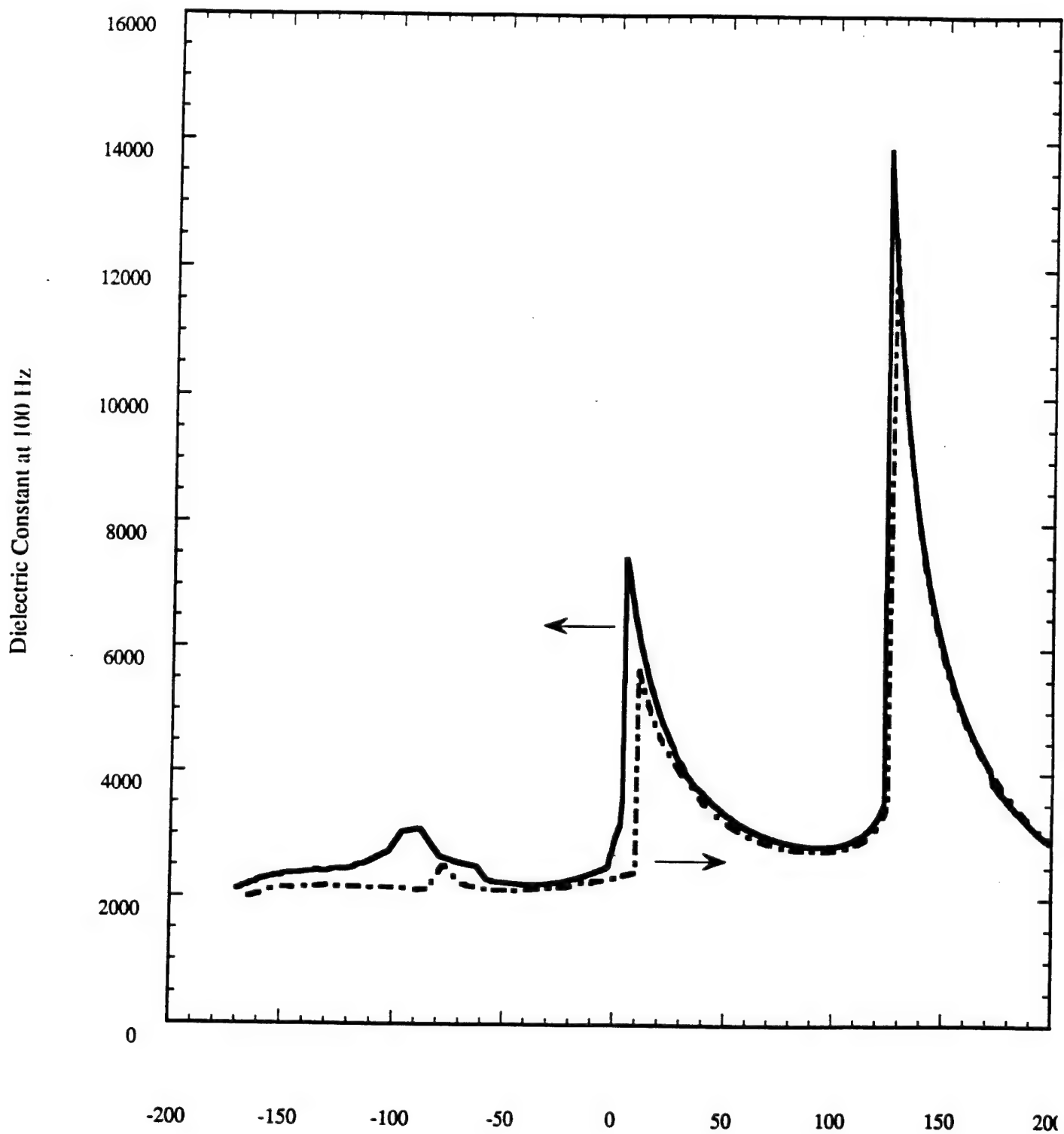
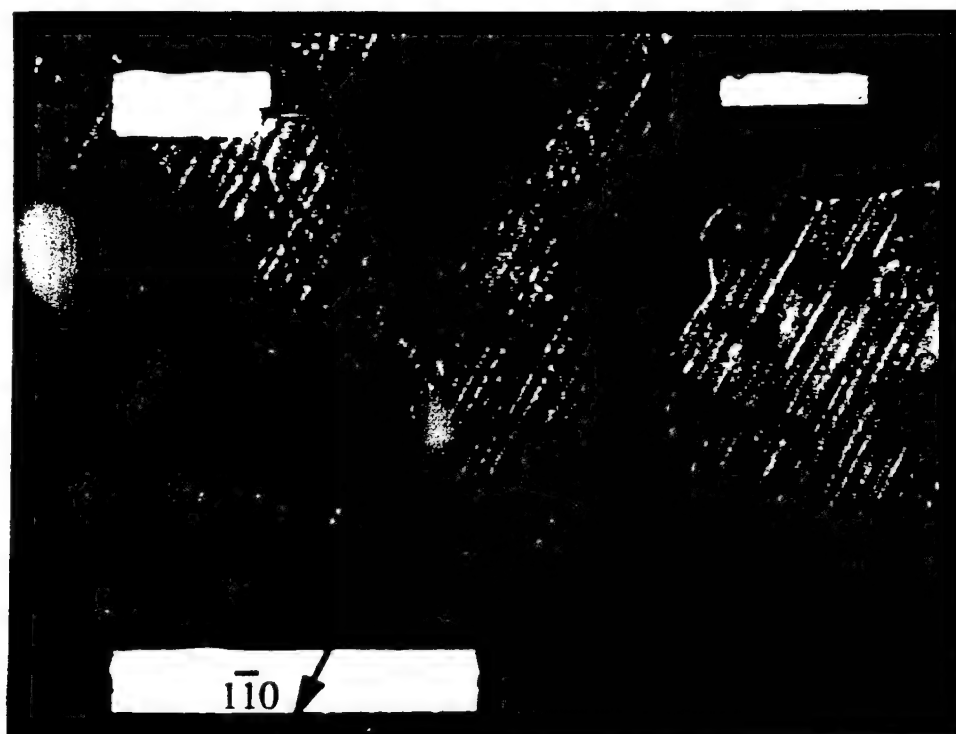
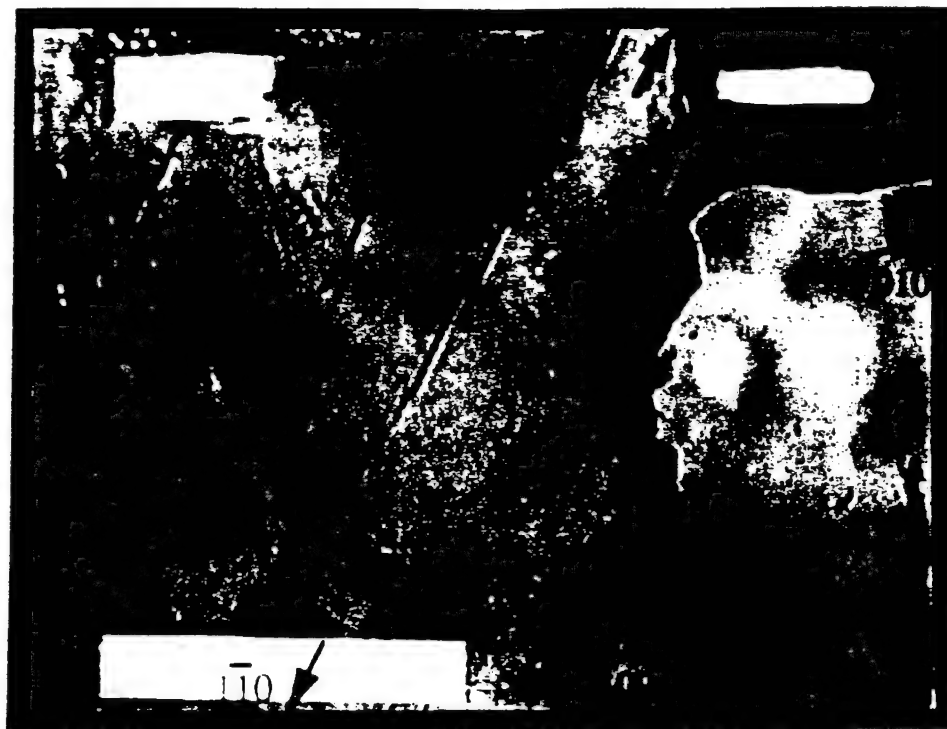
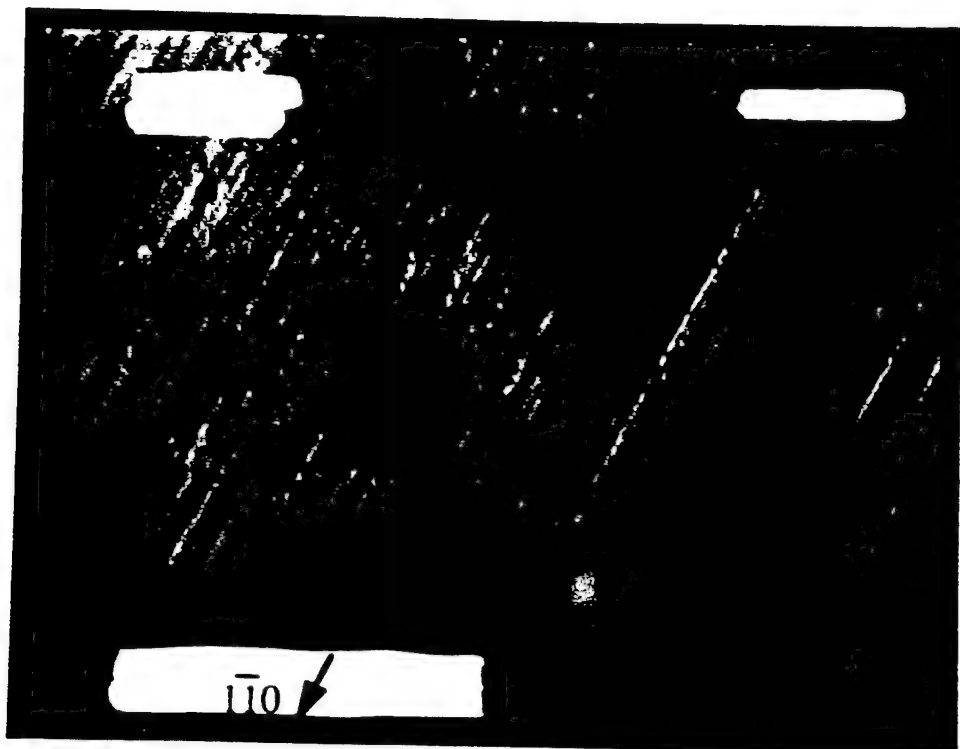
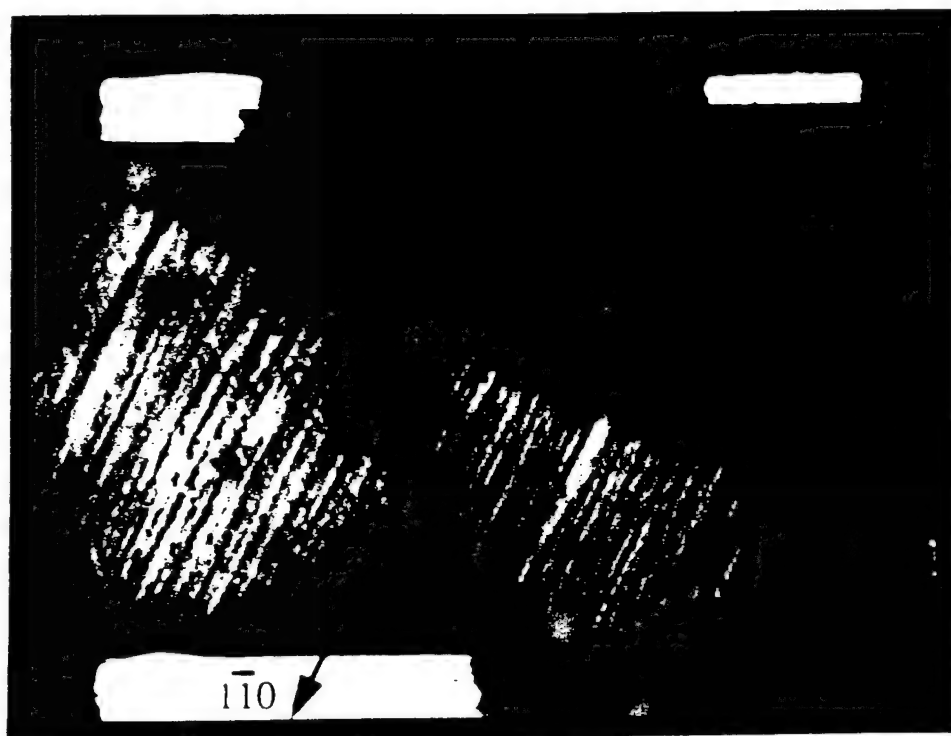


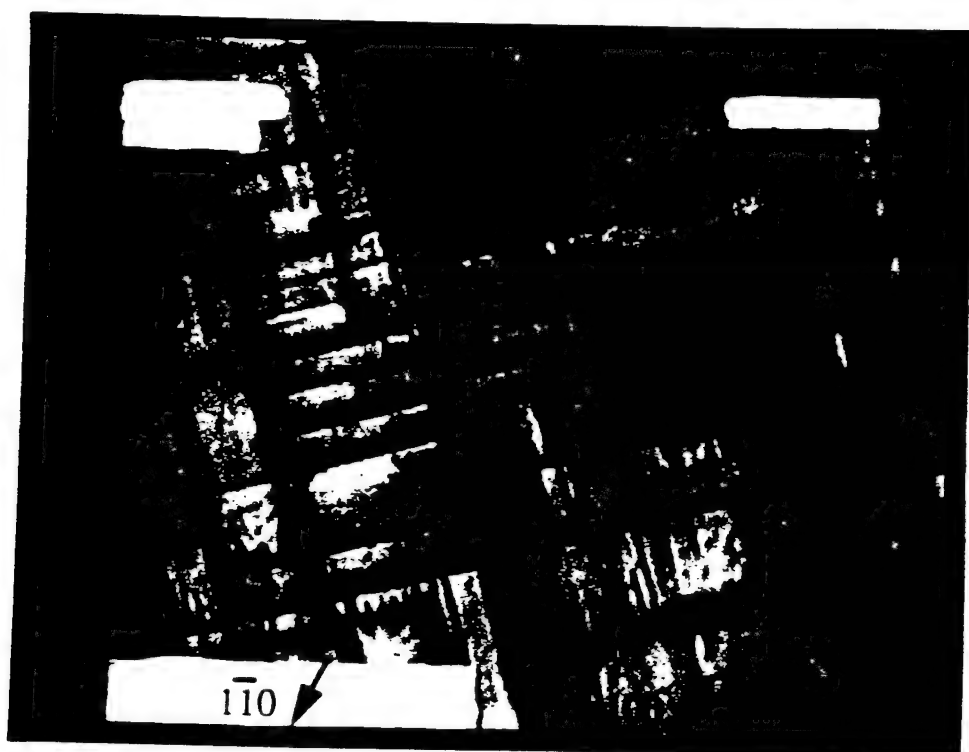
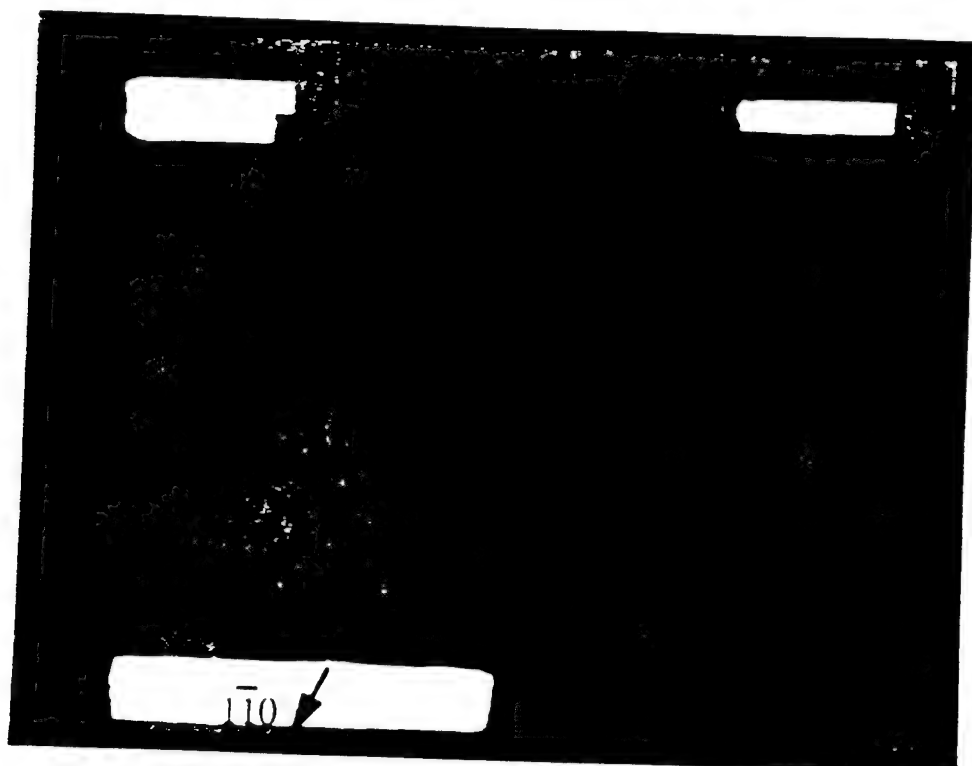
fig 3

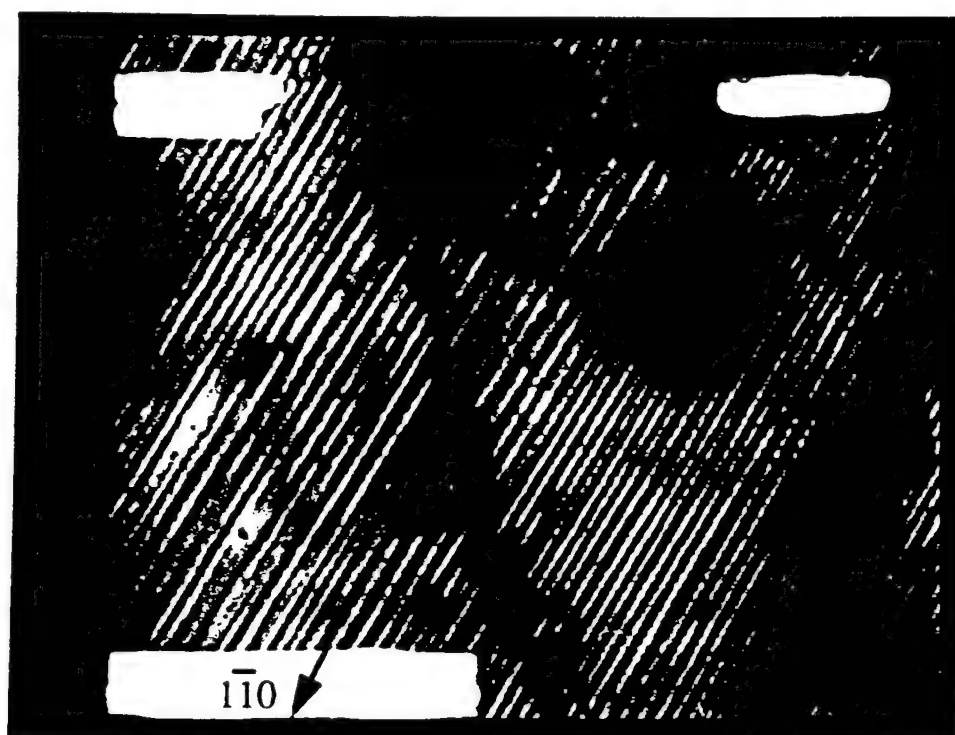


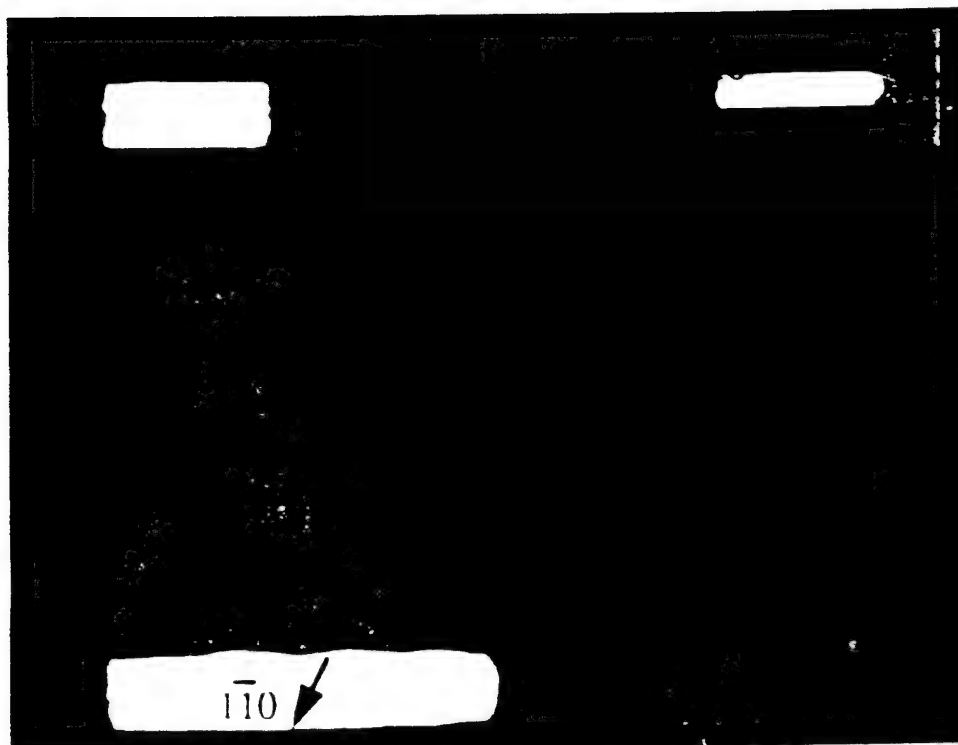












# **APPENDIX 16**

# Electric Properties and Domain Structures in Ba(Ti,Sn)O<sub>3</sub> Ceramics

Ki-Young Oh, Kenji Uchino and L. Eric Cross  
International Center for Actuators and Transducers, Materials Research Laboratory,  
The Pennsylvania University, University Park, PA 16802

**Abstract-** The Ba(Ti,Sn)O<sub>3</sub> ceramics are known as relaxor materials and they show very small hysteresis of field induced strains and field induced polarizations. Optical study was attempted to explain these dielectric properties. Domain structures and motions in Ba(Ti<sub>1-x</sub>Sn<sub>x</sub>)O<sub>3</sub> (x=0, 0.05, 0.1, 0.13) ceramics were observed under an electric field at various temperatures using a high resolution CCD microscope system. Electrical properties such as field induced strains, dielectric properties and field induced polarization characteristics were also measured. The Ba(Ti<sub>1-x</sub>Sn<sub>x</sub>)O<sub>3</sub> ceramics showed a significant difference in domain structures and motions with changing in the composition. The domain structure became tiny and complex with increasing x. Changes of domain structures due to the phase transitions were also observed with varying temperature. The domain reorientation was easily induced with rising and falling an electric field. The results of domain observations can explain the electrical properties well.

## 1. Introduction

Observation of domain structures and domain motion is very useful for understanding the physical properties of ferroelectric materials because domains are fundamentally associated with ferroelectricity. For the past few years we have been reporting on the dynamic domain motion in single crystals such as barium titanate and lead zinc niobate based compositions<sup>1,2</sup>.

This paper concerns the domains in Ba(Ti, Sn)O<sub>3</sub> ceramics. Ba(Ti, Sn)O<sub>3</sub> solid solutions are known as typical relaxor ferroelectric materials, and they exhibit dielectric and electromechanical characteristics associated with relaxor ferroelectrics such as very small hysteresis in the field induced polarization and strain<sup>3,4</sup>. These materials may provide a new category of useful actuator ceramics. Our investigation is focused on the domain motion in these materials as a means of analyzing the electrical characteristics.

## 2. Experimental Procedure

Samples of BaTiO<sub>3</sub>(BT), Ba(Ti<sub>0.95</sub>Sn<sub>0.05</sub>)O<sub>3</sub>(BTS-5), Ba(Ti<sub>0.9</sub>Sn<sub>0.1</sub>)O<sub>3</sub>(BTS-10) and Ba(Ti<sub>0.87</sub>Sn<sub>0.13</sub>)O<sub>3</sub>(BTS-13) were prepared by a conventional mixed oxide method. Mixed powders were calcined at 1100 °C for 2 hours. Disks 13 mm in diameter were pressed and sintered at 1350 °C for 10-50 hours in air. Sintered disks were sliced and polished 100 μm in thickness. One side of each sample was finished with 0.25 μm diamond paste and attached on to a glass plate using resin; then the other side was polished and finished with 0.25 μm diamond paste so that the sample thickness was less than 30 μm. Gold electrodes were sputtered on the sample surface with a gap of 800 μm, and then silver wires were attached to the electrode as shown in Figure 1.

Domain motions of samples were observed with a high-resolution (480,000 pixels) CCD microscope (Japan Hightech Co.) at various temperatures with an electric field applied parallel to the surface. Figure 2 shows the CCD microscope system. The reasons of using this CCD microscope are; 1) a SEM or TEM has higher magnification but it is difficult to apply electric field to sample and 2) an ordinary optical microscope can not record the quick domain motion.

The dielectric constant versus temperature curve was measured

in the temperature range from -100 to 200 °C using an automated Hewlett Packard system. Polarization versus electric field (P-E) curves were measured with a Sawyer-Tower circuit. Strain-field characteristics were measured using a linear differential transformer.

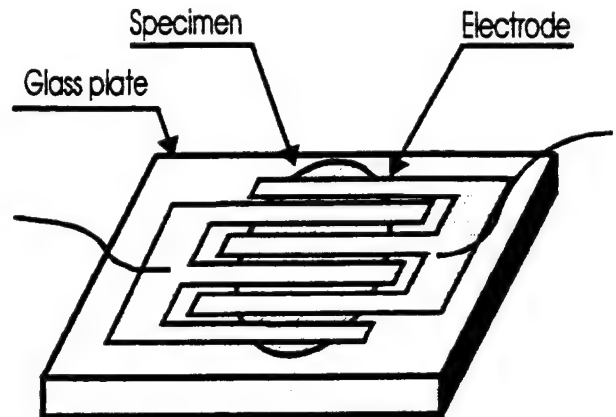


Fig. 1 Configuration of Sample.

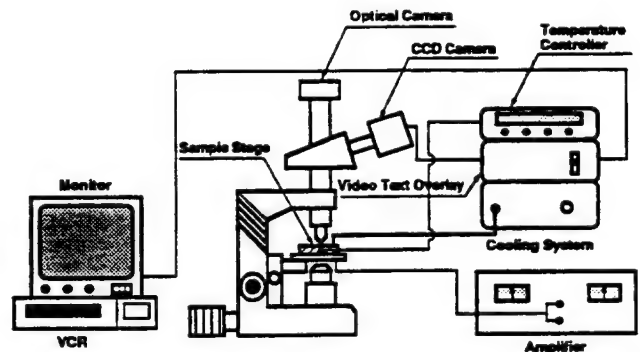


Fig. 2 Configuration of CCD Microscope system.

## 3. Results and Discussions

Figure 3 shows the temperature dependence of permittivity for BT, BTS-5, BTS-10 and BTS-13. The Curie temperature shifts to the lower side, and the shape of the peak becomes remarkably broader with increasing Sn content. The Curie temperatures of BT, BTS-5, BTS-10 and BTS-13 are 121.4, 85.7, 46.1 and 25.3 °C, respectively.

Electrical and electromechanical properties such as the P-E and field-induced strain characteristics were measured at room temperature, and the results are shown in Figs. 4 and 5. Compared with the BT sample, the BTS samples show smaller remanent polarization and less hysteresis. This is due to the Curie temperature shift to lower temperatures and the change of the phase transition characteristic from sharp to diffuse with increasing Sn content. The crystal structure of both BTS-10 and BTS-13 at room temperature was found to be pseudo-cubic. The field induced strain curves show a trend similar to the P-E curves (Fig. 5). With increasing Sn content, the hysteresis becomes smaller.

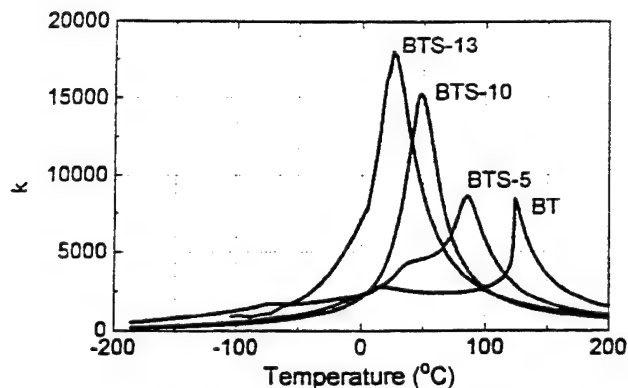


Fig. 3 Permittivity vs. temperature characteristics of BTS samples.

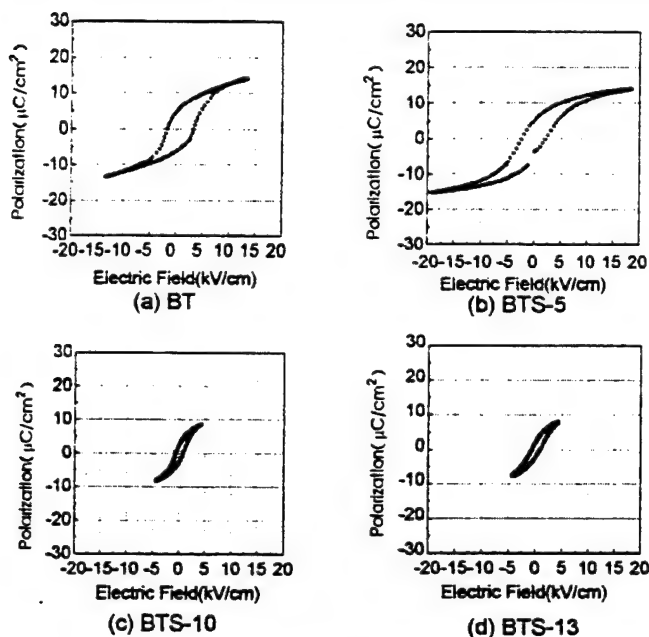


Fig. 4 Field induced polarization characteristics of BTS samples.

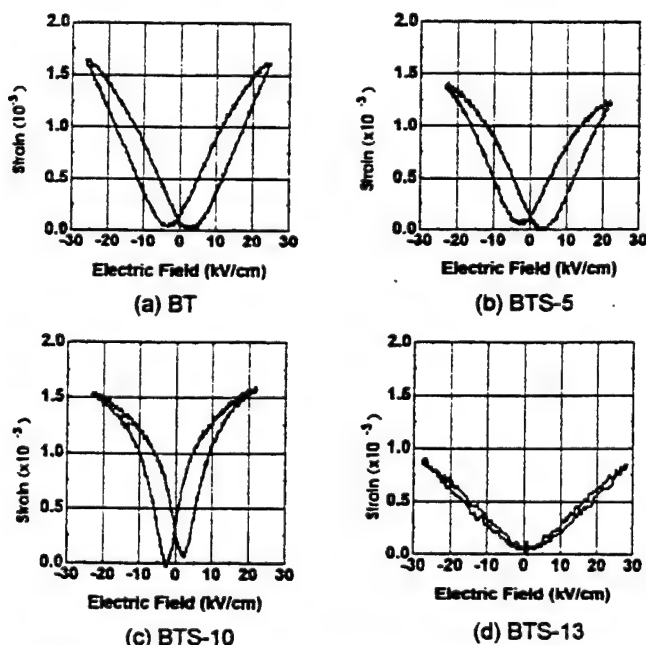


Fig. 5 Field induced strain characteristics of BTS samples.

Figure 6 shows the typical domain structures of BT, BTS-5, BTS-10 and BTS-13 samples at room temperature. The domain walls of BT are very clear straight lines, and the width of domain is rather thick. On the contrary, the domains of BTS-5 are tiny and less well defined. With increasing Sn content, these domain walls became more tiny and less well defined and finally, could not even be found in large grains (BTS-13). Variation of the domain structure with

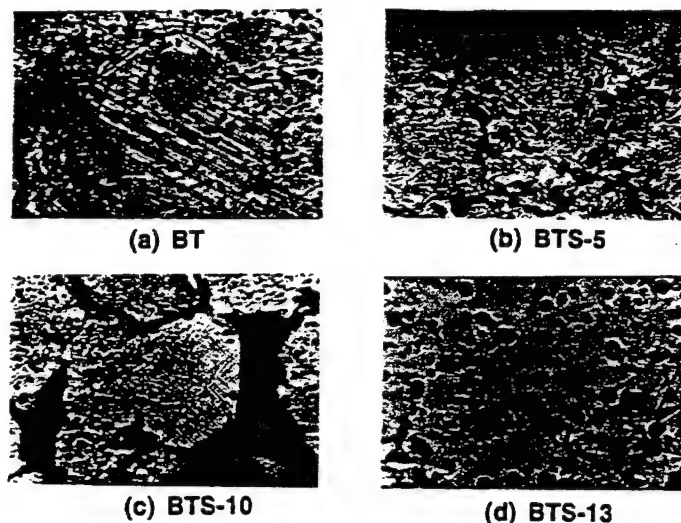


Fig. 6 Domain structures of BTS samples at room temperature.

temperature was also observed, and the results are shown in Figs. 7, and 8. With increasing temperature, the domain walls became unclear and disappeared completely above the Curie temperature. BTS-5 showed clear and simple domain structure at 55 °C because it shows tetragonal phase at this temperature. When the temperature

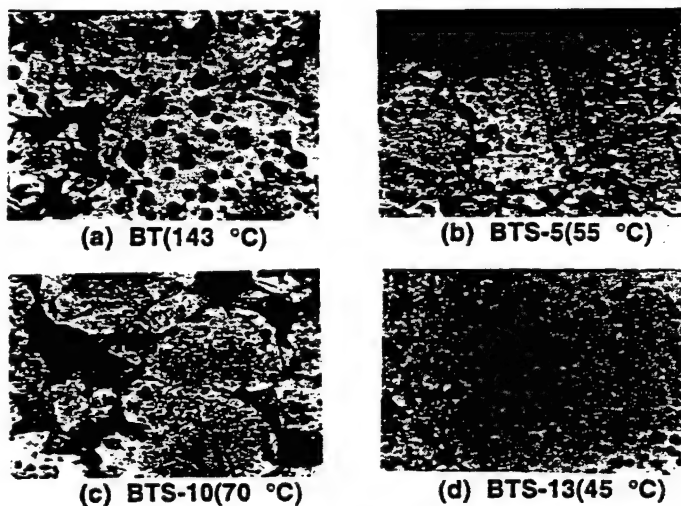


Fig. 7 Domain structures of BTS samples at high temperature.

was decreased, the BT and BTS samples showed different results. For the BT samples, the domain structures became difficult to define and some part of the large domains were divided into small spindle shape domains suddenly at 0 °C. We attribute this to the phase transition from tetragonal to orthorhombic at this temperature. The difference between the domain shapes in the tetragonal and orthorhombic phases is very clear, however the difference between domain shapes in the orthorhombic and rhombohedral phases is not significant. BTS-5 sample showed clear phase transitions from tetragonal to orthorhombic as shown in Fig.3 but it didn't show any sudden change of domain shape due to the phase transition like BT samples. The BTS-10, BTS-13 samples showed a gradual change



of domain structures with decreasing temperature. The domain walls became clear, in general, at a lower temperatures. It is noteworthy that the BTS-13, which does not show any domain walls at room temperature, shows obvious domain walls at low temperature (Fig.8). The domain size at this temperature is tiny and the domain walls are rather difficult to distinguish.

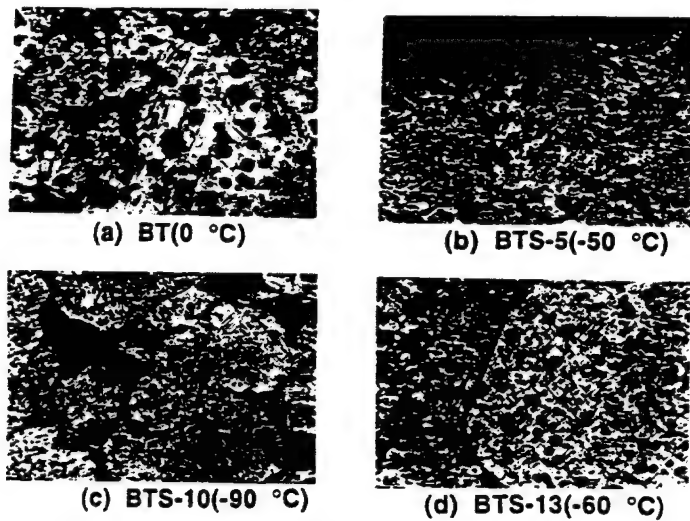


Fig. 8 Domain structures of BTS samples at low temperature.

Figures 9 and 10 show domain motion of the BT and BTS samples as a function of electric field at room temperature. A field of  $\pm 10$  kV/cm was applied to the samples. The BT samples showed  $90^\circ$  and  $180^\circ$  domain switching with application of the electric field. When  $+10$  kV/cm was applied to the BT sample, the domain walls were reoriented by  $90^\circ$  (Fig.9(b)). The reoriented domain walls remained even after removing the electric field (Fig.9(c)). The reoriented domain walls returned to their initial orientation when a small negative bias was applied (Fig.9(d)). The hysteresis of the domain motion is associated with the hysteresis in the P-E and field induced strain characteristics. BTS-5 sample also showed small hysteresis of domain motion. Poled domain shape is different from both of initial state and with field state. On the contrary, the BTS-

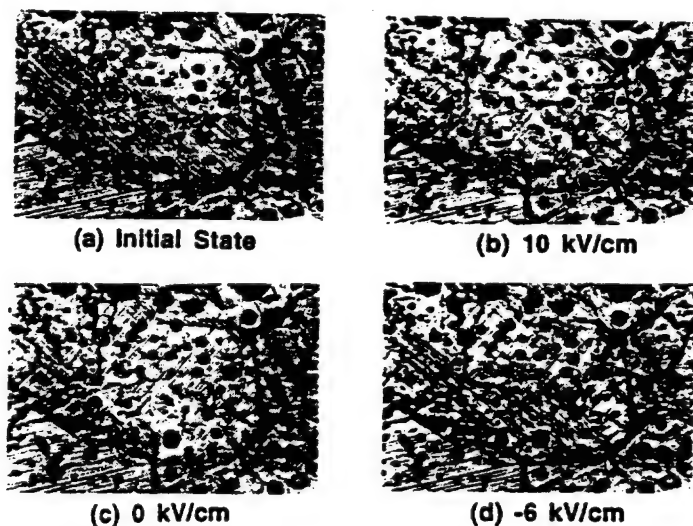


Fig. 9 Variation of domain structures of BT sample under an electric field.

10,13 samples did not show any hysteresis of domain motion as shown in Fig. 10,11. Applying an electric field up to  $+10$  kV/cm to the BTS-10 sample induces domain growth from tiny and complex domains to large and simple domains, and the domain structure returns to its initial state as the electric field is removed. In the case of the BTS-13 sample, the domain walls were observed only when an electric field of  $\pm 5$  kV/cm was applied, and these domain walls disappeared above  $\pm 5$  kV/cm as well as zero field. The domain dynamics of the BTS-13 sample is associated with the small hysteresis of P-E and field induced strain characteristics.

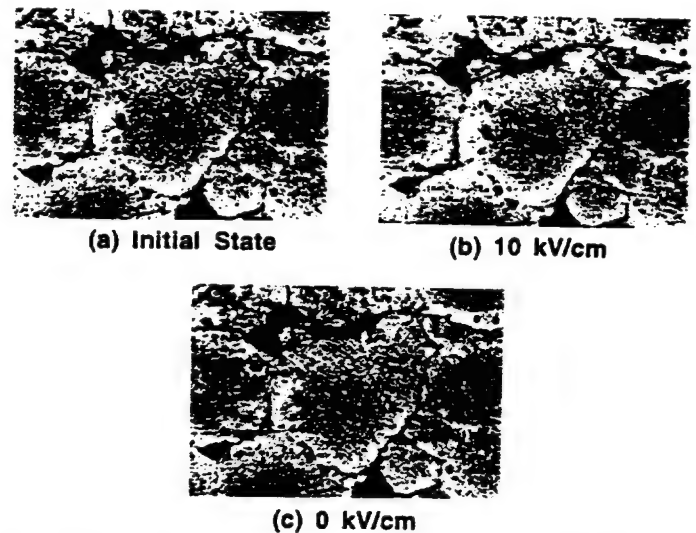


Fig.10 Variation of domain structures of BTS-10 sample under an electric field.

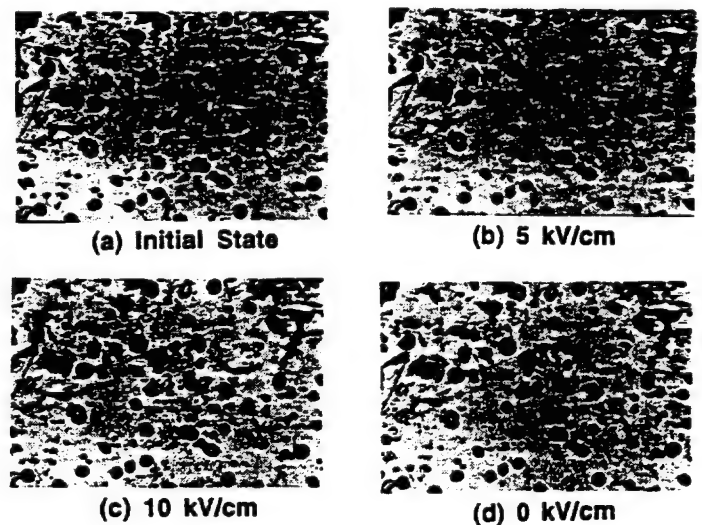


Fig.11 Variation of domain structures of BTS-13 sample under an electric field.

#### 4. Conclusions

Domain structures of  $\text{Ba}(\text{Sn},\text{Ti})\text{O}_3$  become drastically smaller, less well-defined and more complex with increasing Sn content. These micro domain configurations are rather similar to those of the relaxor ferroelectric  $\text{Pb}(\text{Zn}_{1/3}\text{Nb}_{2/3})\text{O}_3$ <sup>1)</sup>.

The domain motion of the  $\text{BaTiO}_3$  and  $\text{Ba}(\text{Ti}_{0.95}\text{Sn}_{0.05})\text{O}_3$  ceramic show hysteresis under an electric field, while the  $\text{Ba}(\text{Ti}_{0.9}\text{Sn}_{0.1})\text{O}_3$  and  $\text{Ba}(\text{Ti}_{0.87}\text{Sn}_{0.13})\text{O}_3$  samples do not exhibit hysteresis; this explains reasonably the superior nonhysteretic characteristic in the induced strain curve of  $\text{Ba}(\text{Ti},\text{Sn})\text{O}_3$ .

## REFERENCES

1. K. Kato, K. Suzuki and K. Uchino, "Observation of Domain Motion in Ferroelectric Single Crystals with a Diffuse Phase Transition" *J. Ceram. Soc. Jpn.*, **98** [5] 840-45 (1990)
2. K. Uchino, "Relaxor Ferroelectrics" *J. Ceram. Soc. Jpn.*, **99** [10] 829-35(1991)
3. J. Von Cierninski, H. Th. Langhammer, and H.P. abicht, "Peculiar Electromechanical Properties of Some Ba(Ti,Sn)O<sub>3</sub> Ceramics" *Phys. Stat. Sol. (a)* **120**, 285-93 (1990)
4. J. Von Cierninski and H. Beige, "High-signal electrostriction in ferroelectric materials" *J. Phys. D: Appl. Phys.* **24** 1182-86 (1991)

# **APPENDIX 17**

## ELASTIC AND ELECTRIC CONSTRAINTS IN THE FORMATION OF FERROELECTRIC DOMAINS

WENWU CAO

*Intercollege Materials Research Laboratory, Pennsylvania State University,  
University Park, PA 16802*

*(Received September 6, 1994)*

Domain formation in ferroelectric system is a consequence of energy competition between different energy sources, including domain wall energy and the dipole-dipole interaction energy which are internal, and the electrostatic energy from compensating charges and the elastic interaction energy from boundary constraints which are external. The external contributions give the domain patterns in ferroelectrics some distinct features which are different from those in ferromagnetics and ferroelastics.

*Keywords: Ferroelectric, ferroelastic, domains, domain walls, elastic constants.*

### INTRODUCTION

Domain formation is a common feature of ferroic systems, which fascinates scientists not only because its physical complexity, but also because the role of domains in determining many physical properties of ferroic systems. In simple physical arguments, the formation of domains is the manifestation of the coexistence of multi-variants in the ferroic phase. There are two distinct groups, i.e., coherent and incoherent domains. The latter is the result of multi-nucleation centers for the ferroic transition associated with structural defects, such as cracks, dislocations, surfaces, etc., domains of this kind can not be switched easily from one to the other since they have strong ties with defects. The formation of coherent domain patterns is controlled by the intrinsic properties of the system and the boundary conditions, it can be described from the view point of energy balance between different sources.

The simplest and the most thoroughly studied ferroic system is ferromagnetic system in which the domain formation is dominated by two energy sources, i.e., the domain wall energy and the demagnetization energy.<sup>1,2</sup> Since there are no free magnetic monopoles, the magnetization in the domain structures must form a closed loop. In a ferroelastic case, the domain formation is determined by the balance of domain wall energy and the elastic interaction energy with the surrounding medium.<sup>3</sup> Domain formation in ferroelastics is more involved than in ferromagnetics because the inclusion of the surrounding medium in the energy minimization process and the tensorial nature of the elastic interactions. Ferroelectric system is the most complicated among all three types of ferroic systems, which combines the characteristics of both ferromagnetic and ferroelastic systems, in addition, there is a new complication of free charge carriers which accumulate at the interfaces and the surfaces of a finite system to compensate the internal electric field. In order

to understand the influence of electric boundary conditions and the elastic constraints on the formation of domain patterns, we need to analyze each energy contributions in more detail.

## DOMAIN WALL ENERGY

Domain wall is the coherent transition region in a twin structure. In the spirit of Landau-Ginzburg theory, the domain wall can be described by a continuum model consisting both nonlinear and nonlocal contributions.<sup>4,5</sup> The mathematic formulation of the continuum theory allows solitary wave solutions which describe the twin and twin band structures in ferroelectrics. From these solutions one can calculate all the physical properties of domains and domain walls, such as the width of domains, the thickness of domain walls and the energy associated with domain walls. It can be easily verified from the solution of continuum theory that the energy associated with a domain wall is positive definite and the interaction between walls is repulsive.<sup>5</sup> Because of the positive energy associated with these domain walls, single domain state would be the most desirable configuration when the depolarization field is compensated.

## ELECTROSTATIC ENERGY AND 180° DOMAINS

There are two sources for the electrostatic energy. One is the interaction energy among the dipoles generated in each unit cell, which tends to align the dipoles in the forwarding direction (along the poling direction) but flip over all neighboring dipoles in the transverse direction (perpendicular to the poling direction). When this dipole-dipole interaction energy is used to balance the domain wall energy, the result will be a regularly spaced 180° domains with planar domain walls.<sup>6,7</sup> The other electrostatic energy contribution is from the free charge accumulations, mostly on the surfaces and interfaces as a mean to compensate nonvanishing electric fields. Because of these compensating charges, ferroelectric domain patterns do not have to arrange the polarization vector in the domains to form a closed loop like in ferromagnetics. These two electrostatic energy contributions plus the domain wall energy contribution make the formation of 180° domains very complicated. In certain cases, the effects of compensating charges may be neglected due to the relatively lone relaxation time, especially when the charges are captured from external sources, but one must include the contributions from the internal charge carriers in calculating the stable domain patterns in ferroelectrics.<sup>8,9</sup> When the compensating charges are neglected, the 180° domain pattern in ferroelectrics is similar to that of the ferromagnetic case, i.e., regularly spaced domains with planar domain walls. However, with the compensating charge effects, the 180° domains will not be regularly spaced and may not even be planar depending on the charge carrier concentration and the conductivity of the system. Figure 1(a) is for the case of regularly spaced 180° domain pattern where no free charges are present. Figure 1(b) is the irregular 180° domain pattern for which the depolarization field is compensated in each of the domains and the free charge carriers trapped on the

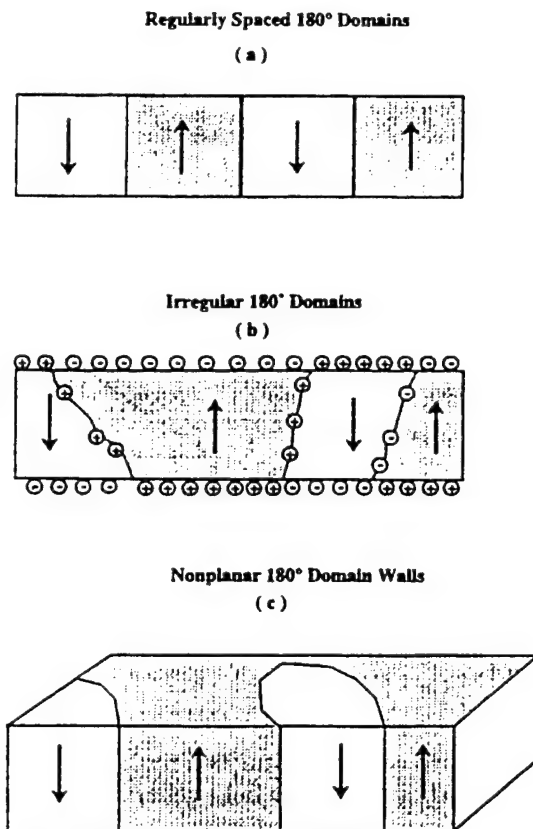


FIGURE 1 (a) Regularly spaced 180° ferroelectric domains without free charges, (b) irregularly spaced 180° domain pattern caused by the charge compensation on the surface and interfaces, and (c) nonplanar domain walls.

domain walls cause the wall to bend, this pattern may eventually settle down to the situation illustrated in Figure 1(c) which shows the nonplanar 180° domain walls commonly observed in ferroelectrics.

#### ELASTIC ENERGY AND NON-180° DOMAINS

The formation of non-180° domains, such as 90° domains in tetragonal ferroelectrics, is controlled by the elastic boundary conditions. The elastic interaction energy between the system and the surrounding medium depends on the geometry of the system and the size of the medium. There are 1-D, 2-D and 3-D cases in terms of elastic energy calculation. Figure 2(a) is the 1-D case in which the vertical dimension of the medium along the domain wall is relatively small and the horizontal dimension and the dimension perpendicular to the drawing plane are very large, Figure 2(b) is the 2-D case in which the dimension of the system is much larger perpendicular to the drawing plane than that in the plane, and Figure 2(c) is the 3-D case in which the system is simply merged in a large three dimensional medium.

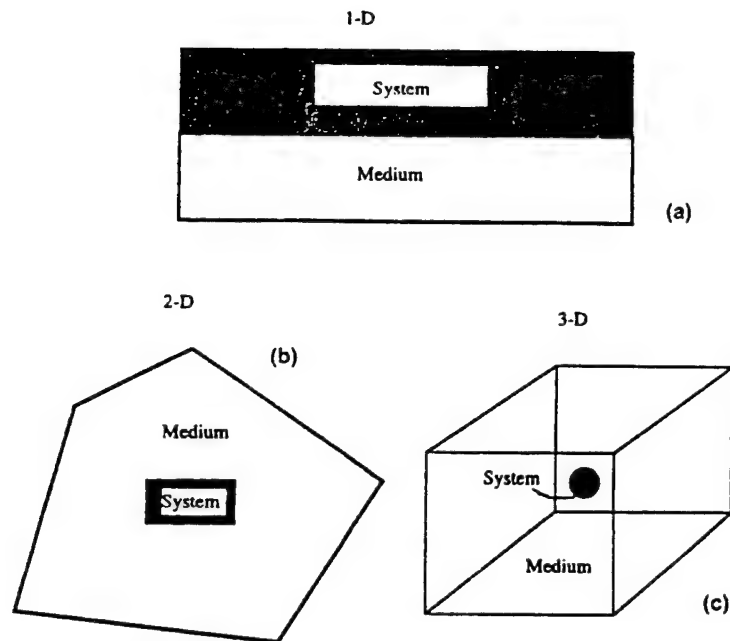


FIGURE 2 The definition of 1-D, 2-D and 3-D stress situation used in the analysis for a ferroelectric in an elastic medium.

In thin film case, the ferroelectrics is attached to the substrate only on one side, if we look at the cross section the stress field generated at the interface is either 1-D or 2-D, while the domains inside ceramic is an example of 3-D case. As a consequence of the stress field difference, domain size can be quite different for thin film with substrate, thin samples for TEM observations and a grain inside a large ceramic. Previous analyses<sup>3,7</sup> on ferroelastic domains all give the same square-root relationship between the domain size  $l_d$ , and the grain size  $L_g$ , i.e.,

$$l_d \propto \sqrt{L_g} \quad (1)$$

which is the same as for ferromagnetic domains. However, no concrete experimental data are available to verify this relationship up to date.

Of course, all theories were based on certain assumptions which may not always be applicable. There are circumstances when this relation does not hold, for example, let us take a simple 1-D case as shown in Figure 3 for a cubic-tetragonal phase transition. Figure 3(a) is a section of a ferroelectric system which will form one of the  $90^\circ$  domains below the transition temperature with the polarization pointing to the  $[010]$  direction, the system is free on one side and attached to an elastic medium on the other side, the medium is fixed at its bottom to simplify our calculation. Assuming we can make an imaginary separation of the system and the medium, the system will transform freely to the tetragonal phase making a shear deformation in  $[\bar{1} 1 0]$  as illustrated at the top portion of Figure 3(b), if we now apply a virtual stress in the vertical direction which is a linear function of the horizontal axis so that the system and the medium will have the same slope along their interface and rejoin the two together afterwards, the whole structure will

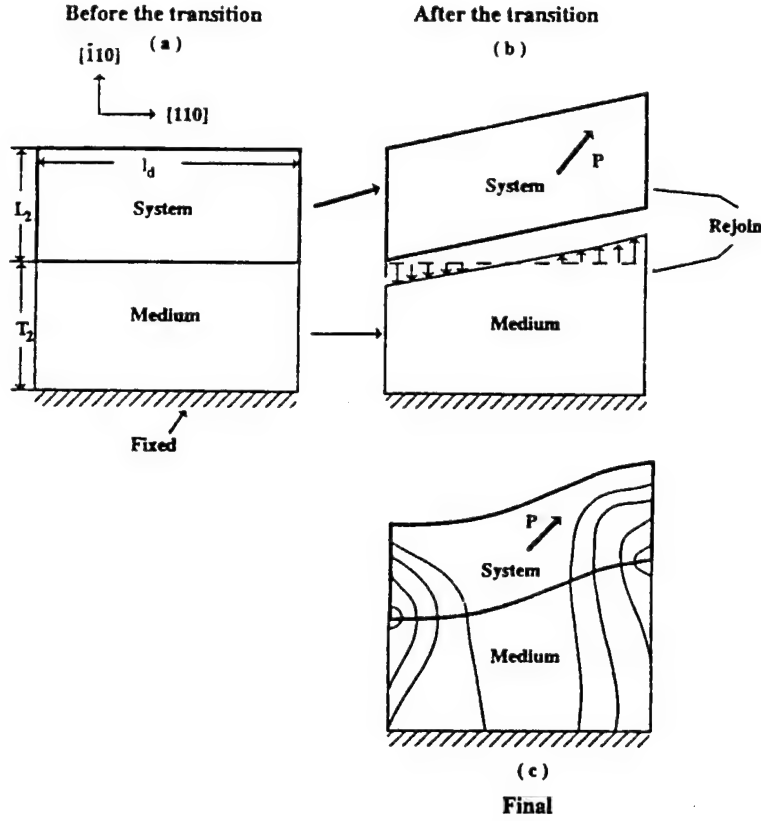


FIGURE 3 A section of a ferroelectric attached to a medium whose bottom is fixed. (a) before the phase transition, (b) after the cubic-tetragonal transition and (c) the final stable configuration and the stress contour.

readjust to the new equilibrium position as shown in Figure 3(c), where the surface of the system will be bent and the stress field is illustrated by the contour curves with the high stress concentrated near the domain wall regions. When the elastic constant of the medium is the same as the ferroelectric system, we can approximate the elastic energy of Figure 3(c) by taking one-half of the energy calculated in Figure 3(b) using the equal partition principle since the kinetic energy will be damped out during the relaxation process from Figure 3(b) to Figure 3(c). When the elastic constant of the medium is different from the system, the elastic energy of Figure 3(c) will be proportional to the elastic energy of Figure 3(b) but not equal to one-half. This elastic interaction energy between the medium and the system gives an additional effective contribution to the system, which if used to balance the domain wall energy will lead to the following equilibrium domain size  $l_d$ ,

$$l_d = \sqrt[3]{\frac{24\sigma_w T_2 L_2}{C\alpha^2}} \quad (2)$$

where the quantity  $\sigma_w$  is area density of the domain wall energy,  $C$  is the effective normal elastic constant of the medium in  $[\bar{1}10]$  direction and  $\alpha$  is the deformation



angle caused by the shear in the  $[\bar{1} 1 0]$  direction. Considering  $L_2$  to be the grain size, the relationship between the domain size and the grain size will be cubic-root instead of square-root as Equation (1).

The inclusion of the medium dimension  $T_2$  in the expression is a consequence of the global energy minimization and the fact that the 1-D like stress will extend into the whole medium. In most of practical cases, the medium is much larger compared to the system, therefore, the stress field becomes 2-D or 3-D, which will decay in the inverse powers of distance from the system-medium interface. In the 2- and 3-D cases the medium dimension  $T_2$  is integrated out to become a characteristic length for the stress field, but the cubic relation Equation (2) still hold. Compared with the experimental data of Arlt<sup>10</sup> for  $\text{BaTiO}_3$ , the cubical relation fit much better than the quadratic relation for the larger grain tetragonal phase.

## SUMMARY AND CONCLUSIONS

The formation of coherent ferroelectric domains is the result of global energy minimization which not only involves the ferroelectric but also the free charges and the elastic medium that is directly in contact with the ferroelectric. The competition between three energy sources determines the formation of  $180^\circ$  domains, the domain wall energy, the dipole-dipole interaction energy and the free charges at the surfaces and interfaces. The presence of free charges causes the formation of irregular  $180^\circ$  domain patterns, and the walls may even be curved in certain cases. Since the free charges can flow through the system, the  $180^\circ$  domains can not have "memory" when the temperature is cycled through the ferroelectric phase transition.

The formation of coherent non- $180^\circ$  domains is mainly a consequence of the elastic interaction of the system with the surrounding medium. The stress field produced at the interface could have 1-D, 2-D or 3-D nature for different geometry as shown in Figure 2. For the 2-D and 3-D cases, the interface stress will decay in the inverse power law so that the domain size will be independent of the medium size for a relative large medium. But for system with 1-D like stress, the dimension of the medium will also influence the domain size. A simple derivation shows that the domain size-grain size relationship for the ferroelastic walls is cubical instead of quadratic for the 1-D model. Compared with existing experimental data on  $\text{BaTiO}_3$ , the cubic-root relation fits better than the square-root relation systems with grain size larger than  $10 \mu\text{m}$ .

## ACKNOWLEDGEMENTS

The author wishes to thank Drs. L. E. Cross, C. R. Randall, R. E. Newnham and J. R. Banavar for beneficiary discussions. This research was sponsored by the Office of Naval Research and the National Science Foundation.

## REFERENCES

1. L. Landau and F. Lifshits, *Sov. Phys.*, **8**, 153 (1935).
2. J. Fousek and M. Safrankova, *Japan J. Appl. Phys.*, **4**, 406 (1965).

3. B. Horovitz, G. R. Barsch and J. A. Krumhansl, *Phys. Rev. B*, **43**, 1021 (1991).
4. V. A. Zhirnov, *Sov. Phys. JETP*, **35**, 822 (1959).
5. W. Cao and L. E. Cross, *Phys. Rev. B*, **44**, 5 (1991).
6. C. Kittel, *Phys. Rev.*, **70**, 965 (1946).
7. G. Arlt, *J. Mat. Sci.*, **25**, 2655 (1990).
8. B. V. Selyuk, *Soviet Phys. Crys.*, **16**, 292 (1971).
9. M. E. Lines and A. M. Glass, *Principles and Applications of Ferroelectrics and Related Materials* (Oxford University Press, Oxford, 1977).
10. G. Arlt, *Ferroelectrics*, **104**, 217 (1990).

# **APPENDIX 18**

# **The Grain Size and Domain Size Relations in Bulk Ceramic Ferroelectric Materials**

Wenwu Cao and Clive. A. Randall

Materials Research Laboratory, Pennsylvania State University

University Park, PA 16802, U.S.A

**Keywords:** A. ceramics, A. interfaces, C. electron microscopy,  
D. ferroelectricity, D. microstructure

## **Abstract**

A study of the ferroelastic domain size variations with grain sizes in  $\text{Pb}(\text{Zr,Ti})\text{O}_3$  [PZT] ferroelectric ceramic has been conducted. Experimental results determined by a transmission electron microscopy (TEM) study on hard and soft PZT ceramics indicate that it is possible to observe a bulk metastable domain configuration in a thinned foil. Theoretical analysis and direct transmission electron microscopy observations demonstrate that the domain structures are strongly dependent on the elastic boundary conditions and crystallite sizes. The traditional parabolic domain size and grain size relation is not a comprehensive description of the distribution of domains in ceramics, especially for small grain size systems. Statistical analysis of the domain size distributions in PZT reveals that the parabolic dependence is only good for a limited size range of  $1\mu\text{m} - 10\mu\text{m}$ . For grain size  $> 10\mu\text{m}$ , the exponent tends toward  $1/3$  while for grain size  $< 1\mu\text{m}$ , the exponent is larger than  $1/2$ . Additional insights are gained from the analysis of poled ceramics which reveal direct evidence for trans-granular domain switching mechanisms.

## Introduction

Domain structures are generated during a structural phase transition to recover the lost symmetry operations[1,2]. In ferroic materials, these domain structures can be switched by external (elastic, electric, or magnetic) fields. Hence the domain population distribution is strongly affected by these fields.

Stable domain configurations in ferroic materials are the result of an energy balance. In the case of a ferroelectric system stable domain configurations reflect the balance of anisotropy energy, domain wall energy, electric and elastic energies. Previous theoretical investigations considered the energy balance of elastic interactions and that of the domain walls, which leads to a parabolic scaling ( $m=1/2$ ) of the grain-domain size relation [3-8],

$$\text{Domain Size} \propto (\text{Grain Size})^m. \quad (1)$$

Most previous domain size studies have focused on ceramic BaTiO<sub>3</sub>. One of the major reasons for studying this system is the strong macroscopic dielectric constant enhancement observed in the tetragonal ferroelectric phase of 1.0  $\mu\text{m}$  grain materials compared to coarse grain ceramics and single crystals. The change of the dielectric constant with grain size has been accounted for in terms of the different stresses created under the spontaneous deformation at the cubic-tetragonal phase transition [9].

Arlt re-examined the domain size distributions in BaTiO<sub>3</sub> ceramic and departure of the domain size grain size relation from the parabolic relation for grain size below 1  $\mu\text{m}$  and above 10  $\mu\text{m}$  [7]. Domain density is higher than the value predicted using the parabolic relation for submicron grains as shown in Figure 1. For grain sizes larger than 10  $\mu\text{m}$ , the exponent in Eq. (1),  $m$ , is found to be close to 1/3, and the slope becomes steeper as the grain size decreases. When the whole range of domain and grain sizes are considered, the fitting to the  $m=1/2$  is very poor as shown in Fig. 1. The current work is in part triggered by this observation.

In practice, the size effect of domain structures is of importance to the future application trends in ferroelectric based materials. In the last few years there have been

rapid advances in the ability to fabricate thin and thick films for applications such as memories, micromotors, thermal imaging, multilayer capacitors, and actuators[10,11] The miniaturization of ferroelectric based electroceramic components is accompanied by the necessity of the reduction of grain sizes. Consequently, the domain sizes, domain configurations, and domain wall mobility will all be changed.

Owing to the large contribution of the elastodielectric properties from the extrinsic mechanisms, i.e., domain walls motion, it is imperative to advance the understanding of domain size effects in the submicron grain size ceramics[12,13]. In this paper, we present some experimental studies on the domain size distributions in poled and unpoled PZT ceramics. In addition, thermally cycling effects on the domain populations in the thin foil samples used in the TEM experiments were also examined. Theoretical analysis shows that the exponent,  $m$ , in the domain size-grain size relation can vary substantially due to the change of boundary conditions and also dimensions .

## **Experimental**

### **Ceramic processing**

Morphotropic phase boundary composition PZT has been investigated in sintered ceramics with a grain size variation from 0.2 to 14  $\mu\text{m}$ . Starting powder size variations were obtained from solid state reactions using conventional and reactive calcination techniques[14,15]. Grain size variations were obtained by controlling densification and grain growth during the sintering process. The submicron grain size ceramics were fabricated using hot pressing techniques; namely, hot uniaxial pressure (HUP) and hot isostatic pressure (HIP). The larger grain size ceramics ( $> 1 \mu\text{m}$ ) were sintered using conventional methods by varying temperature and time in closed crucibles and controlling the lead atmosphere with  $\text{PbZrO}_3$  sources.

Two systems with the morphotropic composition were investigated in this study: one is undoped  $\text{Pb}(\text{Zr}_{.52}\text{Ti}_{.48})\text{O}_3$ , and the other is Nb-doped PZT based on compositional

formula of  $\text{Pb}_{0.988}(\text{Zr}_{0.52}\text{Ti}_{0.48})_{0.976}\text{Nb}_{0.024}\text{O}_3$  [17]. The undoped PZT is naturally a hard piezoelectric material owing to the superoxidation processes creating an excess of acceptor lead vacancies over oxygen vacancies. The Nb-donor doping is commonly used in commercial soft PZT for piezoelectric applications and is therefore regarded as a model system for this study.

### Transmission Electron Microscopy

The domain size distributions and structures were investigated using analytical transmission electron microscopy (TEM); Phillips-420 STEM operated at 120 kV. TEM is most suited for microstructural investigations in the nanometer to micrometer size regime. Ferroelectric domains can be directly imaged using diffraction contrast imaging techniques [18,19]. The observations were made on dense (>95% theoretical density) ceramic samples which were cut and polished to a thickness of 70  $\mu\text{m}$ . Samples were epoxied to 3 mm copper grids before ion-beam thinning at 3 kV, with a 12° glancing angle until electron transparent. The poled samples were prepared after exposure to a poling field of 40 kV/cm in a heated oil bath at 120°C for 20 minutes. Samples were prepared with the poling direction in the plane of the thin foil. A Gatan single tilt hot stage was used to heat thinned samples through the transition temperature to re-equilibrate the domain configurations in the foils used for TEM studies.

### **Theoretical**

Our investigation is primarily concerned with the non-180° domains in PZT ceramics. At the morphotropic phase boundary (MPB) of PZT there exist the possibility of the coexistence of two ferroelectric phases, i.e., tetragonal and rhombohedral [20]. There are 14 possible polarization directions (6 for tetragonal phase and 8 for rhombohedral phase), and domain wall orientations are in {100} and {110} pseudocubic lattice planes. The size of the domains as bounded by the domain walls is influenced by the energy

considerations listed above. In the case of the non-180° ferroelectric domains the dominant contributions are the wall energy,  $E_w$  and the elastic energy,  $E_{el}$ .

The domain wall energy is a consequence of strong non-local coupling. The energy density contribution from the domain walls can be calculated with the Landau-Ginzburg expansion [20,21]. The effective energy density of the domain walls can be expressed as :

$$E_w = \frac{\sigma_w}{D} \quad (2)$$

where  $\sigma_w$  is the surface energy density of a domain wall, and  $D$  is the domain size [3-6].

Both ferroelastic and ferroelectric transitions are accompanied by large strain changes. In a confined system, this strain produced at the phase transition would entail a large elastic energy if the ferroic phase were to form a single domain. Therefore, a multidomain state is produced to minimize the elastic interaction energy between the system and the surrounding medium. The calculation of the elastic energy density depends on the nature of the boundary conditions and the dimensionality of the system. As mentioned above there have been a number of approaches to evaluate the size of ferroelastic and coelastic domains, all suggesting a parabolic relation [3-8]. Most of the previous calculations have utilized the concept of invariant plane strain [3] and assume vanishing far field elastic strain produced at the system-medium interface. However, in a finite system and a finite medium the calculation of interaction energy depend strongly on the geometry and boundary conditions. In what follows we conduct an analysis in a simple system to show this situation.

Figure 2 shows a finite system with dimensions of  $L_1 \times L_2 \times L_3$  joined with an elastic medium having dimensions of  $L_1 \times T_2 \times L_3$ . Where,  $L_1, L_3 \gg L_2$  and  $T_2$ , similar to the practical case of a thin film on a substrate. Since the dimension of the medium is small, we should use a different estimate for the elastic interaction energy.

Considering as a model example of a cubic to tetragonal phase transition, 90° domains will form in accordance with the elastic boundary constraints. If  $x$ ,  $y$  and  $z$  coordinates, as shown in Figure 2(a), are chosen to correspond to the original cubic



symmetry directions of  $[110]$ ,  $[\bar{1}10]$ , and  $[001]$ , the  $90^\circ$  domain walls will be parallel to the y-z plane. For simplicity consider the top surface of the sample to be free, whereas the bottom of the medium is rigidly fixed. We now select a single domain section along with the attached medium as shown in Figure 2(b). The approach developed by Eshelby is used to calculate the elastic energy generated at the phase transition [22]. Assuming the system and the medium are separated so that the system is free to transform, a shear deformation will occur in the system as shown in Fig. 2 (b). We then press the medium to match the slope of the transformed system so that an effective energy density of the following form will be generated [22],

$$E_{\text{eff}} = \frac{C \alpha^2}{24 T_2 L_2} D^2 L_1 L_2 L_3 \quad (3)$$

where  $C$  is the normal elastic constant of the medium and  $\alpha$  is the inclined angle produced by the shear deformation in the  $[\bar{1}10]$  direction. It can be shown that if the elastic constant of the medium is the same as that of the system, the final energy given by Eq. (3) is roughly reduced by one half due to dissipation in the relaxation process, after the system and the medium are rejoined together.

The total effective energy density is therefore given by

$$E_{\text{tot}} = E_w + E_{\text{el}} = \frac{\sigma_w}{D} + \frac{C \alpha^2}{48 T_2 L} D^2 \quad (4)$$

Minimizing this expression with respect to  $D$  gives rise to the optimal domain size,

$$D = \left( \frac{24 \sigma_w T_2 L_2}{C \alpha^2} \right)^{\frac{1}{3}} \quad (5)$$

When  $D \approx L_2$  the system is in single domain state.

The value  $T_2$  represents an effective coherent range of the stress field from the system medium interface, it approaches a saturated finite value for large medium. In this case the relation becomes a cube root which can be seen from the experimental results in Figure 1.

When the medium size is small however, such as in fine grain size system, the value of  $T_2$  reflects the coherent length of the medium which is approximately the same order as the grain size, i.e.,  $T_2 \sim L_2$ , from Eq. (5) the exponent becomes  $2/3$ .

It is therefore recognized that the elastic boundary conditions can strongly influence the domain sizes in finite grain size systems. For the about case analyzed the exponent,  $m$ , will vary continuously with the grain size and may change from  $2/3$  to  $1/3$  with the increase of grain size.

## Results and Discussions

In the nature of this experiment we must ensure that the obtained domain sizes by the TEM technique are representative of the bulk ceramic but not the ion-beam thinned foils. We found that in order for this to be true, the ferroelectric material must have a moderately high transition temperature compared with sample preparation and observation temperatures. The thermal and mechanical stresses have to be kept to a minimum during the cutting, polishing and ion beam thinning processes. Under these conditions, samples prepared may preserve the bulk domain structures (which are metastable configurations in the thin foil).

Two tests were performed in the PZT samples to verify this fact. First, poled Nb-doped piezoelectric ceramics were thinned and shown to preserve an aligned domain configuration which are expected only in poled sample, as shown in Figure 3 (a-c), indicating there were no major redistribution of the domains during the sample preparation procedure. Second, unpoled ceramic samples were analyzed for domain size distribution after ion beam thinning and later after being heated and cooled slowly through the transition temperature inside the TEM with a hot stage. A difference in the mode and shape of the distribution function of the domain sizes was observed before and after the foils were heated through the transition temperature. The domain sizes are shifted to multi-modal distributions with the majority of domains smaller in the thin foil samples after the heat

treatment; suggesting the domain patterns before heating are metastable. These test results support the claim that carefully prepared TEM samples can preserve domain structures representative of the bulk ceramic in systems with moderately high transition temperatures.

Figure 4 shows a selection of domain structures in a variety of grain size for PZT piezoelectric ceramics. We note in the finer grain ceramics (  $0.2\ \mu\text{m}$  ) the domain walls generally have preferred orientations, in other words, the number of variants becomes less within each grain. The domain walls are generally periodic as shown in Figure 4 (a) and transverse across the entire grain to pin on the grain boundaries. Figure 4 (b) shows a typical domain structure for the soft PZT with a mean grain size  $0.8\ \mu\text{m}$ . Figure 4 (c) shows a multimodal domain size distribution in soft PZT with  $1.8\ \mu\text{m}$  mean grain size after the thinned TEM foil was heated above the transition temperature and then slowly cooled in the microscope. Figure 4(d) is a typical complex multiple variant domain configuration for larger grain sized PZT.

A statistical analysis of the grain and domain sizes is determined directly by measuring scanning electron microscope (SEM) micrographs of etched ceramics and TEM micrographs, respectively. The domains measured were limited to those tilted such that no  $\delta$  fringes are observed; i.e., domain wall planes are parallel to the electron beam direction [18,19]. The histograms for the grain size are in general symmetric and therefore the mode and the mean are almost the same as observed in the typical histograms, Figure 5(a). However, the histograms of the domain size distributions are often skewed, an example is given in Figure 5(b), therefore, the modes of the domain distribution are selected for comparison. The mode in the distribution corresponding to the most probable domain size as indicated in Fig. 5 (a), but not the mean value. The mode values and the errors based on a full width half maximum distribution are listed in Table I.

The experimental values for the domain sizes are plotted against the corresponding grain sizes in Figure 6(a) and (b) for Nb-doped and undoped PZT, respectively. For both compositions of grain sizes between  $1.0\ \mu\text{m}$  and  $10\ \mu\text{m}$  the exponent is found to be

approximately  $m \approx 0.5 \pm 0.03$ , consistent with previous bulk ceramic studies. However, the domain size in the  $0.1 \mu\text{m}$  grain sample show departure from the  $m=1/2$  curve as shown in Fig. 6 (a). Similar departures have been reported for domain structures in the fine grain thin film ferroelectrics [24]. The departure to higher domain densities in submicron grains may be associated with the inhomogeneous strain fields, which also have been found to increase the domain densities in highly defective coelastic crystals [4]. With higher domain densities, one might expect a larger extrinsic contribution to elastodielectric properties, but this is found not to be the case in both PZT fine grain bulk ceramics and thin film studies [25-27]. One possible reason for this is a decrease in the domain mobility and the number of variants in each grain as the grain size decreases. In the case of grain sizes larger than  $10 \mu\text{m}$  our data is limited to one composition and one grain size but it is noted that this point also departs from the parabolic relation in a manner consistent with the course grain  $\text{BaTiO}_3$  ceramics [see the upper curve in Fig. 6 (b)].

The domain structures observed in the poled PZT ceramics are shown to be strongly influenced by the neighboring grain domain structures, both with regard to domain wall spacing and orientations. Figure 3 (a) and (b) clearly show a transgranular elastic coupling, which can only be explained through cooperative intra- and trans-granular domain switching. Figure 3(a) shows grain #3 with two sets of periodic ferroelastic twins,  $\text{DW}^x$  and  $\text{DW}^y$ , which couple respectively to domain configurations in the adjacent grains labeled #1 and #2 respectively. Figure 3 (b) also shows transgranular coupling of poled domain structures. This micrograph shows the grain boundary between grains #2 and #3 perturbs the periodicity of domain structure in grain #1. Transgranular coupling is also of practical importance for fine grained thin film piezoelectric materials for devices such as micromotors. Grain boundary phases must be kept at a minimum to maximize the transgranular coupling. The transgranular coupling and their relation to elastodielectric properties will be the focus of future investigations in the domain structures of PZT ceramics.

## Conclusions

Through a simple model we have shown that the relation between domain size and grain sizes may not be parabolic, instead, it depends strongly on the boundary conditions and the geometry of the system and the size of surrounding medium. For very large grain system, the exponent  $m$  should be  $1/3$ , and  $m$  increases with decreasing grain size. Experimentally we found that for grain size between  $1.0 - 10 \mu\text{m}$  range, the parabolic relation ( $m=1/2$ ) can reasonably describe the domain size grain size relation for bulk ceramic hard and soft PZTs. Deviation from the parabolic relation to higher domain densities were found in systems with grain size greater than  $10 \mu\text{m}$  and less than  $1 \mu\text{m}$ , consistent with the trend predicted in the theoretical analysis.

Experiments were conducted to establish the TEM technique as a valid method for domain size assessment in bulk ceramics. Using poled samples and heating cycles, the domain size were confirmed to reflect that of the bulk ceramic when the samples were prepared at temperatures much below the transition temperature. Domain redistribution reflecting the new boundary conditions of the thin foil was found only after the samples were heated to temperatures near  $T_c$ .

Additionally, it was noted that fine grain ferroelectrics ( $< 1 \mu\text{m}$ ) often contain one or two set of simple twin bands, while larger grains can have many cross hatching twin band structures. The result of fine grains having simple domain structures implies a reduction in the degrees of freedom a particular grain can readily deform under the transition. The reduced variants combined with the surface pinning of the domain walls may be the cause for the reduction of domain wall mobility and hence the associated extrinsic elasto-dielectric properties for fine grain PZT ceramics and thin films.

The poled ceramic samples reveal direct evidence of the domain switching process involving both intragranular and transgranular cooperation. The transgranular switching indicates that the non- $180^\circ$  domains have strong semi-coherent elastic coupling across grain boundaries.

**Acknowledgments:**

We wish to thank Drs. T. R. Shrout and N. Kim for the supplying of the ceramic samples in the TEM studies. The authors are also wish to acknowledge many insightful conversations with Drs. L.E. Cross, R.E. Newnham, and T.R. Shrout. This research is supported by the National Science Foundation under Grant MRG DMR-92-23847.

## References

1. Fousek J. and Janovec V., J. Appl. Phys., **40**, 135 (1969).
2. Sapriel J., Phy. Rev., B **12**, 5182 (1975).
3. Khachaturyan A. G., Theory of Structural Transformations in Solids, John Wiley & Sons, New York, 1983.
4. Salje E., Phase Transitions in Ferroelastic and Coelastic Crystals, Cambridge Univeristy Press (1990).
5. Kittel C., Phy. Rev., **70**, 965 (1946).
6. Mitsui T. and Furuichi J., Phy. Rev., **90**, 193 (1953).
7. Arlt G., Ferroelectrics, **104**, 217 (1990).
8. Chenskii E. V., Sov. Phy. Solid-State, **14**, 1940 (1973).
9. Buessem W. R., Cross L.E., Goswami A.K., J. Am. Ceram. Soc., **49**, 33 (1966).
10. Swartz S. L., I.E.E.E. Trans. on Elect. Insulator, **25**, 935 (1990).
11. Whatmore R.W., A. Patel, Shorrocks N.M. and Ainger F.W., Ferroelectrics, **104**, 269 (1990).
12. Cross L. E. (private communication).
13. Randall C.A., Rossetti G.A. and Cao W., Ferroelectrics, **150**, 163 (1993).
14. Philippe P., Dougherty J.P. and Shrout T.R., J. Mater. Res. **5**, 2901 (1990).
15. Shrout T.R., Proc. 1st International Meeting on Chem. of Electr. Cerm. Mater.(1990).
16. Kim N., Grain Size Effect on Dielectric and Piezoelectric Properties in Compositions Near the MPB of PZT Ceramics, Ph. D. Thesis, The Pennsylvania State University (1994).
17. Jaffe B., Cook W.R. and Jaffe H., Piezoelectric Ceramics, Academic Press (1971).
18. Gevers R., Blank H. and Amelinckx S., Phys. Stat. Sol., **13**, 449 (1966).
19. Randall C.A., Barber D.J. and Whatmore R.W., J. Mat. Sci., **22**, 925 (1987).
20. Cao W. and Cross L. E., Phys. Rev., B **47**, 4825 (1993).

21. Landau L.D., Phys. Z.Sowjun, **11**, 26 (1937); *ibid*, 545.
22. Cao W. and Cross L. E., Phys. Rev., B **44**, 5 (1991).
23. Eshelby J.D., Ann. Physik, **1**, 116(1958).
24. Cao W., Ferroelectrics, in press (1995).
25. Tuttle B., Voigt J., Headley T.J., Potter B.G., Dimos D., Schwartz R.W., Duggan M.T., Michael J., Nasby R.D., Garino T.J., and Goodnow D.C., Ferroelectrics **151**, 11 (1994).
26. Demartin M., Carry C., and Setter N., Proceedings, 4th Int. Conf. on Electron. Ceram. and Applications, 393 (1994).
27. Eatough M., Dimos D., Tuttle B., MRS Fall Meeting (1994).



## Figure Captions

- Figure 1. Domain size versus grain size for BaTiO<sub>3</sub> ceramics, experimental results compared to parabolic relation (after Arlt 1990, ref. 7).
- Figure 2. (a) Schematic illustration of a 90° twin band attached to and substrate medium with a fixed bottom.  
(b) Coordinate system and a section of (a) with only one tetragonal domain.
- Figure 3. (a) – (c) Multi-beam bright field TEM images of domain structures in a poled PZT ceramic foil.
- Figure 4. Typical bright field images of ferroelectric domain structures in (a) 0.2 μm, (b) 0.8 μm, (c) 1.8 μm, and (d) 14 μm bulk ceramics.
- Figure 5. Typical histograms of (a) grain size distribution of undoped PZT,  $G_{mode} = 0.8 \mu m$  and (b) domain size distribution of Nb-doped PZT,  $D_{mode} = 0.2 \mu m$ .
- Figure 6. (a) Logarithmic plot of measured domain size versus grain size for Nb-doped PZT ceramics and the parabolic relation.  
(b) Comparison of the domain size grain size relation in undoped PZT and large grain BaTiO<sub>3</sub>. The exponent,  $m$ , for BaTiO<sub>3</sub> of large grains is  $\sim 1/3$  while for PZT is  $\sim 1/2$  except the largest grain sample show deviation to higher domain density.

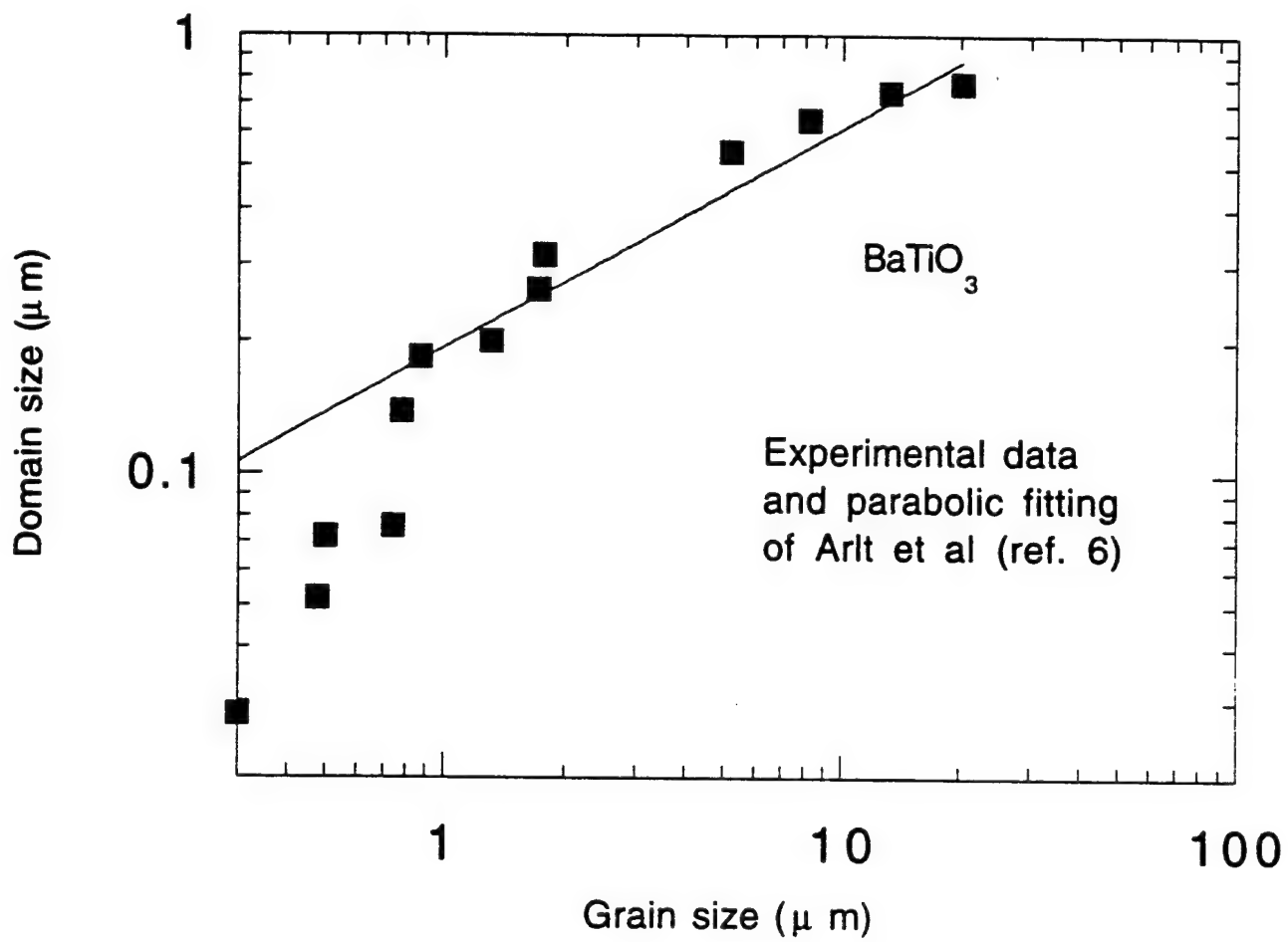


Fig. 1

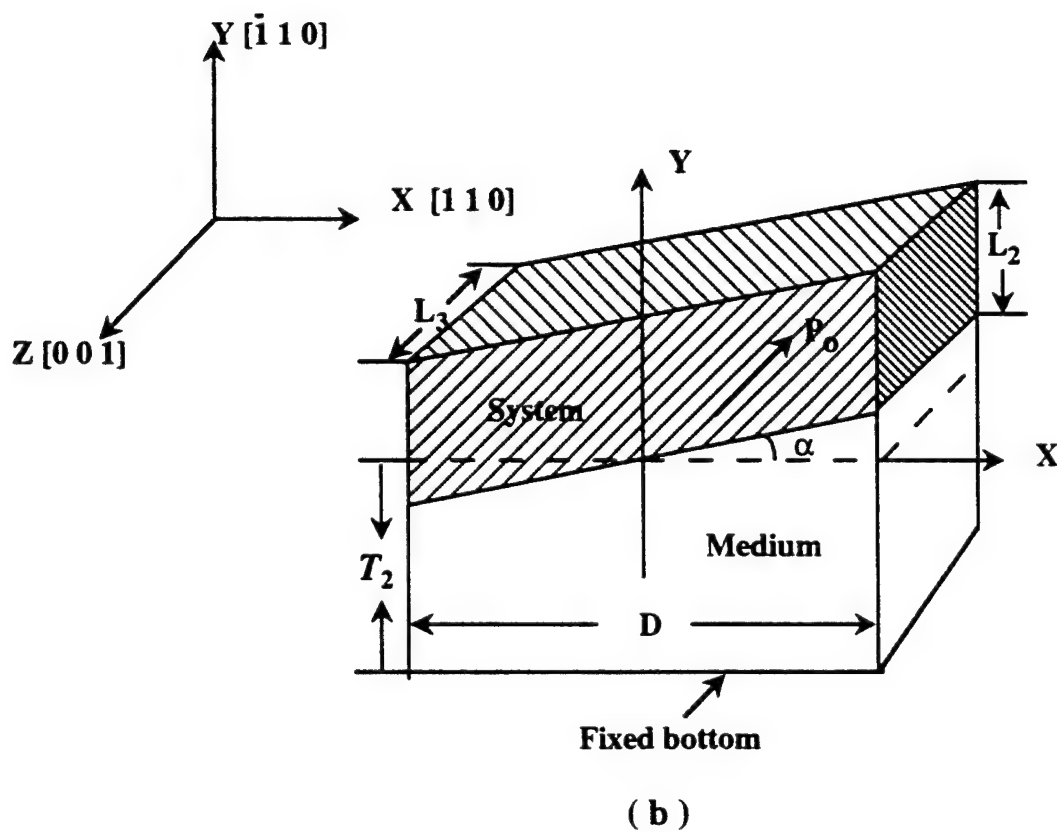
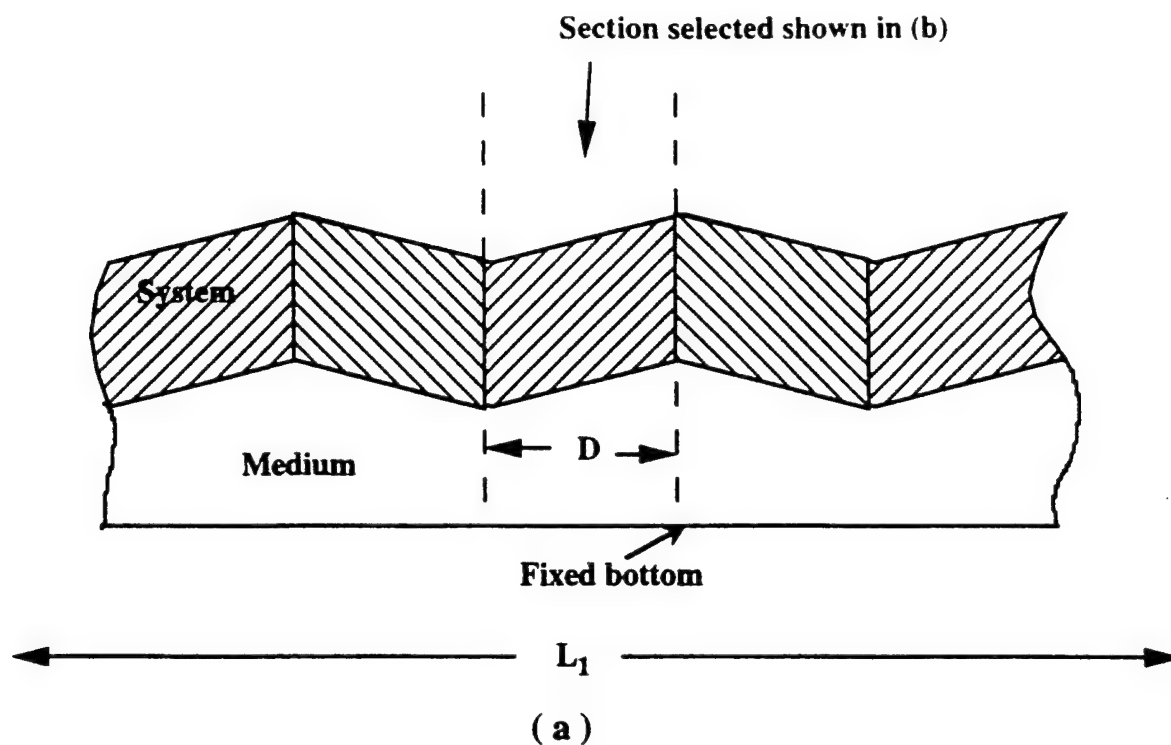


Figure 2



Fig. 3

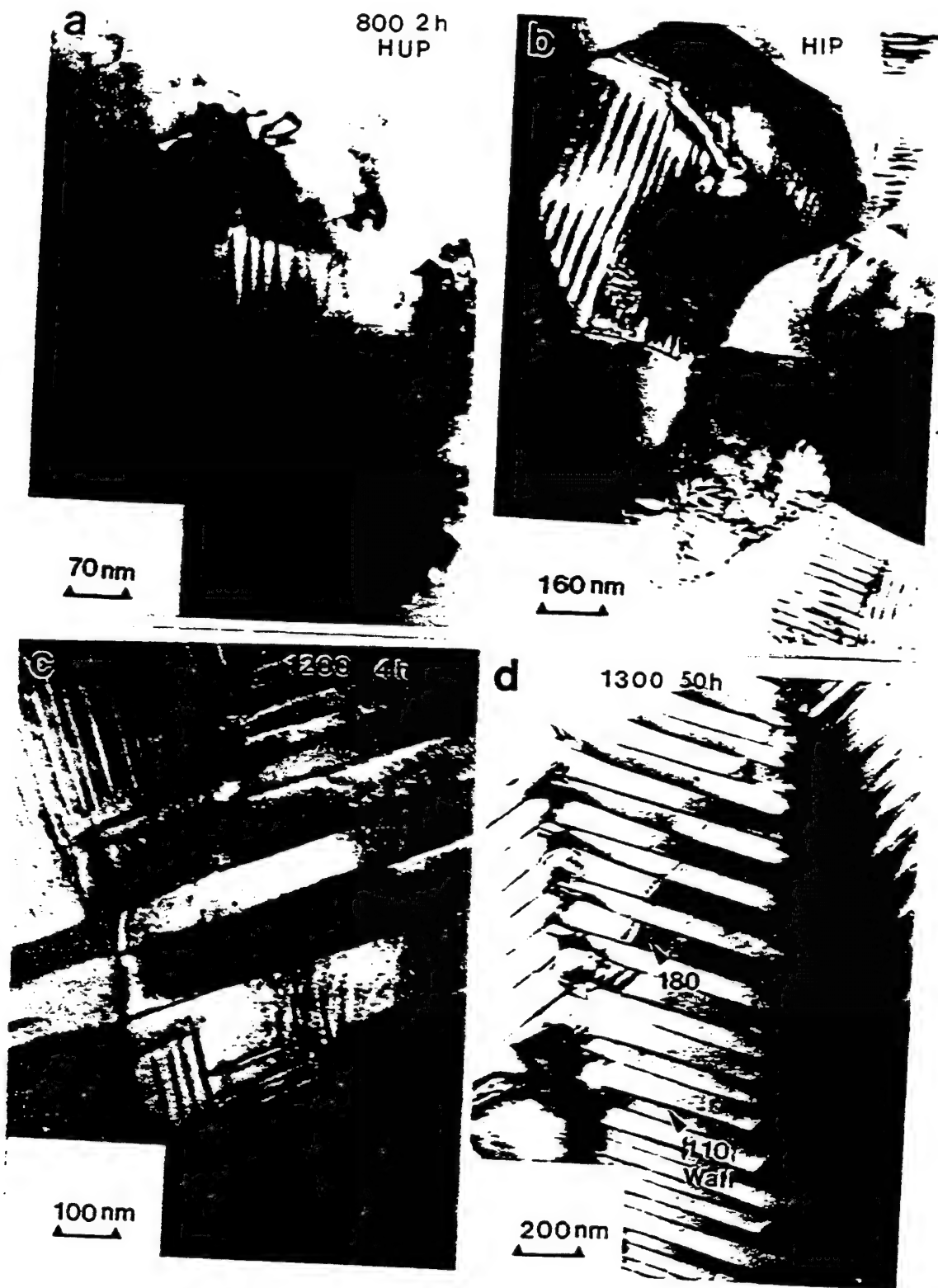


Fig. 4

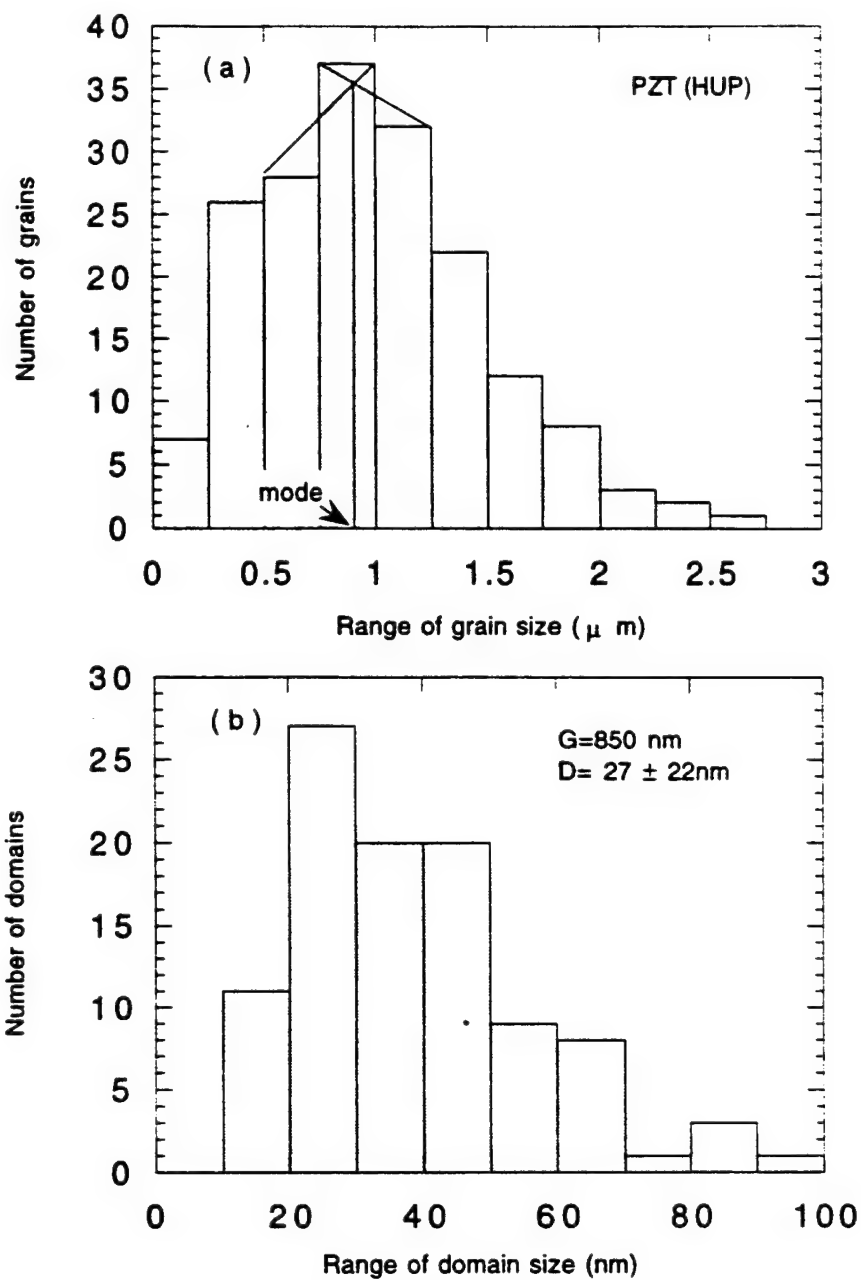


Fig. 5

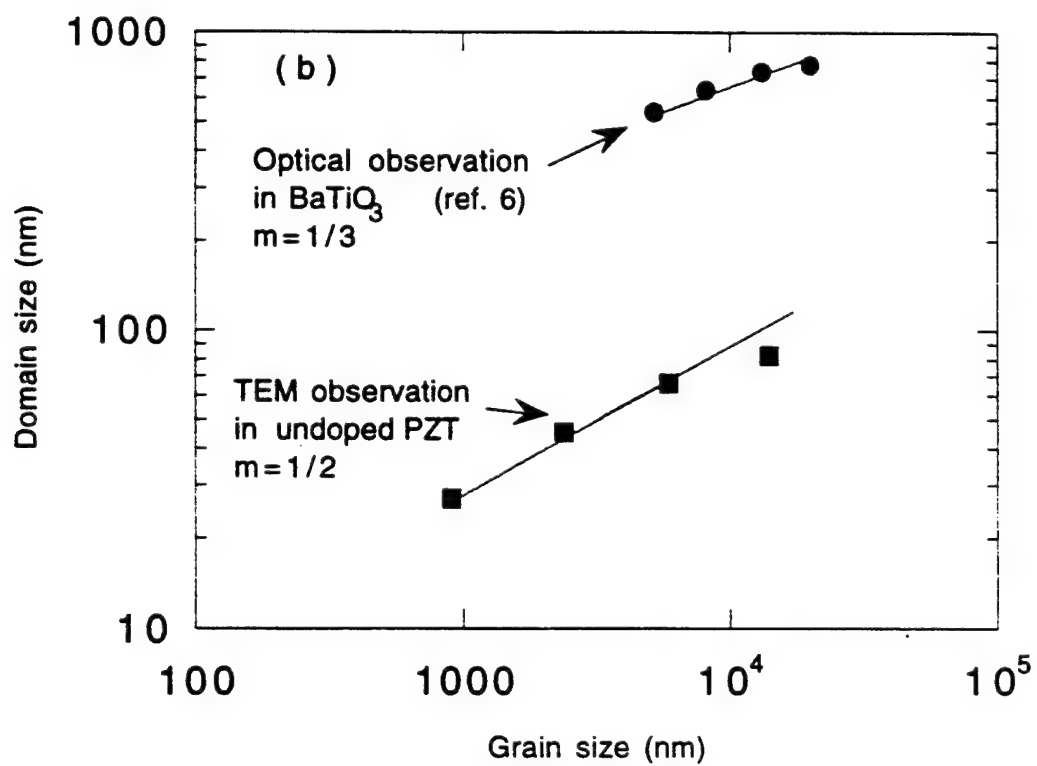
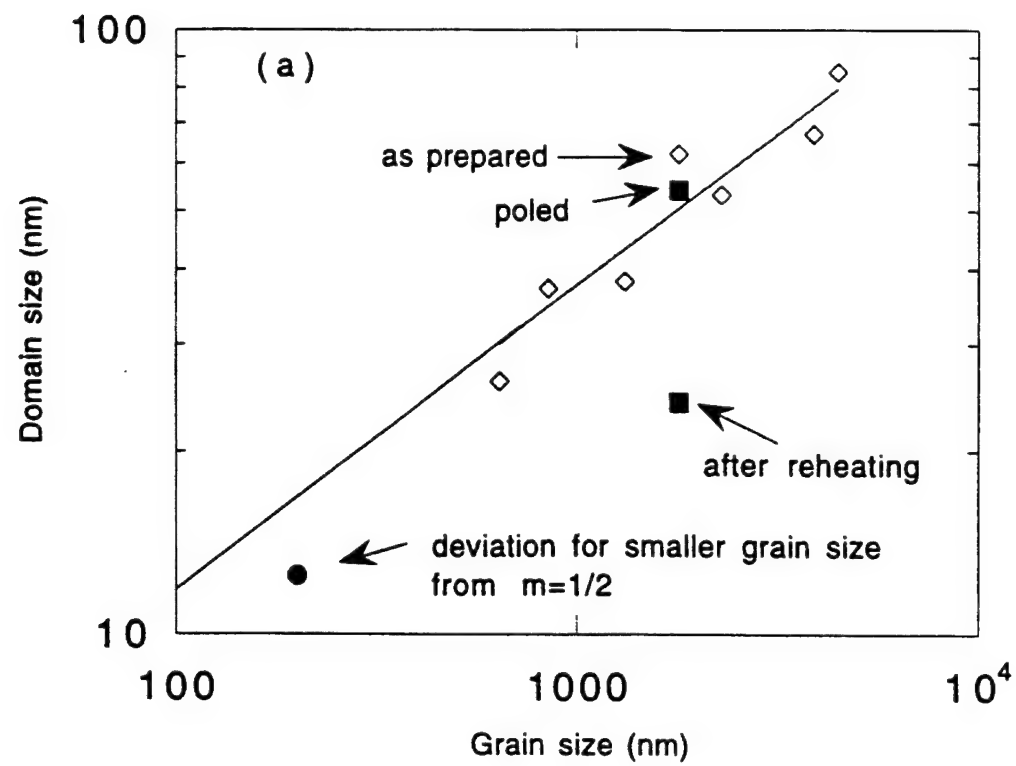


Fig. 6

Table I Sintering conditions for the PZT samples, and the measured grain size, domain size and the estimated errors.

Nb-Doped PZT						
Firing Conditions	Mean Grain Size ( $\mu\text{m}$ )	Mode Grain Size ( $\mu\text{m}$ )	Standard Error of Grain Size ( $\mu\text{m}$ )	Mode Domain Size (nm)	Estimated Domain Size Error in Mode ( $\pm$ nm)	Comments
800/2 hours	0.17	0.16	0.005	12	3	Hot Pressed
970°C/4 hrs 900°C/2 hrs	0.64	---	0.020	30	15	Conventional & HIP
1000°C/4 hrs	0.85	0.78	0.020	37	22	Conventional
1100°C/4 hrs	1.32	1.30	0.025	38	10	Conventional
1200°C/4 hrs	1.82	---	0.030	63	12.5	Conventional
1250°C/4 hrs	2.30	---	0.038	53	8.5	Conventional
1300°C/50 hrs	3.95	3.85	0.230	67	11	Conventional
Unknown*	4.5†	---	---	85		†Grain size determined from line intercept
*Commercial soft PZT						
Undoped PZT						
Firing Conditions	Mean Grain Size ( $\mu\text{m}$ )	Mode Grain Size ( $\mu\text{m}$ )	Standard Error of Grain Size ( $\mu\text{m}$ )	Domain Size (mode)(nm)	Estimated Domain Size Error in Mode ( $\pm$ nm)	Comments
800/2 hrs	0.98	0.82	0.037	26	9.5	Hot pressed
1000°C/4 hrs	2.4	2.2	0.12	49	20	Conventional
1200°C/4 hrs	5.9	---	0.19	66	10	Conventional
1300°C/50 hrs	14.3	12.5	0.59	82	13	Conventional



Table 1 Sintering conditions for the PZT samples, and the measured grain size, domain size and the estimated errors.

Nb-Doped PZT						
Firing Conditions	Mean Grain Size ( $\mu\text{m}$ )	Mode Grain Size ( $\mu\text{m}$ )	Standard Error of Grain Size ( $\mu\text{m}$ )	Mode Domain Size (nm)	Estimated Domain Size Error in Mode ( $\pm$ nm)	Comments
800/2 hours	0.17	0.16	0.005	12	3	Hot Pressed
970°C/4 hrs 900°C/2 hrs	0.64	---	0.020	30	15	Conventional & HIP
1000°C/4 hrs	0.85	0.78	0.020	37	22	Conventional
1100°C/4 hrs	1.32	1.30	0.025	38	10	Conventional
1200°C/4 hrs	1.82	---	0.030	63	12.5	Conventional
1250°C/4 hrs	2.30	---	0.038	53	8.5	Conventional
1300°C/50 hrs	3.95	3.85	0.230	67	11	Conventional
Unknown*	4.5†	---	---	85		†Grain size determined from line intercept *Commercial soft PZT
Undoped PZT						
Firing Conditions	Mean Grain Size ( $\mu\text{m}$ )	Mode Grain Size ( $\mu\text{m}$ )	Standard Error of Grain Size ( $\mu\text{m}$ )	Domain Size (mode)(nm)	Estimated Domain Size Error in Mode ( $\pm$ nm)	Comments
800/2 hrs	0.98	0.82	0.037	26	9.5	Hot pressed
1000°C/4 hrs	2.4	2.2	0.12	49	20	Conventional
1200°C/4 hrs	5.9	---	0.19	66	10	Conventional
1300°C/50 hrs	14.3	12.5	0.59	82	13	Conventional

# **APPENDIX 19**

# Defect Stabilized Periodic Amplitude Modulations in Ferroelectrics

Wenwu Cao

Materials Research Laboratory  
The Pennsylvania State University  
University Park, PA 16802

## ABSTRACT

Theoretical analysis shows that the total free energy of a ferroelectric system with free boundary conditions increases with the number of the inhomogeneous regions, such as domain walls and other modulated structures. However, charged defects could lower the total energy of a ferroelectric system by interacting with the charge density fluctuations in the inhomogeneous regions. We discuss a special kind of inhomogeneous microstructure in a lanthanum doped lead titanate, the amplitude modulations, which can be stabilized by the aliovalent dopants.

Keywords: Defects, precursor, modulations, ferroelectrics, doping

## I. INTRODUCTION

There are many known microstructures in ferroic systems, such as twinbands, microtwinning, tweed, etc., particularly in many proper and improper ferroelastic systems (Tanner, Pelton and Gronsby, 1982; Clapp, Rifkin and Tanner, 1988; Osjima, Sugiyama and Fujima, 1988) including high  $T_c$ - superconductors (Schmahl, et al, 1989). In many cases, complex microstructure are originated from localized stress or strain due to defect doping (Cao and Krumhansl, 1990; Falk, 1982; Salje, 1990).

These microstructures not only fascinate scientists but also control the physical properties of ferroic materials. They have a strong dependence on the nature and number of defects in the system. In some cases, an intrinsic excitation of the system is the driving force for the ordering of the defects and these ordered defects play the role of pinning centers to stabilize the intrinsic excitations of the system which otherwise will be unstable or metastable.

Recently a new type of spatial amplitude modulation is reported in a lanthanum doped lead titanate solid solution system,  $Pb_{1-y}La_yTiO_3$ , as shown in Fig. 1 (Randall, Rossetti and Cao, 1994; Rossetti, Cao and Randall, 1994). Fig. 1 (a)-(d) are the bright field image of the microstructures for La content of 1%, 5%, 10%, and 25%. One can see that a modulation is developing with the lanthanum content and it is the most pronounced in Fig. 1(c) where clear modulations are shown inside each of the domains. Through the change of the image conditions it is found that the modulations are not microtwinning, instead, they are amplitude modulations with the polarization directions unchanged (Randall, Rossetti and Cao, 1994; Rossetti, Cao and Randall, 1994). In other words, the wave vector of the modulation is oriented in the same direction as that of the polarization.

Obviously, from the sequence of Fig. 1, this modulated structure is induced by the lanthanum dopants. It is the results of the interaction between these aliovalent dopants and an inhomogeneous periodic excitations in the system. In what follows, we will derive this intrinsic excitations in a system with first order phase transition by using the Landau-Ginzburg theory, and also discuss the mechanism for the formation of the microstructures shown in Fig. 1 (c) in terms of defect stabilization of metastable and/or unstable microstructures of a pure system.

## II. LANDAU-GINZBURG MODEL

Cao and Cross (1991) have developed a continuum model for the  $O_h$ - $C_{4v}$  proper ferroelectric phase transition based on Landau-Ginzburg theory. The free energy density can be written as the following:

$$F(P_i, P_{i,j}, \eta_{kl}) = F_L(P_i) + F_{el}(\eta_{kl}) + F_c(P_i, \eta_{kl}) + F_G(P_{i,j}) \quad (1)$$

where  $F_L(P_i)$  is the Landau energy for the polarization,

$$F_L(P_i) = \alpha_1 (P_1^2 + P_2^2 + P_3^2) + \alpha_{11} (P_1^2 + P_2^2 + P_3^2)^2 + \alpha_{12} (P_1^2 P_2^2 + P_2^2 P_3^2 + P_1^2 P_3^2) + \alpha_{111} (P_1^6 + P_2^6 + P_3^6) + \alpha_{112} [P_1^4 (P_2^2 + P_3^2) + P_2^4 (P_1^2 + P_3^2) + P_3^4 (P_1^2 + P_2^2)] + \alpha_{123} P_1^2 P_2^2 P_3^2, \quad (2)$$

$F_{el}(\eta_{kl})$  is the elastic energy of the system,

$$F_{el}(\eta_{kl}) = \frac{C_{11}}{2} (\eta_{11}^2 + \eta_{22}^2 + \eta_{33}^2) + C_{12} (\eta_{11}\eta_{22} + \eta_{11}\eta_{33} + \eta_{22}\eta_{33}) + 2C_{44} (\eta_{12}^2 + \eta_{13}^2 + \eta_{23}^2), \quad (3)$$

$F_c(P_i, \eta_{kl})$  represents the coupling between the primary and the secondary order parameters,

$$F_c(P_i, \eta_{kl}) = -q_{11} (\eta_{11} P_1^2 + \eta_{22} P_2^2 + \eta_{33} P_3^2) - q_{12} [\eta_{11} (P_2^2 + P_3^2) + \eta_{22} (P_1^2 + P_3^2) + \eta_{33} (P_1^2 + P_2^2)] - 2q_{44} (\eta_{12} P_1 P_2 + \eta_{13} P_1 P_3 + \eta_{23} P_2 P_3), \quad (4)$$

and  $F_G(P_{i,j})$  is the lowest order gradient energy, which has the independent invariant form of

$$F_G(P_{i,j}) = \frac{1}{2} g_{11} (P_{1,1}^2 + P_{2,2}^2 + P_{3,3}^2) + g_{12} (P_{1,1} P_{2,2} + P_{1,1} P_{3,3} + P_{2,2} P_{3,3}) + \frac{g_{44}}{2} [(P_{1,2} + P_{2,1})^2 + (P_{1,3} + P_{3,1})^2 + (P_{2,3} + P_{3,2})^2]. \quad (5)$$

The physical meaning of the expansion coefficients can be found in the original paper of Cao and Cross (1991), and all the coefficients are assumed to be independent of temperature except  $\alpha_1$ ,

$$\alpha_1 = \alpha_0 (T - T_0). \quad (6)$$

Minimizing the free energy Eq. (1) with respect to the polarization and the elastic displacement field give the following solutions for a homogeneous system (Cao and Cross, 1991):

(i) For  $T > T_1$ ,

$$\text{where } T_1 = T_0 + \frac{\alpha'_{11}{}^2}{3\alpha_0\alpha_{111}}, \quad \alpha'_{11} = \alpha_{11} - \frac{\hat{q}_{11}^2}{6\hat{C}_{11}} - \frac{\hat{q}_{22}^2}{3\hat{C}_{22}},$$

and

$$\begin{aligned}\hat{C}_{11} &= C_{11} + 2C_{12}, \\ \hat{C}_{22} &= C_{11} - C_{12},\end{aligned}$$

$$\begin{aligned}\hat{q}_{11} &= q_{11} + 2q_{12}, \\ \hat{q}_{22} &= q_{11} - q_{12},\end{aligned}$$

we have the solution for the cubic phase,

$$P_i = 0, \eta_{ij} = 0, (i, j = 1, 2, 3). \quad (7)$$

(ii) For  $T_1 > T > T_c$ , where  $T_c = T_0 + \frac{\alpha'_{11}{}^2}{4\alpha_0\alpha_{111}}$  is the phase transition temperature,

there are two solutions:

$$(a) \quad P_i = 0, \eta_{ij} = 0, (i, j = 1, 2, 3); \quad (8)$$

$$(b) \quad \vec{P} = (\pm P_T, 0, 0), (0, \pm P_T, 0), (0, 0, \pm P_T), \quad (9)$$

with

$$P_T = \sqrt{\frac{-\alpha'_{11} + \sqrt{\alpha'_{11}{}^2 - 3\alpha_1\alpha_{111}}}{3\alpha_{111}}}, \quad (10)$$

$$\eta_{11} = \frac{P_T^2}{3} \left( \frac{\hat{q}_{11}}{\hat{C}_{11}} + \frac{2\hat{q}_{22}}{\hat{C}_{22}} \right), \quad (11)$$

$$\eta_{\perp} = \frac{P_T^2}{3} \left( \frac{\hat{q}_{11}}{\hat{C}_{11}} - \frac{\hat{q}_{22}}{\hat{C}_{22}} \right), \quad (12)$$

$$\eta_{ij} = 0, (i \neq j), (i, j = 1, 2, 3). \quad (13)$$

Here  $\eta_{||}$  and  $\eta_{\perp}$  are the normal strain components in the directions parallel and perpendicular to the tetragonal axis in each of the three tetragonal states, respectively,  $P_T$  is the amplitude of the spontaneous polarization in the tetragonal phase.

Solution (a) represents a thermodynamically stable cubic phase and (b) indicates that an additional tetragonal metastable phase also exist in this temperature region. This metastable phase can be stabilized to become the ferroelectric phase with further cooling.  $T_c$  is the phase transition temperature, at which the free energies of the cubic and tetragonal phases are equal.

(iii) For  $T_c \geq T > T_0$ ,

solutions (a) and (b) in (ii) exist, but in this temperature region the tetragonal phase becomes thermodynamically stable and the cubic phase becomes metastable.

(iv) For  $T < T_0$ ,

only the tetragonal phase exists [solution (b) in (ii)].

The interesting temperature region is  $T_1 > T > T_0$ , in which there are two solutions with one being stable and the other being metastable. When the system has higher energy, a modulation swinging back and forth between the two (local) minima can be excited.

### III. INTRINSIC AMPLITUDE MODULATIONS

In the study of martensitic phase transition, Falk (1993), Barsch and Krumhansl (1988), have derived periodic solutions for the martensite-martensite and martensite-austenite structures. Similarly, we can also derive such periodic solutions for a ferroelectrics system using the Landau-Ginzburg type of model described above (Cao and Cross, 1991).

Considering the nature of the modulation shown in Fig. 1 (c) the problem may be rendered to quasi-one-dimensional with a space variation only along the polarization direction. Similar to the study of  $180^\circ$  domains (Cao and Cross, 1991) we assume here the following *ansatz* for the polarization and strain,

$$\vec{P} = (0, 0, P_3(x_3)), \quad (14)$$

$$\eta_{ij} = \eta_{ij}(x_3) \quad (15)$$

Note here the space variable is  $x_3$ , the same as the polarization direction, while for the  $180^\circ$  domain structure the space variable is perpendicular to the polarization direction (Cao and Cross, 1991).

Substituting the Eqs. (14) and (15) into the energy minimization conditions and the elastic compatibility relations (Cao and Cross, 1991) lead to a second order nonlinear ordinary differential equation for  $P(x_3)$ ,

$$2\alpha_1^+ P_3 + 4\alpha_{11}^+ P_3^3 + 6\alpha_{111} P_3^5 - g_{11} P_{3,33} = 0 \quad (16)$$

with

$$\alpha_1^+ = \alpha_1 - \left[ \frac{\hat{C}_{22}}{C_{11}} q_{12} \eta_{\perp} + \left( q_{11} - \frac{C_{12}}{C_{11}} q_{12} \right) \eta_{\parallel} \right] \quad (17)$$

$$\alpha_{11}^+ = \alpha_{11} - \frac{q_{12}^2}{2C_{11}} \quad (18)$$

Equation (16) is equivalent to a one-dimensional model with an effective free energy density of

$$\begin{aligned} f_{\text{eff}} &= \frac{g_{11}}{2} (P_{3,3})^2 + \alpha_1^+ P_3^2 + \alpha_{11}^+ P_3^4 + \alpha_{111} P_3^6 \\ &= \frac{g_{11}}{2} (P_{3,3})^2 + f_L \end{aligned} \quad (19)$$

where  $f_L$  is the Landau-like potential as plotted in Fig. 2.

Direct integration of Eq. (16) leads to the following result:

$$x_3 = \frac{\sqrt{g_{11}}}{2} \int \frac{dP_3}{\sqrt{\alpha_1^+ P_3^2 + \alpha_{11}^+ P_3^4 + \alpha_{111} P_3^6 - f_0}} \quad (20)$$

One can obtain different solutions depending on the value of the integration constant  $f_0$ . For temperature region  $T_c < T < T_1$ , we are interested for an  $f_0$  value in the range of  $f_{\min} < f_0 < f_{\max}$  as shown in Fig. 2. In this case, Eq. (20) can be integrated (Gradshteyn and Ryzhik, 1980) and the polarization has the following solution:

$$P_3(x_3) = \frac{\gamma_1}{\sqrt{1 - \left[ 1 - \frac{\gamma_1^2}{\gamma_2^2} \right] \text{sn}^2(x_3/\beta', k)}} \quad (21)$$



and

$$\beta' = \frac{1}{\gamma_2} \sqrt{\frac{g_{11}}{2\alpha_{111}(\gamma_3^2 - \gamma_1^2)}} \quad (22)$$

$$k = \frac{\gamma_3}{\gamma_2} \frac{\sqrt{\gamma_2^2 - \gamma_1^2}}{\sqrt{\gamma_3^2 - \gamma_1^2}} \quad (23)$$

where  $\gamma_i$  are the roots of the radicand in the integrand of Eq. (20) and  $\text{sn}(x)$  in Eq. (21) is an elliptic sine function. The solution Eq. (21) is periodic with a period of

$$x_p = 2\beta'K(k) \quad (24)$$

where  $K(k)$  is a complete elliptic integral of the first kind.

Fig. 3 is an illustration of the amplitude modulation solution for a special set of parameters in normalized scale. The polarization is normalized in terms of the spontaneous polarization at  $T_c$ ,

$$P_0 = \sqrt{\frac{\alpha_{11}^+}{2\alpha_{111}}} \quad (25)$$

while the space variable is normalized by a factor  $x_0$ ,

$$x_0 = \sqrt{\frac{2\alpha_{111} g_{11}}{\alpha_{11}^+}} \quad (26)$$

The amplitude of the polarization oscillates in space between two values that are less than the polarization value of the fully developed tetragonal phase,  $P_T$ , while the direction of the polarization is fixed. The coupling of this polarization to the elastic strain makes the modulation visible to the electron microscopy.

#### IV. INTERACTION BETWEEN THE AMPLITUDE MODULATION AND ALIOVALENT DOPING

As shown in Fig. 2 that the amplitude modulation solution oscillating between  $\gamma_1$  and  $\gamma_2$  has higher energy than both the stable and the metastable states (cubic and tetragonal phases respectively in the case discussed above), but it can be locally stable (in configurational space) once being excited (Barsch and Krumhansl, 1988). The excitation has two distinct features:

1. It exists only in a limited temperature range, i.e.,  $T_0 < T < T_1$ , hence may be closely related to the 'precursor' and the 'postcursor' in a first order transition.
2. The period of the modulation is incommensurate with the lattice structure and change continuously with temperature.

However, when aliovalent doping is introduced into the system, the situation will be changed. The existence of inhomogeneous polarization modulation means the presence of polarization gradient in the system. From electrostatics, there will be charge density fluctuations in space associated with these polarization gradients. These charge density fluctuations will interact with the aliovalent dopants which have excess charge, causing some ordering of these charged defects. On the other hand, the ordering of these defects will pin the modulations so that the period will become commensurate with the underlying lattice structure and may become temperature independent. In other words, the defect ordering will persist for lower temperatures as an modulation to the tetragonal phase. These facts are consistent with the experimental observations in the lanthanum doped lead titanate shown in Fig. 1(c) (Randall, Rossetti and Cao, 1993).

Because the charge density fluctuations are produced at a certain temperature, they have a defined magnitude for specified boundary conditions, and certain amount of defects ( $> 5\%$ ) are needed to stabilize the microstructure as indicated in Fig. 1.

In conclusion, the amplitude modulation observed in lanthanum doped lead titanate shown in Fig. 1 can be understood as the results of defect stabilized intrinsic solitary periodic excitations which exist in systems with a first order phase transition.

#### ACKNOWLEDGMENTS

The author is indebted to Drs. G. R. Barsch, J. A. Krumhansl, C. A. Randall, G. A. Rossetti Jr. and L. E. Cross for many beneficial discussions. This research was supported by the ONR under Grant No. N00014-92-J-1501 and NSF under Grant No. DMR-92-23847.

## REFERENCES

- Cao, W. and L. E. Cross (1991), Phys. Rev. B **44**, 5.
- Cao, W., J. A. Krumhansl (1990), Phys. Rev. B **42**, 4334.
- Cao, W., J. A. Krumhansl and R. J. Gooding (1990), Phys. Rev. B **41**, 11319.
- Clapp, P. C., J. Rifkin, J. Kenyon, and L. E. Tanner (1988), Metall. Trans. A., **19**, 783.
- Barsch G. R. and J. A. Krumhansl (1988), Met. Trans. A, **19**, 761.
- Falk. F. (1982), J. de Physique, **43**, C4-3.
- Falk F. (1983), Z. Physik B - Condensed Matter **51**, 177.
- Gadshteyn I. S. and I. M. Ryzhik (1980), Table of Integrals, Series and Products, Academic Press Inc., New York.
- Osjima R., M. Sugiyama, and F. E. Fujita (1988), Metall. Trans. A, **19**, 803.
- Randall C. A., G. A. Rossetti, Jr., and W. Cao (1993), Ferroelectrics, **150**, 163.
- Rossetti G. A., Jr, W. Cao and C. A. Randall (1994), Ferroelectrics, **158**, 343.
- Salje, E. K. H. (1990), Phase Transitions in Ferroelastic and Coelastic Crystals, Cambridge University Press, Cambridge.
- Schmahl, W. W., A. Putnis, E. Salje, P. Freeman, A. Graeme-Barber, R. Jones, K. K. Singh, J. Blunt, P. P. Edwards, J. Loram and K. Mirza (1989), Phil. Mag. Letters, **60**, 214.
- Tanner, L. E., A. R. Pelton, and R. Gronsby (1982), J. de Phys. Suppl. 12, **43**, C4-169.

## FIGURE CAPTIONS

- Figure 1      Bright field image of microstructures in a solid solution series  $(\text{Pb}_{1-3x/2}\text{La}_x)\text{TiO}_3$ . (a) 1% at. La - only the regular domain structure. (b) 5% at. La - some texture inside the domains; (c) 10% at. La - periodic modulations inside the domains; (d) 25% at. La show no regular domains (after Randall, Rossetti and Cao, 1993).
- Figure 2      Effective free energy for temperature  $T$  with  $T_1 > T > T_0$ . The modulation reflects a periodic solution for the polarization between the two values  $\gamma_1$  and  $\gamma_2$ .
- Figure 3      The tetragonal strain along the polarization direction accompanying the periodic polarization modulation.

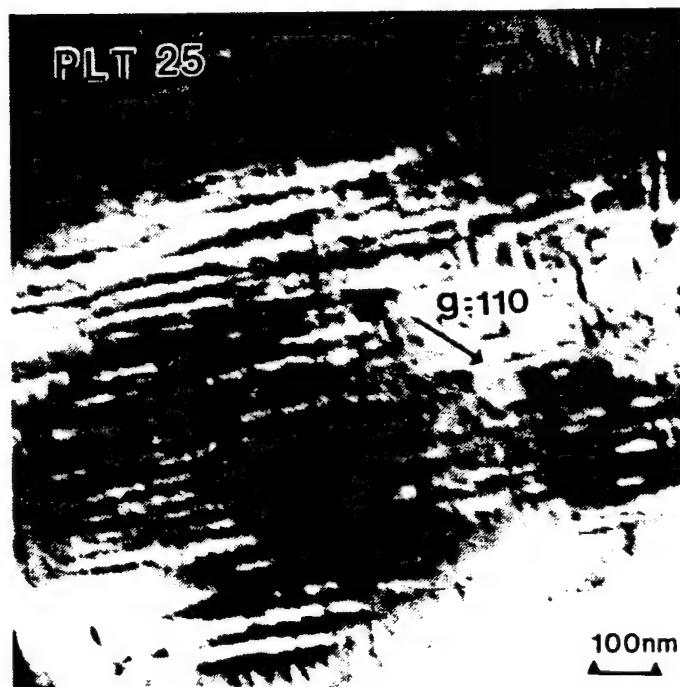
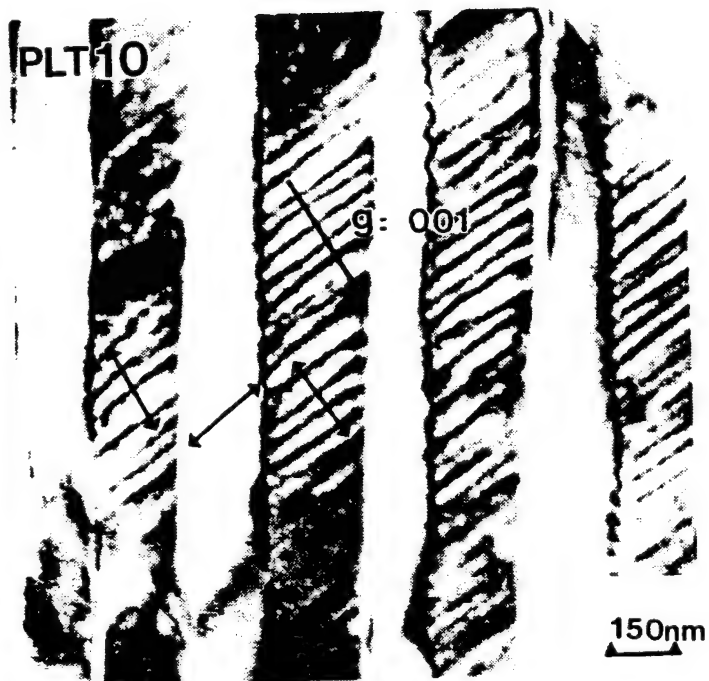
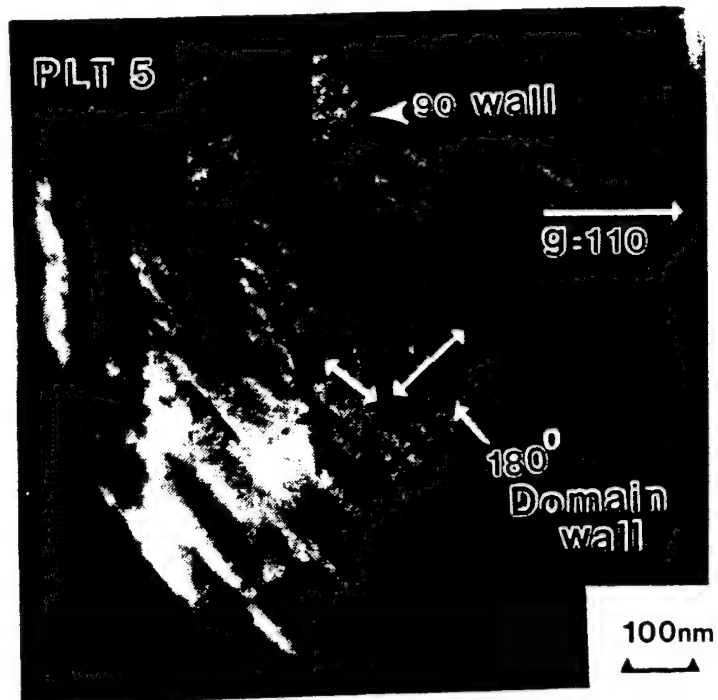
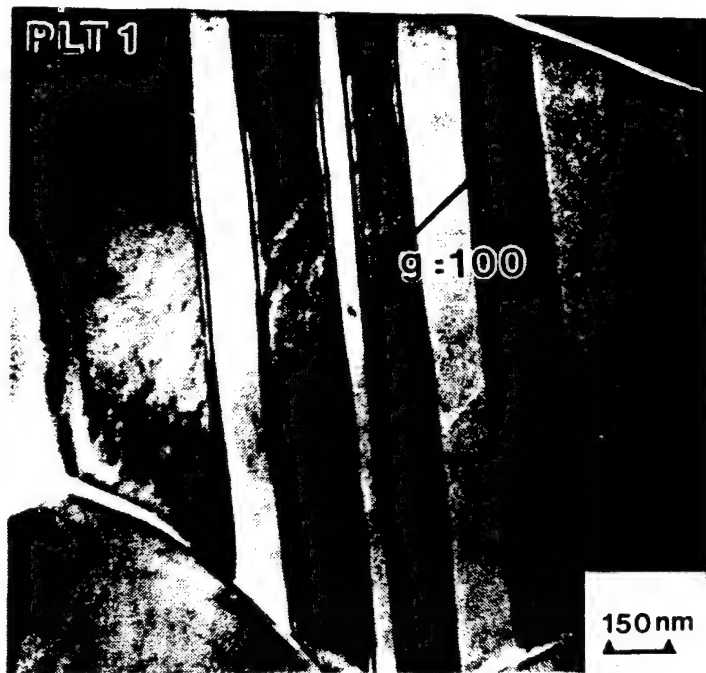


Fig. 1 / Cas

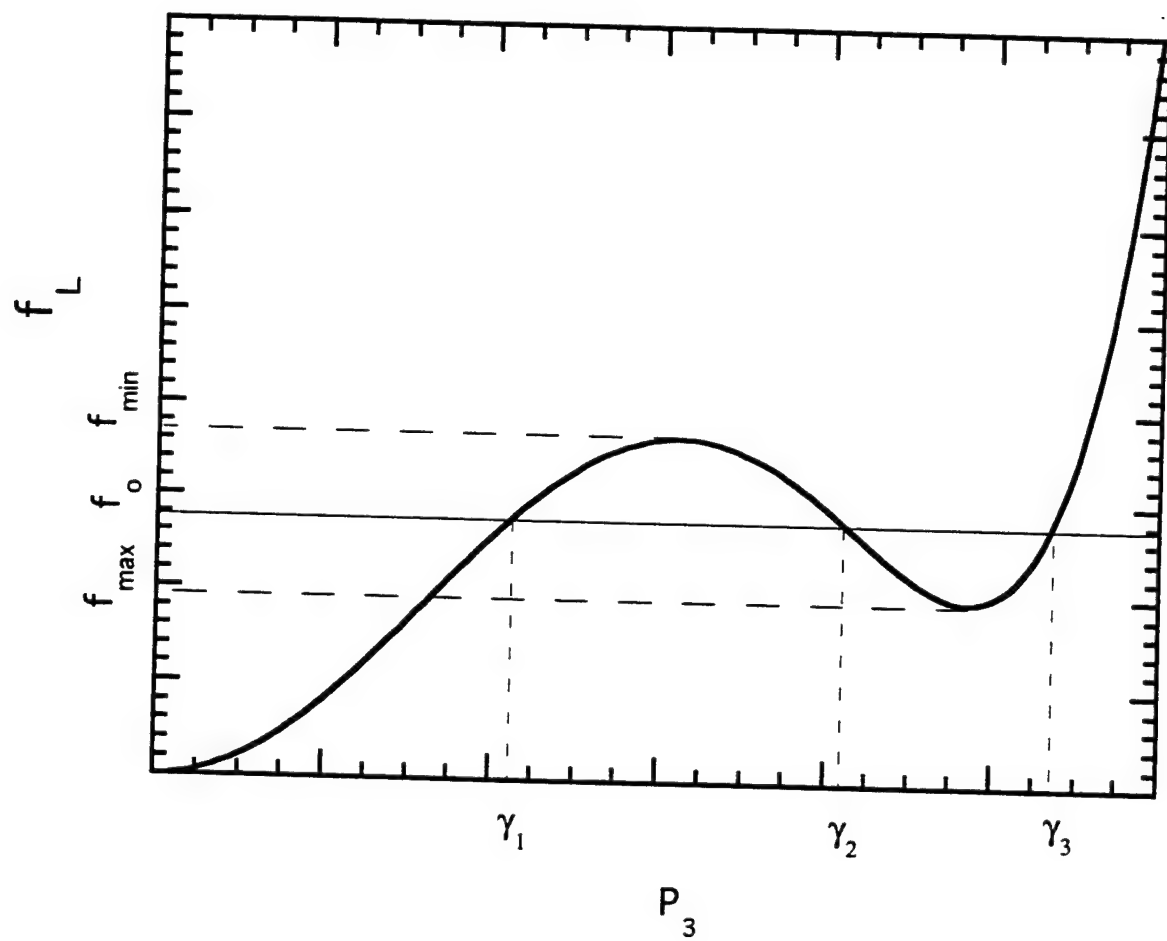


Fig. 2 / Cao

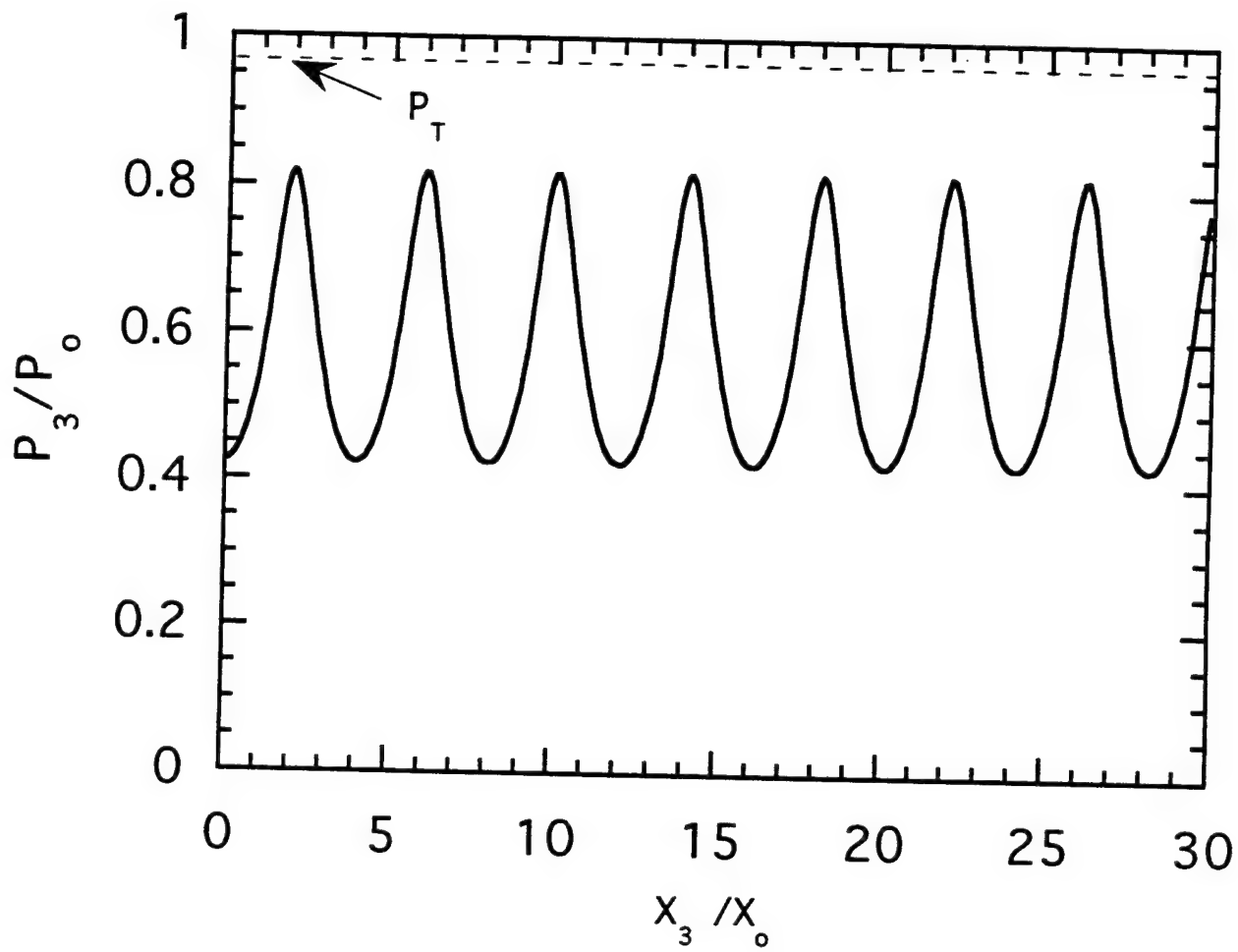


Fig. 3 / Cao

# **APPENDIX 20**



## AN IMPROVED QUANTITATIVE METHOD FOR DETERMINING DYNAMIC CURRENT RESPONSE OF PYROELECTRIC MATERIALS

J. SOPKO, A. BHALLA and L. E. CROSS

*Materials Research Laboratory, The Pennsylvania State University,  
University Park, PA 16802 USA*

*(Received August 15, 1994; in final form February 14, 1995)*

An improved quantitative pyroelectric characterization system has been developed in an effort to more thoroughly investigate the dynamic pyroelectric response of selected materials at particular temperatures of interest, such as at transition, or to study electrical aging effects. Specifically, the system is capable of measuring pyroelectric current responsivity of a wide variety of materials ranging from ferroelectric ceramics to polymers at constant temperature utilizing a modulated heating source technique.<sup>1</sup> Effectiveness of this system was determined through measurements of lithium tantalate and lithium niobate samples of various geometries. The result of the study was a comprehensive evaluation of dynamic pyroelectric current responsivity of these samples with a particularly good signal-to-noise enhancement for evaluating high noise materials such as polymer gels which are extremely difficult to evaluate using other techniques. These measurements revealed a significant dependence of the pyroelectric response on frequency of heating illumination. Bandwidth characteristics were governed primarily by the complex thermal diffusive properties and geometries of the samples.

*Keywords:* pyroelectrics, dynamic response measurements,

### BACKGROUND

The most widely accepted technique used to measure pyroelectric coefficient of materials is that described by Byer and Roundy<sup>2</sup> in which a sample is heated or cooled at a sufficiently slow linear rate to achieve a known change in bulk sample temperature with time. Knowing the sample area,  $A$ , and measuring the d-c pyroelectric current,  $i_p$ , calculation of the pyroelectric coefficient,  $p_i$ , is quite straightforward since  $dT/dt$  can be considered constant.

$$i_p = A \frac{dP}{dt} = A \frac{dP}{dT} \frac{dT}{dt} = A p_i \frac{dT}{dt} \quad (1)$$

However, in certain issues such as the evaluation of pyroelectric behavior near transition temperatures or when measuring lossy samples under high noise conditions, the d-c pyroelectric current at precise temperature points may be difficult to distinguish either due to averaging the effect over a given temperature range or due to the presence of piezoelectric or thermoelectric noise sources. Also, since pyroelectric detector materials are more often utilized in some form of chopped illumination design at constant temperature, a system utilizing those conditions would be most desirable in evaluating detector material performance. Since the latter is an a-c system with a known chopping frequency,  $f_c$ , this technique (Chynoweth's Method) leads itself directly to signal-to-noise enhancement through the use of a lock-in analyzer or a digital signal processing.

# QUANTITATIVE A-C PYROELECTRIC MEASUREMENT SYSTEM DESIGN

## Theory

The unique feature of the present system is the type of illumination of technique used. Since pyroelectric detectors are usually blackened to increase thermal absorption, they are virtually indifferent to the specific wavelength of the incident radiation provided the emissivity at that wavelength is known. The major task in quantifying a pyroelectric response system is the ability to measure exactly how the incident radiation is absorbed. This is most easily accomplished through the evaluation of the overall energy conservation equation<sup>4</sup>:

$$P_a = P_{inc} - P_l \quad (2)$$

where the accumulated power ( $P_a$ ) in the sample equals the incident power ( $P_{inc}$ ) less the power lost ( $P_l$ ).

$$P_{inc} = WA\eta f(t) \quad (3)$$

$$P_l = (8A\sigma\eta T_0^3 + G_c)\Delta T = G\Delta T \quad (4)$$

$$P_a = \rho A\delta(\partial\Delta T/\partial t) \quad (5)$$

where  $W$  = power incident ( $\text{Wm}^2$ );  $\eta$  = emissivity of sample surface;  $f(t)$  = periodic chopping function with period  $\lambda$ ;  $A$  = detector electrode area ( $\text{m}^2$ );  $T_0$  = background temperature ( $^\circ\text{K}$ );  $G$  = thermal conductance and radiation conductance to surroundings in parallel ( $\text{W}/^\circ\text{K}$ );  $\sigma$  = Stefan-Boltzmann's constant,  $5.66 \times 10^{-8} \text{ W/m}^2 - ^\circ\text{K}$ ;  $\rho$  = density of the pyroelectric material ( $\text{Kg/m}^3$ );  $c$  = specific heat capacity of the material ( $\text{J/Kg}^\circ\text{K}$ );  $\Delta T$  = temperature difference between background and sample ( $^\circ\text{K}$ );  $\delta$  = thickness of sample (m).

Using Equations (3-5), the energy conservation equation becomes:

$$dA\rho c(\partial\Delta T/\partial t) = WA\eta f(t) - G\Delta T \quad (6)$$

This system would have a thermal time constant,  $\tau_t$ , equal to:

$$\tau_t = A\delta\rho c/G \quad (7)$$

which would represent the low frequency lumped parameter thermal model shown in Figure 1(a) with a typical pyroelectric current and voltage response shown in Figure 1(b). Theoretically then, the pyroelectric current response ( $R_i$ ) should be independent of heating frequency above some frequency  $\omega_t = 1/R\theta C\theta$  and the high frequency rolloff in the voltage response should be limited only by measurement system input impedance. In order to eliminate the effects of stray capacitance and the high frequency limitation of voltage measurement, current detection was used to increase bandwidth fidelity.

In particular, this approach described by Singer<sup>4</sup> for a thermally isolated sample heated by a chopped (100% squarewave modulated) light beam applies directly to the present design as well as in the description of actual device operations. If the chopping period  $\lambda \ll \tau_t$ , then the approximation below is valid

$$I_0 \cong i_p \cong WA\eta p_i A/2\rho c\delta \quad (8)$$

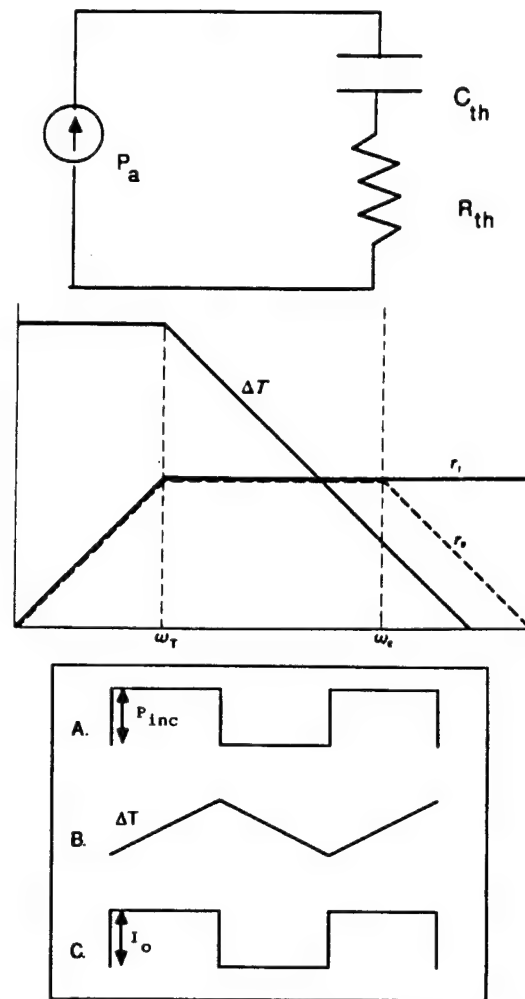


FIGURE 1 (a) Thermal model for low frequency analysis. (b) Plot of  $\Delta T$  and pyroelectric current response ( $R_i$ ), and voltage response ( $R_v$ ) versus heating frequency. (c) Relationship between incident power signal (A), sample temperature (B) and pyroelectric signal (C) for a chopping period much less than the thermal time constant.

where  $I_o$  is the peak-to-peak excursion of the pyroelectric current. Since the heating frequency is much greater than  $\omega_T$ , the heating rate is almost linear resulting in a waveform shown in Figure 1(c).

It is noted here that an accurate use of Equation (8) is only possible if the thermal properties of the sample are known. If the thermal coefficients are unknown then characteristics such as pyroelectric responsivity can still be measured quantitatively.

Sample illumination in the present system is accomplished by electronically modulating a Seiko SMD-10E LED through a 50/125  $\mu\text{m}$  multimode fiber at 842 nm wavelength. Light emitted from the fiber end directly illuminates the blackened surface of the sample material. Considering a fiber with a numerical aperture of

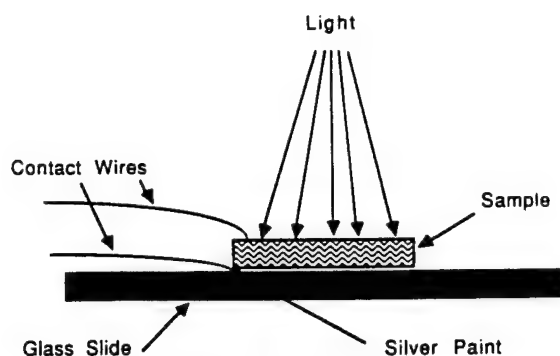


FIGURE 2 Sample mounting.

$\sim 0.25$ , an 8 mm separation produces a 4 mm diameter spot. Provided the sample is a disc approximately 4.5–5 mm in diameter virtually all the power emanating from the fiber end is incident on the sample (Figure 2), and with a high emissivity ( $\eta \sim 1$ ) coating virtually all of that incident power should be absorbed into the sample. Therefore, by measuring the output power of the fiber with an optical power meter, pyroelectric current response could be directly calculated from

$$R_i = \frac{I_0}{P_a} \quad (9)$$

Other features of the LED/fiber system are its high stability of the chopping waveform essential to an accurate averaging technique, the ability to modulate any waveform, electrical isolation, wide-band frequency response (D.C. to 35 MHz), elimination of acoustic noise generated by mechanical vane choppers and a great reduction in cost.

To ensure low thermal conduction to the surroundings, the sample was weakly thermally mounted on a glass cover slide with only enough silver paint to attach electrode wires. The background temperature was controlled by a MMR Technologies System I Microrefrigerator and A MMR Technologies K-20 Programmable Temperature Controller which was linked via the IEEE-488 Instrumentation Bus with a Hewlett-Packard Series 9000 computer. The sample chamber was also evacuated to  $\sim 10$  mT to reduce the effects of convective thermal loss.

#### *Pyroelectric Current Measurement*

The pyroelectric current is measured directly using a lock-in analyzer synchronized to the chopping frequency of the source. An EG&G Model 5208 analyzer was selected with an EG&G Model 181 current preamplifier. A heterodyne mixer in the 5208 which features a  $Q$  of about 10,000 aided significantly in noise reduction by reducing the observed signal bandwidth. The high sensitivity and low noise of the 5208/181 combined with the high current gain ( $10^{-9}$  A/V) of the Model 181 gave an overall resolution of 1 fA ( $10^{-15}$  A) with a usable 1  $\mu$ V resolution of the 5208. The highest input impedance of the 181 is  $\sim 10$  K $\Omega$  at a gain setting of  $10^{-9}$  A/V. This had no noticeable effect on the sample circuit for the samples used;

however, for high loss samples this input impedance would be a consideration restricting current gain to lower settings. The bandwidth of the 181 on the highest gain setting ( $10^{-9}$  A/V) is limited to  $\sim 2$  KHz; therefore, for true fidelity in measuring frequency response, lower gain settings (such as  $10^{-6}$  A/V) provided a usable bandwidth up to  $\sim 100$  KHz. In connecting the sample to the Model 181, low noise coaxial cable was used to reduce the effects of triboelectric noise at the input.

One significant factor that needed consideration is that although the SMD-10E was square wave modulated and thus the pyroelectric signal at mid-band would also be a square wave, the Model 5208 responds only to the fundamental sinusoidal component of the modulation signal. Therefore, some adjustment must be made to the 5208 readings to reproduce the peak current produced by the sample. A square wave is represented by the Fourier series:

$$I(\omega t) = \frac{4}{\pi} I_0 \left[ \sin(\omega t) + \frac{1}{3} \sin(3\omega t) + \frac{1}{5} \sin(5\omega t) + \dots \right] \quad (10)$$

Since only the fundamental is detected, the RMS value indicated on the 5208 is related to the peak-to-peak square wave amplitude,  $I_0$ , by:

$$I_0 = V_{5208} \frac{\pi}{4} (2\sqrt{2}) \cdot A_i = V_{5208} \frac{\sqrt{2}\pi}{2} \cdot A_i \quad (11)$$

where  $V_{5208}$  is the voltage measured by the 5208 and  $A_i$  is the current gain of the Model 181 in (A/V). The agreement of this method for reproducing  $I_0$  is very good ( $<1\%$ ) when compared with a calibrated oscilloscope display. The EG&G Model 5208 has a frequency response of .5 Hz–200 KHz and is capable of an averaging time constant of up to 30 seconds.

For low frequency analysis ( $<.5$  Hz) a Hewlett-Packard 54201A digitizing oscilloscope is used. The most significant feature of the HP 54201A is an ensemble averaging capability which allows for substantial noise reduction and signal en-

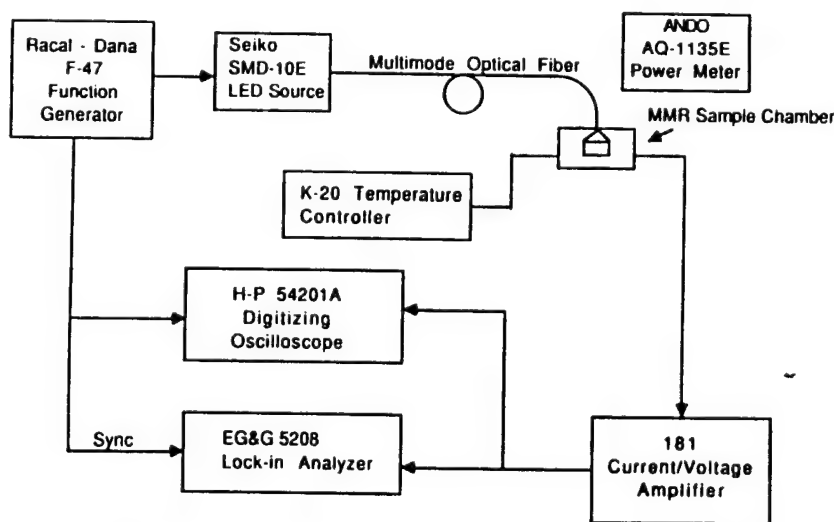


FIGURE 3 Overall block diagram of MRL-Chynoweth System.

hancement. Since again the pyroelectric signal is periodic, the oscilloscope display and sampling can be synchronized in time with the modulating signal. Since the synchronized signal will occur in the same relationship in time on the display each trigger cycle, the average value of each sample bin over time will closely approximate the pyroelectric signal at that point. Provided that the noise is uncorrelated in time with the signal, a substantial improvement in S/NR results. Another distinct advantage of this type of processing is that the high frequency components of the signal are retained. This particular method calculates a separate moving average for each of the 1001 data bins in the ensemble and is capable of averaging up to 256 ensembles, updating the display with the 256 ensembles taken. The overall block diagram of the system is shown in Figure 3.

### *Measurement Procedure*

The samples were electroded with sputtered gold layer on both sides and mounted on a glass cover slide. Electrical contacts were made by placing whisker-type silver wire on each electrode and held in place using sparse amounts of silver paint. The cover slide-sample assembly was thermally connected to the MMR Microrefrigerator stage with heat sink compound.

The illumination fiber was inserted into the temperature chamber through a Seko SAA-2 bulkhead adapter and the sample illuminate through a glass cover which was used to ensure vacuum integrity. The optical power incident on the sample was measured at the fiber end subtracting for the attenuation of the glass slide cover, which was measured to be  $-0.27$  db using an insertion loss technique. The samples were then coated on the illuminated side with black India ink and the emissivity taken to be  $\sim 1$ .

The thermal stage was then adjusted and set for the desired background temperature,  $T_0$ , after the chamber had reached sufficient vacuum ( $<10$  mT). Allowing sufficient time for the temperature of the stage to stabilize, a frequency response profile was measured to find the peak frequency response. This was accomplished by biasing the SMD-10E sufficiently to enable faithful reproduction of sinusoidal modulation frequency ( $<100\%$  amplitude modulation). The frequency was swept to determine the maximum response frequency and bandwidth of the sample. Amplitude and phase were measured at discrete frequency points with the lock-in analyzer. The function generator was then set to the maximum response frequency, which theoretically should indicate mid-band response, and the d-c removed from the SMD-10E. The SMD-10E was then driven by a square wave with a 50% duty cycle which caused 100% amplitude modulation of the SMD-10E output. Typical risetime for the SMD-10E was rated at 10 ns (35 MHz) which establishes the upper frequency limit of the driving light signal. Output power of the SMD-10E was measured during the on cycle to determine peak incident power. Temperature of the stage/sample was then stepped through the range 250–350°K and the pyroelectric current,  $I_0$ , measured at chosen temperature points. The pyroelectric current responsivity and pyroelectric coefficient were calculated using Equations (8) and (9). Since the total power emitted by the fiber is incident on the sample, the power reading taken with the ANDO AQ-1135E could be used for WA.

In order to demonstrate the capabilities of the system,  $\text{LiTaO}_3$  and  $\text{LiNbO}_3$

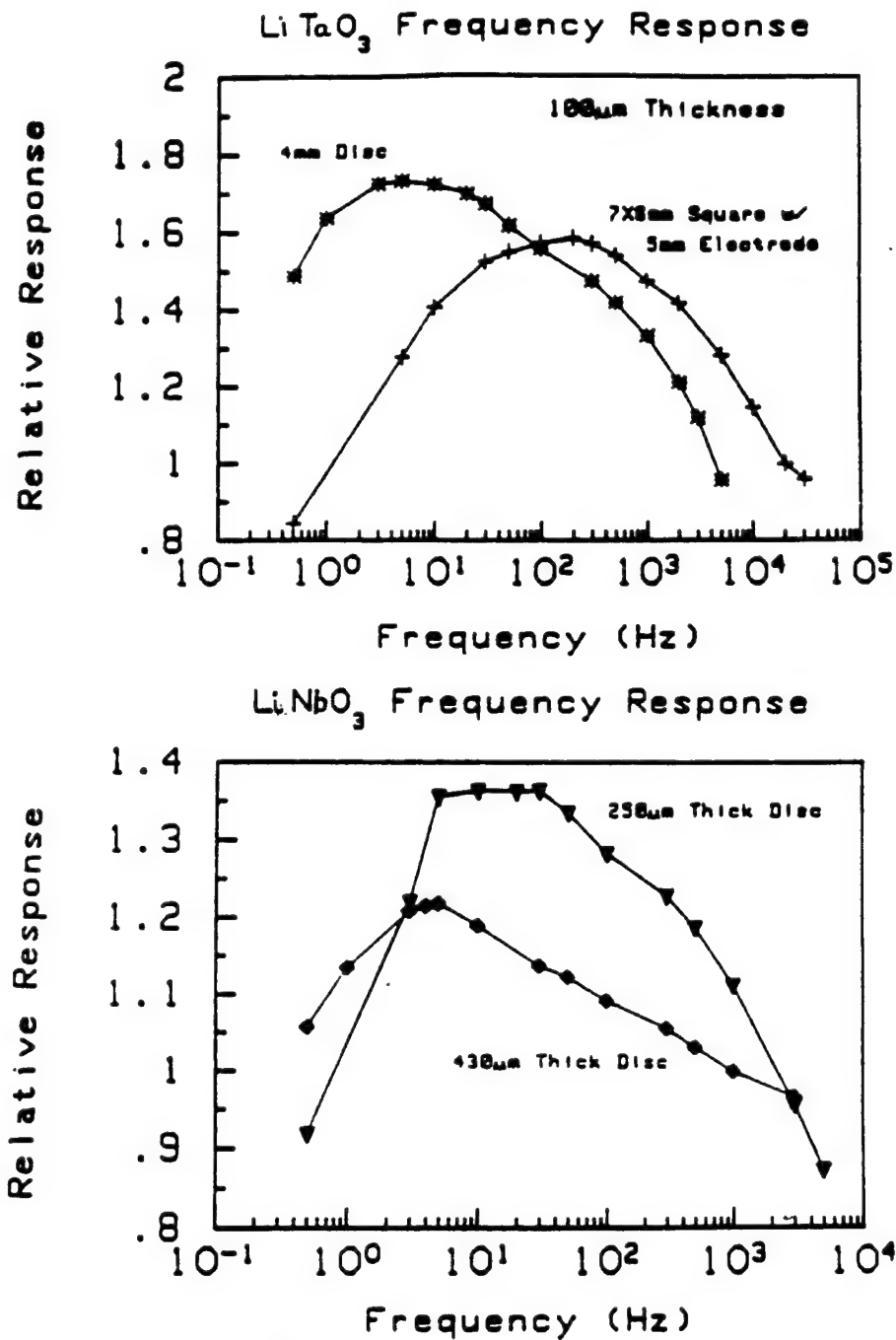


FIGURE 4 (a) Relative frequency response of lithium tantalate with respect to data taken via the Byer and Roundy method. (b) Relative frequency response of lithium niobate with respect to data taken via the Byer and Roundy method.

samples were chosen for the measurements of pyroelectric coefficients, and the results were compared with those measured by the Byer-Roundy technique. Details of the data and the samples are given in the appendix section of this paper. It's clear that the pyroelectric coefficients measured by the present system yielded the higher values, but the slope of the  $p$  vs.  $T$  in the case of  $\text{LiTaO}_3$ , seems to be very close, as shown in Figure 4.

After applying the proper thermal parameters and correction factors, the values very close to those measured by the Byer-Roundy technique were obtained.

The differences in the pyroelectric response data taken with the present dynamic system and that of Byer and Roundy, we feel, are attributable to the method and frequency of the heating radiation. In the Byer-Roundy method, the sample is uniformly heated at a pre-determined rate to generate the required change in temperature. Since both surfaces of the sample are heated equally, the current measured will be a function of the pyroelectric coefficient and the rate of change of the bulk temperature. In the present system, the bulk temperature of the sample is held constant, and induced temperature change is due to the optical illumination, which is incident only to one side. This may induce a temperature differential between the illuminated face and the opposite side of the sample which is not present in the Byer-Roundy system. Further, if the thermal wave propagation within the sample is considered, then perhaps as the illumination wavelength approaches twice the sample thickness the temperature phase differences at both face electrodes may be 180 degrees out of phase. This may explain a pyroelectric currents which are off by a factor of two. When attenuation of the thermal wave within the sample is considered, the result would then be a factor between one and two.

All the other reasons we discussed earlier would account only for value of the pyroelectric current to be less than that of Byer-Roundy. Temperature phase differences at the face electrodes seem to be a logical explanation, since lack of proper mounting of the sample would only lessen the measured current. Perhaps the answer is a combination of the two.

Further design improvements would include using a programmable calibrated light source capable of generating approximately 1 mW of optical output power source. A more careful mounting of the sample and cleaner electroding practices should also help.

#### *Practical Applications and Future Work*

Perhaps the most straightforward application of this system is in detector design optimization. The system provides for quantitative spectral analysis of pyroelectric detectors in an environment similar to actual implementation. Therefore, for a given detector, an optimum chopping frequency could be chosen to yield maximum detector response. Another application could be in the study of the thermal characteristics of the sample materials perhaps in relating the depth of thermal penetration to the high frequency limit. It appears that due to the rapid thermal diffusion at the surface at high frequencies, as frequency is increased, more of the incident energy is used to heat only the regions that are responsible for generating the pyroelectric surface charge. This would account for some frequency dependence due to high efficiency heating near the surface and above which the decrease in



the depth of thermal penetration no longer provides sufficient heating to the deeper material. This could explain the effective "peak" of the pyroelectric current that is well above what was predicted and also the high frequency roll-off due to the lack of temperature change felt in the bulk at higher frequencies.

Since it uses a highly localized fiber for illumination, locating the fiber closer to the material allows for the illumination area to be reduced down to the core size of the fiber. This could be as small as 9  $\mu\text{m}$  in diameter if single mode fiber is used. Thus, a precision stepper drive positioning system could move the fiber in an  $x$ - $y$  plane, allowing for the examination of the microstructure of the material surface. This would find a direct application in array element analysis and production control and in the analysis of individual grains of a ceramic or composite detector. Studies involving the use of this system for determining electric field aging effects and the pyroelectric responsivity of polymer gels are also conducted successfully. Further refinements such as a calibrated LED source (e.g. HP 8154B) and spectral analysis equipment would greatly enhance the quality of the data.

## SUMMARY

The present system has several advantageous features:

- Use of fiber optic/electronic modulation allows for extremely accurate averaging techniques, greatly increasing measurement sensitivity. Rotary vane choppers are unstable in freq. Also much greater frequency range/modulation choices.
- Use of optoelectronic modulation eliminates "false pyro" signals due to coupling of acoustic "fan noise" generated by rotary vane choppers.
- Grounding of stage plate to dewar eliminates noise contribution from heater in MMR microrefrigerator vastly increasing the signal-to-noise ratio of the system.
- Optoelectronic modulation also allows thermal analysis due to ability to use CW sinusoidal heating, swept over frequency to determine optimum response of system.
- Electric aging experiments can be conducted using fixed temperature by plotting pyro response over time under bias conditions.
- Averaging oscilloscope allows viewing of sample behavior/aids in sample signal analysis.

## APPENDIX A

### SAMPLE PYROELECTRIC RESPONSE DATA SUMMARY AND ANALYSES

#### 1. *Dynamic Pyroelectric Signal Analysis of $\text{LiTaO}_3$*

Two samples of  $\text{LiTaO}_3$  were measured to determine the pyroelectric frequency dependences due to varying geometry. Sample 1 was a 7  $\times$  6 mm square with a

5-mm diameter disc electroded on each side. The illuminated face was blackened with India ink to increase thermal absorption. Data was taken using the method described with frequency response as follows:

TABLE A1  
Sample 1 (LiTaO<sub>3</sub>) frequency response to CW sinusoidal illumination.  $P_{inc} = 65.4 \mu\text{W}$ , gain =  $10^{-6} \text{ A/V}$ , thickness =  $100 \mu\text{m}$ ,  $T = 292^\circ\text{K}$

Frequency (Hz)	$V_{5208} (\mu\text{V})$	Phase (degrees)
0.5	6.48	54.0
5	9.81	15.0
10	10.81	10.0
30	11.70	4.1
50	11.90	3.0
100	12.08	1.1
200	12.17	-1.5
300	12.06	-2.8
500	11.83	-5.0
1000	11.32	-7.7
2000	10.88	-10.9
5000	9.84	-20.0
10,000	8.80	-31.3
20,000	7.68	-46.7
30,000	7.37	-60.2

TABLE A2  
Sample 1 (LiTaO<sub>3</sub>) effective pyroelectric coefficient temperature dependence.  $P_{inc} = 65.4 \mu\text{W}$ ,  $f_c = 200 \text{ Hz}$

Temperature ( $^\circ\text{K}$ )	$I_0 (\text{pA})$	$p (\mu\text{C/m}^2 \cdot ^\circ\text{K})$	RI (nA/W)
263	28.1	275.3	429.7
273	28.30	277.2	432.7
283	28.48	279.0	435.5
293	28.68	281.0	438.5
303	28.90	283.1	441.9
313	29.14	285.5	445.6
323	29.36	287.6	448.9
333	29.54	289.4	451.7
343	29.65	290.5	453.4
353	29.96	293.5	458.1
363	30.12	295.1	460.6

Sample 2 of LiTaO<sub>3</sub> was of equal thickness ( $100 \mu\text{m}$ ) but was cut down to a 4-mm disc and fully electroded. The expected result was an increase in response due to reduced thermal loading of the sample as well as a decrease in the peak response owing to a longer thermal time constant due to less thermal dissipation to the nonelectroded area of Sample 1.

TABLE A3

Sample 2 ( $\text{LiTaO}_3$ ) frequency response to CW sinusoidal illumination. 4-mm disc. Gain =  $10^{-7}$  A/V,  $T = 292^\circ\text{K}$ , phase was not measured

Frequency (Hz)	$V_{5208}$ ( $\mu\text{V}$ )
.5	97.5
1	107.3
3	112.9
5	113.3
10	112.6
20	111.0
30	109.3
50	105.8
100	102.0
300	96.6
500	92.9
1000	87.2
2000	79.3
3000	73.3
5000	62.7

TABLE A4

Sample 2 ( $\text{LiTaO}_3$ ) effective pyroelectric coefficient temperature dependence.  $f_c = 35$  Hz,  $P_{\text{inc}} = 66.6 \mu\text{W}$  (on-cycle peak power)

Temperature ( $^\circ\text{K}$ )	$I_0$ (pA)	$p$ ( $\mu\text{C}/\text{m}^2 \cdot ^\circ\text{K}$ )	$R_1$ (nA/W)
253	29.30	290.6	439.9
263	29.59	293.4	444.3
273	29.96	297.2	449.8
283	30.28	300.3	454.7
293	30.72	304.7	461.3
303	31.19	309.3	468.3
313	31.59	313.3	474.3
323	32.12	318.5	482.3
333	32.54	322.7	488.6
343	32.99	327.1	495.3
353	33.50	332.2	503.0
363	33.98	337.1	510.2
373	34.63	343.4	520.0

Repeatability of measurements for effective pyroelectric coefficient at room temperature was extremely stable ( $<2\%$  spread). Factors affecting the measurement stability/repeatability were often directly related to power fluctuations in the SMD-10E source or change in stress on the optical fiber. Figure A-1 shows a typical pyrocurrent signal for Sample 2.

## 2. Dynamic Pyroelectric Signal Analysis of $\text{LiNbO}_3$

Two samples of  $\text{LiNbO}_3$  of different thicknesses but similar area were measured (Sample 3 =  $430 \mu\text{m}$ , Sample 4 =  $250 \mu\text{m}$ ). Both samples had a fully electroded area of  $\sim 4$  mm diameter and blackened with India ink as were the  $\text{LiTaO}_3$  samples.

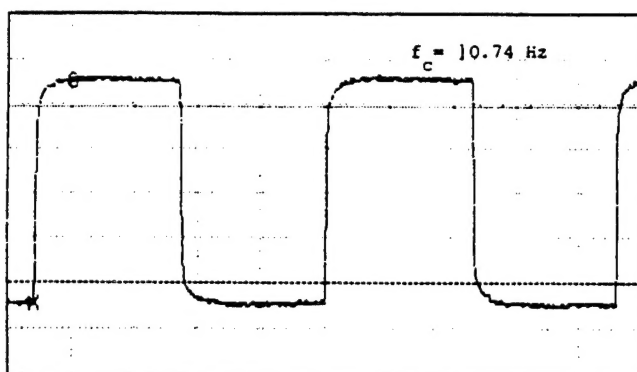


FIGURE A1 Pyroelectric current signal of Sample 2.  $T = 292^\circ\text{K}$ ,  $P_{mc} = 67 \mu\text{W}$ ,  $I = 30.6 \text{ pA}$ .

TABLE A5

Sample 3 ( $\text{LiNbO}_3$ ) frequency response to CW sinusoidal illumination. Thicknesses =  $430 \mu\text{m}$ ,  $T = 292^\circ\text{K}$ , Gain =  $10^{-8} \text{ A/V}$

Frequency (Hz)	$V_{5208}$	Phase (degrees)
.5	94.2	26.6
1	101.1	25.6
3	107.7	8.2
4	108.3	4.8
5	108.6	2.5
10	106.0	-1.9
30	101.3	-4.8
50	100.0	-5.0
100	97.2	-5.0
300	94.0	-6.3
500	91.8	-7.5
1000	89.0	-10.4

TABLE A6

Sample 3 ( $\text{LiNbO}_3$ ) effective pyroelectric coefficient temperature dependence.  $P_{mc} = 67 \mu\text{W}$ ,  $f_c = 5 \text{ Hz}$

Temperature ( $^\circ\text{K}$ )	$I_0$ (pA)	$p$ ( $\mu\text{C}/\text{m}^2\cdot^\circ\text{K}$ )	$R_f$ (nA/W)
263	2.832	72.34	42.27
273	2.861	73.08	42.70
283	2.888	73.76	43.10
292	2.910	74.33	43.43
303	2.936	75.01	43.82
313	2.959	75.57	44.16
323	2.996	76.54	44.72
333	3.023	77.22	45.12
343	3.048	77.84	45.49
353	3.092	78.98	46.15
363	3.116	79.60	46.51
373	3.139	80.17	46.85

TABLE A7

Sample 4 ( $\text{LiNbO}_3$ ) frequency response to CW sinusoidal illumination. Thickness = 250  $\mu\text{m}$ ,  $T = 292^\circ\text{K}$ , Gain =  $10^{-7}$  A/V

Temperature	$V_{5208}$ ( $\mu\text{V}$ )	Phase (degrees)
.5	17.69	49.3
3	23.50	15.7
5	26.10	7.4
10	26.25	3.4
20	26.22	-0.5
30	26.25	-2.5
50	25.70	-4.3
100	24.70	-5.4
300	23.65	-8.1
500	22.85	-10.1
1000	21.40	-15.8
3000	18.40	-27.5
5000	16.80	-42.0

TABLE A8

Sample 4 ( $\text{LiNbO}_3$ ) effective pyroelectric coefficient temperature dependence.  $P_{\text{inc}} = 64.8 \mu\text{W}$ ,  $f_c = 10$  Hz

Temperature ( $^\circ\text{K}$ )	$I_0$ (pA)	$P$ ( $\mu\text{C}/^\circ\text{K}$ )	$R_I$ (nA/W)
263	5.664	87.46	87.41
273	5.724	88.39	88.33
283	5.760	89.07	88.89
293	5.809	89.69	89.65
303	5.842	90.21	90.15
313	5.902	91.13	91.08
323	5.953	91.92	91.87
333	6.013	92.85	92.79
343	6.068	93.70	93.64
353	6.153	95.01	94.95
363	6.197	95.69	95.63
373	6.235	96.28	96.22

TABLE A9

Comparison of MRL-PSU data with data acquired using the method of Byer and Roundy,  $T = 292^\circ\text{K}$ ,  $P_1$  (Byer and Roundy),  $P_2$  MRL-PSU)

Sample	Material	Thickness ( $\mu\text{m}$ )	$P_1$ ( $\mu\text{C}/\text{m}^2 \cdot ^\circ\text{K}$ )	$P_2$ ( $\mu\text{C}/\text{m}^2 \cdot ^\circ\text{K}$ )
1	$\text{LiTaO}_3$	100	176	281.0
2	$\text{LiTaO}_3$	100	176	304.7
3	$\text{LiNbO}_3$	430	61	74.33
4	$\text{LiNbO}_3$	250	61	89.69
5	PZZN-90	313	215	296.6
6	PZZN-92	344	214	348.6

## ACKNOWLEDGEMENTS

Authors are thankful to Sei-Joo Jang, Qiming Zhang, and Tadashi Takenaka for several useful discussions during the course of this work. A final expression of thanks is given to the United States Navy with whose permission J. Sopko, as a Naval Officer, was able to participate in this research.

## BIBLIOGRAPHY

1. J. A. Sopko, "A Quantitative Method for Determining Dynamic Response Characteristics of Pyroelectric Materials," Masters Thesis, The Pennsylvania State University, University Park, PA 1987."
2. R. L. Byer and C. B. Roundy, "Pyroelectric Coefficient Direct Measurement Technique and Application to a Nsec Response Time Detector," *Ferroelectrics*, **3**, 333-338 (1972).
3. A. G. Chynoweth, "Dynamic Method for Measuring the Pyroelectric Effect with Special Reference to Barium Titanate," *J. Appl. Phys.*, **27**, 78-84 (1956).
4. B. Singer, "Theory and Performance Characteristics of Pyroelectric Imaging Tubes," in "Advances in Image Pickup and Display," ed. B. Kazan, Academic Press, pp. 1-8, 1977.